INTRACORTICAL NEURAL PROBES

WITH POST-IMPLANT SELF-DEPLOYED ELECTRODES

FOR IMPROVED CHRONIC STABILITY

by

Daniel G. D. Egert

**A dissertation submitted in partial fulfillment of the
requirements for the degree of
Doctor of Philosophy
(Electrical Engineering)
in The University of Michigan
2015**

Doctoral Committee:

      **Professor Khalil Najafi, Chair
      Assistant Professor Timothy Bruns
      Assistant Professor Becky L. Peterson
      Professor Kensall D. Wise**

DEDICATION

To my aunt Marie-Luise, a role model in taking on big challenges.

TABLE OF CONTENTS

LIST OF TABLES

LIST OF FIGURES

LIST OF APPENDICES

ABSTRACT

INTRACORTICAL NEURAL PROBES

WITH POST-IMPLANT SELF-DEPLOYED ELECTRODES

FOR IMPROVED CHRONIC STABILITY

by

Daniel Egert

Chair: Khalil Najafi

This thesis presents a new class of implantable intracortical neural probe with small recording electrodes that deploy away from a larger main shank after insertion. This concept is hypothesized to enhance the performance of the electrodes in chronic applications.

Today, electrodes that can be implanted into the brain for months or years, are an irreplaceable tool for brain machine interfaces and neuroscience studies. However, these chronically implanted neural probes suffer from continuous loss of signal quality, limiting their utility. Histological studies found a sheath of scar tissue with decreased neural density forming around probe shanks as part of an ongoing chronic inflammation. This was hypothesized to contribute to the deterioration of recorded signals. The neural probes developed in this thesis are designed to deploy

electrodes outside this sheath such that they interface with healthier neurons. To achieve this, an actuation mechanism based on starch-hydrogel coated microsprings was integrated into the shank of neural probes. Recording electrodes were positioned at the tip of micrometer fine and flexible needles that were attached to the springs. Before insertion, the hydrogel dehydrates, retracting the springs. After insertion, the gel rehydrates, releasing the springs, which then deploy the electrodes. The actuation mechanism functions in a one-time release fashion, triggered by contact with biological fluids at body temperature. The deployment of the electrodes occurred over the course of two hours and can be divided into three stages: For the first 20 s, the electrodes did not deploy. Within the first three minutes they deployed by roughly 100 µm (0.5 µm/s). Tor the following two hours they deployed an additional 20 µm (0.17 µm/min). The employed design supported six deploying electrodes, each at the end of a 5 µm wide and thick, and 100 µm long needle. These were attached to a shank with 290 µm width, 12 µm thickness and 3 mm length. The shanks could be inserted into the cortex of rats through an opening in the pia without breaking. The acquired waveforms indicate that some of the deployed electrodes were able to record neural action potentials.

CHAPTER 1

INTRODUCTION

1.1   Interfacing with the central nervous system

The mammalian central nervous system has an unmatched ability to interact with the environment and builds upon unmatched complexity. It became the distinguishing factor for human success; it can be inspiration for biomimetic systems or if malfunctioning, source of pain, impair senses, motor control or cognitive function. The central nervous system consists of the brain and the spinal cord. Its main active building blocks are neurons. The human brain contains some twenty billion neurons with some hundreds of trillion connections between them. Most of the cell bodies are positioned in the outer 2 mm of the cerebrum called the cerebral cortex. Their axons or dendrites, forming outgoing and incoming connections, run underneath. To transmit and process information, neurons use electrical potentials created by ion flows and modulated by other chemicals.

There is great scientific and clinical interest in exploring, restoring and improving the functions of the human brain. Hence many tools have been developed to probe and modulate the activity of neurons. Amongst all of them, electrodes are to-date irreplaceable. Unlike most other methods, electrodes allow to resolve activity of single neurons with high speed and high spatial resolution in an almost arbitrary position in the brain.

Brain interfaces have been created using stimulating electrodes implanted into nuclei inside the cerebrum (deep brain stimulation), microelectrodes implanted into the cortex of the brain [1] (penetrating intracortical neural probes, as used in this thesis research), electrodes placed directly on the surface of the brain [2] (electrocorticography) or electrodes placed on the scalp (electroencephalography). A promising alternative to electrodes is enabled by optogenetics. In optogenetics, neurons are genetically rendered to become responsive to light or to express indicators that allow to optically detecting their activity [3]. However, optogenetic methods face some hurdles: genetically altering neurons (delivering viral vectors) in human patients comes with ethical issues [4]. Also, light does not penetrate deeply into nervous tissue without being perturbed. Hence it is not trivial to use light to interface with deeper lying structures on a cellular resolution. Furthermore, portable microscopes and lasers are not common practice [5]. Another way of interfacing with neurons makes use of the variety of chemicals neurons respond to and release. Small fluid channels and electrochemical sensors allow administering or extracting and analyzing fluids surrounding neurons [6].

An arising clinical application utilizes intracortical neural probes to form brain-computer interfaces [7]. For example, patients with tetraplegia can gain thought-control of a computer cursor [8] or a motor prosthesis [9]. These allow patients suffering spinal cord injuries to control motorized prostheses or their own muscles with signals recorded from their brain, bypassing the site of injury. This has been realized in humans and monkeys [10]. Another clinical application of neural interfaces that became common practice over the last few years is using the deep brain stimulation electrodes [11]. Deep brain stimulation can suppress tremors, obsessive compulsive disorders or chronic pain. It is based on the concept of modulating the activity of neural nuclei

using stimulating electrodes implanted into the brain. More specific, nuclei emitting faulty signals are reversibly silenced by rhythmic stimulation.

Many applications require interfacing with single neurons and reaching neurons that are below the surface of the brain. Intracortical neural probes allow exactly that. They typically consist of millimeter-long, several tens to hundred micrometer wide, needle-like shanks that are implanted into the cortex [12] (Figure 1). The shanks support interfaces to neurons such as recording or stimulation electrodes, optical fibers or fluidic channels for drug delivery. Bringing these interfaces in close proximity of the neurons allows selectively recording from or stimulating neurons at a cellular resolution.

a)

Neural probe array

b)

Interconnects

Electrodes

Shank

1 mm
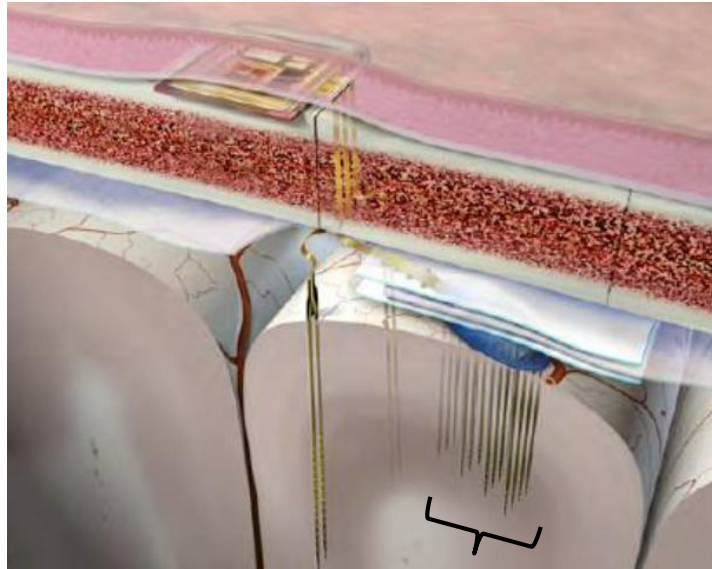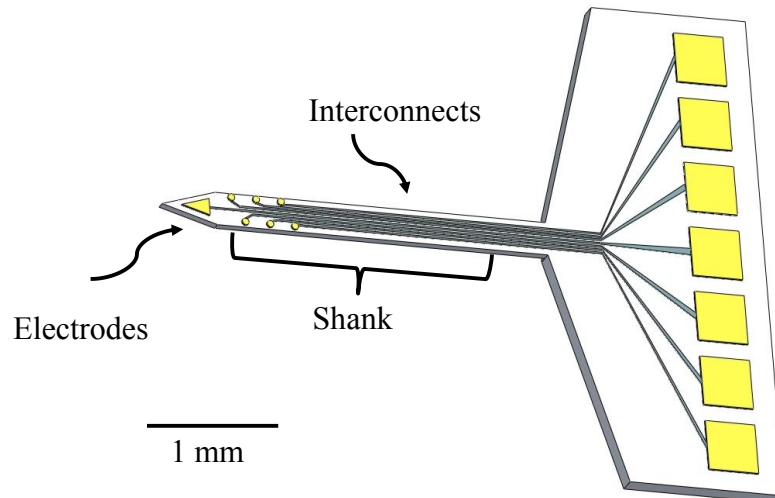
Figure 1: a) Drawing of neural probes implanted as array into the cortex **[13]** *and b), drawing of a single neural probe shank with labels used in this thesis.*

Two representative examples of neural probes often seen in studies are the Michigan Probes and Blackrock Utah arrays. The Michigan probes are fabricated using a well characterized thin-film silicon process. They are shaped to 15 μm micrometer thin shanks with multiple electrodes along the length. This electrode arrangement allows recording along columns and layers of the cerebrum.

4

These probes are often used in acute and several weeks lasting neuroscience studies. The probes are commercially available and are distributed by NeuroNexus (http://neuronexus.con) (Figure 2a).

The Blackrock Utah arrays are famous for human pilot studies [9], (Figure 2b). These are multi-year lasting experiments, allowing impaired patients control robot arms with electrode arrays. The neural probe array consists of insulated needles with exposed tips serving as electrodes. Multiple of these electrodes are arranged on a surface and allow recording from layers (instead of columns) of the cerebrum.

Deep brain stimulating (DBS) electrodes are often implanted into deep cerebral structures, far underneath the cortex. Stimulating electrodes require a larger surface area than recording electrodes. The dimensions of electrodes for deep brain stimulation are about one order of magnitude larger than typical cortical recording neural probes. Their diameter can be more than one millimeter and their length can be more than 10 cm. Deep brain stimulation electrodes are distributed by Medtronic (http://medtronic.com).
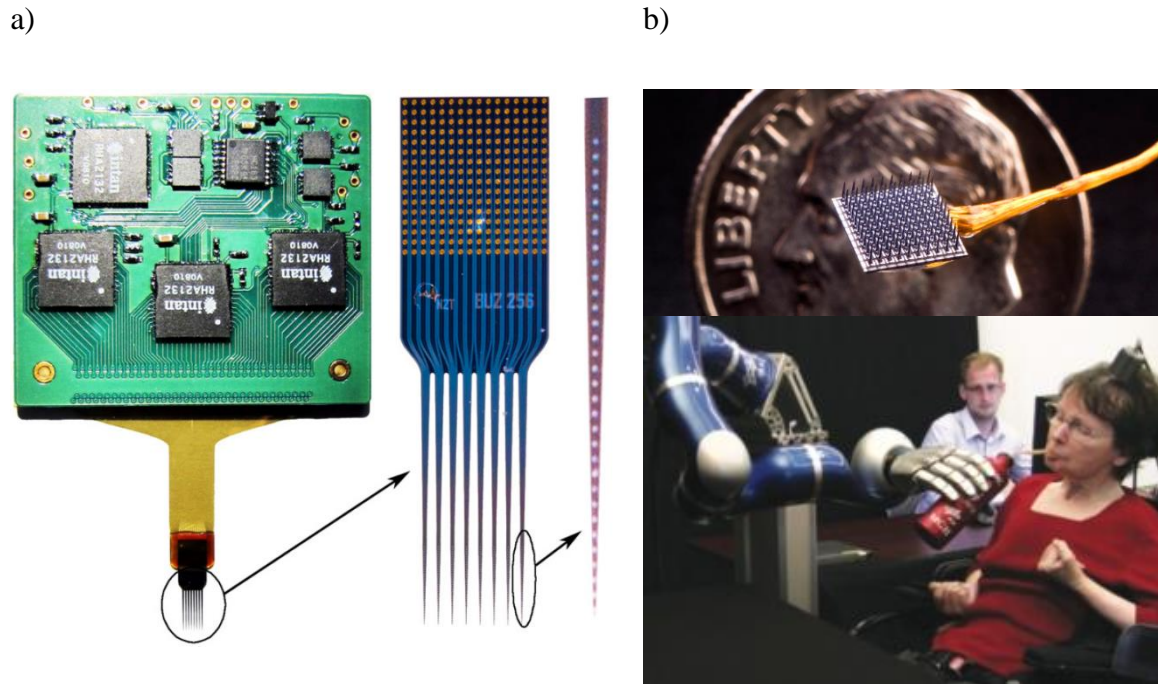
Figure 2: a) Michigan neural probes shown in a configuration for parallel recording of 512 channels in behaving rodents **[14]**. *b) A 4mmx4mm, 96-channel Blackrock Utah array (top)* **[15]** *and its application in clinical studies (bottom)* **[9]**.

1.2   Decline of signal-to-noise ratio of recorded neural activity

Several efforts have been made to investigate the chronic stability of neural probe recordings. Their common conclusion is that the signal-to-noise ratio of chronically implanted neural probes decreases continuously over time. To give three examples, the chronic performance of neural probes was investigated by implantation into rhesus macaque monkeys, into rats, and they were used in a 2.7 years lasting human trial. Blackrock Utah arrays were implanted into the motor cortex of three rhesus macaque monkeys for up to 30-month [10]. The recorded action potential amplitudes decreased by 2.4 % per month on average. Five intracortical electrode designs implanted into rat barrel cortices were compared in terms of their chronic recording function [16]. Employed designs were untethered (firmly connected to the skull) and 15 μm thick Michigan

6

probes (Neuro-Nexus, Ann Arbor, Michigan), Microwire Arrays with 50 µm diameter (Tucker-Davis Technologies, Alachua, FL), tethered floating Microwire Arrays with 75 µm diameter (MicroProbes for Life Science, Gaithesburg, MD) and Utah Arrays (Blackrock Microsystems, Salt Lake City, UT). In all designs the electrode performance, measured as signal-to-noise ratio (SNR) was highest within the first days if indwelling and then dropped. In all designs except the Microwire Arrays with 50 µm diameter, the SNR dropped to or below a baseline of usefulness, defined as 1.25 times the standard deviation of the noise. The SNR of the Microwire Arrays, after dropping to the noise floor in the first week, remained at a level of 2 for two months but then continuously dropped until the termination of the experiment. The authors of [8] implanted the Utah Array into the motor cortex of a human patient with tetraplegia. Although cursor control was still possible after 1000 days of indwelling, the number of electrodes recording action potentials and the amplitude of the action potentials was significantly smaller (169 µV +-157µV std. dev. vs. 63.1 µV +- 34 µV std.dev.).

The precise control of motor prosthesis with multiple degrees of freedom such as joints resembling an arm and a hand is offering plenty of use for enhanced performance of neural probes in terms of reliable recorded signals and the number of neurons these signals are recorded from [17]. The application of neural prosthetics gains significantly in value if implants remain functional over a patient's lifetime. The literature indicates that there is a strong need for chronic stability of neural probe recordings enhanced from months or years towards decades.

1.3   Research objective and thesis contributions

Histological studies investigating the biological failure mechanisms of chronic neural probes show the formation of a dense sheath of scar tissue and a decreased density of neurons around neural probe shanks. Neurons further away from the shank (on the order of 100 µm) suffer less tissue

reaction [18, 19, 20, 21]. This motivated the hypothesis that deploying electrodes away from the shank (Figure 3) will lead to more stable operation. To avoid extending the inflammation towards the electrodes, they are connected by fine needles, much smaller than the shank. The research objective of this thesis was to develop neural probes with integrated mechanical actuators that are capable of deploying electrodes after insertion.
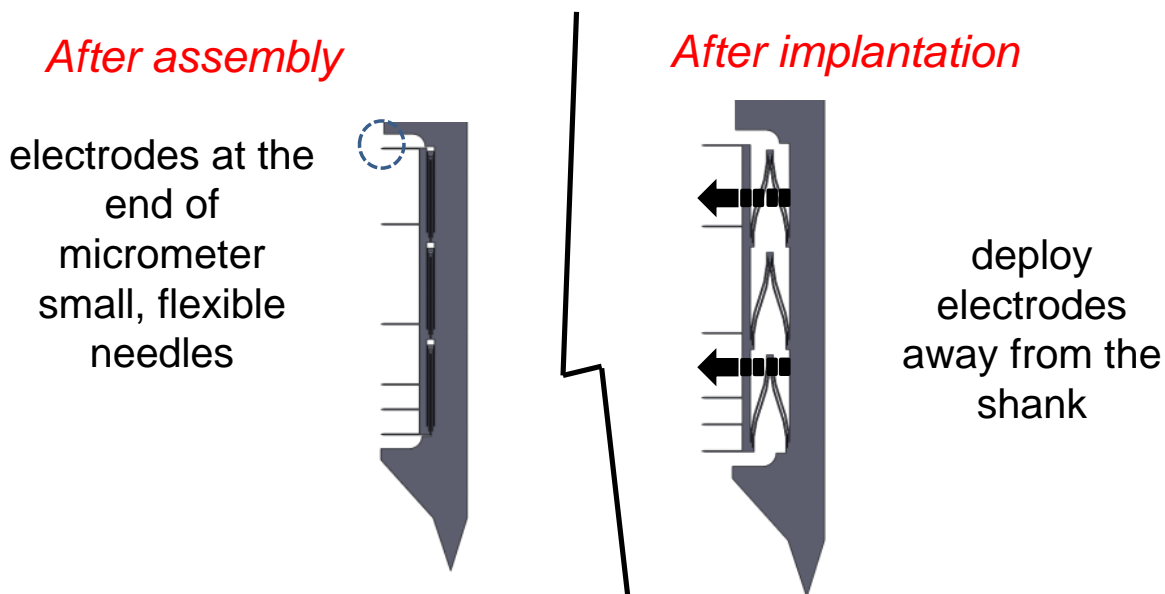
Figure 3: Drawing of neural probes with deployable electrodes. The electrodes are not fabricated directly on the shank but at the end of fine and flexible needles. After implantation, these needles are deployed away from the shank to reach outside a dense sheath of scar tissue, allowing them to interface with more healthy neurons.

There are several benefits this concept is hypothesized to bring with it. Deployed electrodes, or "satellite" electrodes, interface with neurons further away from local inflammation around the shank, physical damage caused by implantation or electrical shielding. Deployed electrodes can be mechanically decoupled from the shank and left floating almost freely with the tissue. Since the

electrode performance becomes less dependent on the shank design, the shanks can then be made larger. Large shanks are sufficiently robust for reliable implantation and handling without breaking, and they can carry channels for drug delivery or optical fibers. However, deploying electrodes is technologically extremely challenging and has so far not been realized in a practical device. The goal of this thesis was to develop technologies and demonstrate the feasible of neural probes with deployable electrodes. The resulting contributions can be introduced as:

- Development of a new class of neural probes with deployable electrodes for improved chronic stability.

- Exploration of starch gel as smart, biodegradable hydrogel for actuation of MEMS.

- Development of Parylene neural probes with integrated stiffeners and sharp tips for improved insertion into cortical tissue.

- Development of a specialized spring design featuring "roll-down" concept. Advantages include intimate contact between surfaces of spring arms which is favorable for operation by hydrogels or capillary action, extremely compact geometry, large travel, large reactive force and robustness.

Chapter II describes the development of fully functional prototypes of neural probes with deployable electrodes. To deploy the electrodes, a novel actuation mechanism based on silicon springs coated with starch hydrogel was developed and tested.

The experiments conducted for Chapter II indicate that starch hydrogel has unique and very useful properties. It can enhance or enable several applications other than deploying electrodes on neural probes. This lead to investigation of more general properties, preparation, processing, and patterning of starch-based hydrogels for use with MEMS, as discussed in Chapter III. In an effort to fabricate neural probes with deploying electrodes, first a Parylene substrate was chosen (and

later abandoned). Chapter IV discusses technologies developed for Parylene-based neural probes. Parylene is a promising material to form neural probes for its longevity and flexibility, but has not been used broadly due to troublesome insertion into tissue. Two mechanisms, namely a method to integrate vertical stiffeners underneath the shank of Parylene probes and a method of creating sharp tips are introduced.

CHAPTER 2

INTRACORTICAL NEURAL PROBES
WITH POST-IMPLANT, SELF-DEPLOYED ELECTRODES
FOR IMPROVED CHRONIC STABILITY

This thesis chapter discusses the development of prototypes of neural probes with the ability to deploy electrodes away from the shank after implantation. Deploying electrodes has been hypothesized to render the recording performance of neural probes less susceptible to an occurring immune reaction. It is technologically extremely challenging and has so far not been achieved in a practical device. Here, an implantable micro actuator was developed that moves a set of electrodes away from the shank after implantation. The actuator consists of silicon springs that are coated with a starch-based hydrogel. The hydrogel retracts and locks the springs before implantation, and gradually releases them when surrounded by bodily fluids as it swells. Models for the actuator were derived, the actuator was characterized in *in-vitro* experiments, and its practicality is demonstrated in an *in-vivo* experiment.

2.1   Introduction

The value of neural probes used in clinical applications increases considerably if they remain functional over a patient's lifetime. Also, only chronic neuroscience experiments can shed light on certain mechanisms. However, the quality and quantity of recorded signals has been shown to decline over time [10, 22]. This has been linked to tissue damage during implantation and

indwelling of the neural probes [23]. The implantation causes mechanical trauma and damages neurons, supporting tissue and the dense vasculature. Indwelling triggers a chronic tissue response in form of inflammation and chronic blood brain barrier disruption [18, 19, 20, 21]. The chronic tissue response leads to encapsulation of the probe shank in a sheath of scar tissue. The sheath of scar tissue decreases the density of neurons, and remaining neurons are getting demyelinated in direct proximity to the probe shank [20]. Since electrical signals strongly decline with distance [24], this leaves less neurons that can be recorded from. The scar tissue has increased electrical impedance [25, 26] what furthermore decreases the signal amplitude.

Following these findings, there were several approaches made to modify neural probes in order to extend their ability to form chronic high quality interfaces. Most of these studies show success to some degree. Some studies used quantitative histology as indicator for chronic inflammation, others used the electrical recordings from electrodes as performance measure. The approaches meant to enhance the chronic stability of neural probes can be divided into mechanical/geometrical, biological or computational modifications. The rest of this paragraph consists of a list of basic findings on how mechanical and geometrical properties of neural probes can be changed to improve the chronic stability of neural probes: It has been shown that the implant size correlates with the extent of the tissue reaction. Small geometries evoke less immune response than larger structures [27, 28]. Neural probes with flexible surfaces, for example those encapsulated in soft hydrogels [29] or consisting of ultra-flexible materials, [30, 31, 32] are hypothesized and in some cases were shown to work better. It was demonstrated that neural probes record more stably if they are not firmly connected to the skull [33]. Extremely slowly or fast inserted neural probes evoked less immune response than those that were inserted at a moderate rate [34]. Biological approaches make use of biologically active drugs. For instance, administering neural adhesion molecules that

promote the growth of neurons towards the electrodes or that demote the inflammation occurring around them. Computational approaches develop decoding algorithms used to generate control signals for prosthesis whose operation is less affected by the decline of the signal amplitude. For example, in [10] it was suggested that decoding threshold-crossing events is more favorable for this purpose than using isolated action potentials. These approaches are often not mutually exclusive and in next generation neural probes several of them can be combined.

Following the finding that extremely small geometries, on the order of a few micrometers, barely or not at all accumulate scar tissue, neural probes were miniaturized to geometries with those dimensions. Table 1 shows a list of neural probe designs that follow this approach. These designs, however, are usually hyper-flexible and fragile and hence hard to insert into tissue. There appears to be an inherent trade-off, mediated by the probe dimensions between tissue damage and the reliability of the insertion. Some of these devices require insertion-aids such as biodissolvable delivery vehicles or insertion shuttles for successful implantation. Furthermore, some electrode designs reduce the shank width at the expense of electrode numbers. The extremely shallow carbon fibers, for example, only support one electrode at their tip. Some applications require recording using multiple electrodes in laminar distribution. Furthermore, some neural interfaces, such as the larger electrodes made for deep brain stimulation or those carrying an optical fiber, are inherently large and cannot be reduced to micrometer fine structures.

Table 1: Overview of intracortical neural probe designs specialized for chronic use by employing subcellular features around electrodes. The acronyms "hist." stand for histology and "rec." stand for recording.

Citation	Implantation aid required	Multiple electrodes per shank	High density arrays	Smallest features reported	*in-vivo* data published
Spring deployed (this)	No	Yes	No	5x5 µm	No
Carbon fibers, Patel '15	Yes	No	Yes	9 µm diameter	Yes (chronic, hist.+ rec.)
Cui '14 [31]	Yes	Yes	No	2.5x4x5 µm	Yes (chronic, hist.)
Open structure, Kipke '07, [28]	No	Yes	No	4x5 µm	Yes (chronic, hist)
Lattice, Tresco '11, [27]	No	Yes	Yes	12x15 µm	Yes (chronic, hist + rec.),
Nanowires, Kotov '15, [35]	No	No	Yes	≈100 nm radius	Yes (acute, rec.)
Silk Fishbone, Yoon '11, [30]	Yes	Yes	No	5x14 µm	No

The strategy followed in this thesis chapter is to deploy very small satellite recording sites to locations outside of the sheath of scar tissue around the shank to connect with neurons that are least affected, all after implantation [36] (Figure 4). The deployed electrodes may then interface with neurons further away from the local inflammation around the shank, the physical damage caused by implantation and the electrical shielding around the shank.
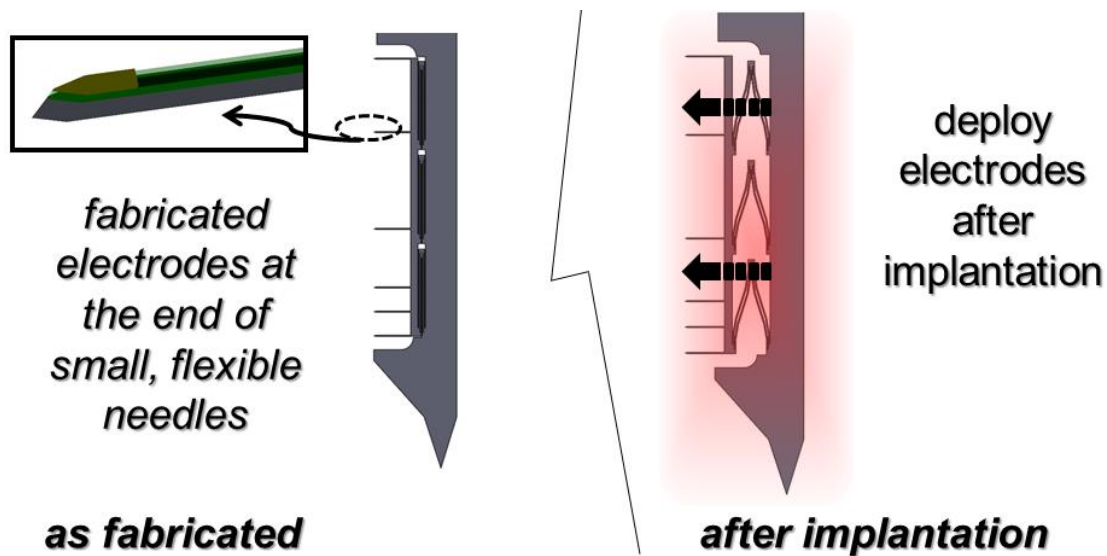
Figure 4: Drawing of the concept of probes with deployed electrodes. The electrodes are not fabricated directly on the shank but at the end of fine and flexible needles. After implantation, these needles are deployed away from the shank.

The electrodes can be mechanically decoupled from the shank and left floating almost freely with the tissue. The shanks on the other hand can then be made sufficiently robust for reliable insertion, to transport larger optical fibers or electrodes for deep brain stimulation, and for handling without breaking. Many approaches were targeted towards mitigating the immune response around shanks, the concept presented in this report makes the performance of electrodes less vulnerable to an immune response around the shank.

Deploying structures of an inserted neural probe shank is technologically extremely challenging since it requires large displacement, force and biocompatibility. It has so far not been realized in a way leading to a device that is optimized for chronic implantation. This thesis chapter reports on developed technologies and fabricated prototypes of feasible neural probes with deployable electrodes.

Mechanical actuation mechanisms were employed previously for operation in conjunction with neural probes in the central and peripheral nervous system. This paragraph reviews three reported actuation concepts, applied in six examples: Bi-stable structures that unfold during implantation, temperature triggered shape memory materials and electrically controlled conjugated polymer actuators (Figure 5). To render fine wire electrodes stiff enough for insertion, they were coated in dissolvable gelatin and designed to fan out during implantation [37] (Figure 5a). To increase the surface of wire electrodes it was suggested to deploy recording spikes after implantation. This could be done by partially retracting a probe with a bi-stable neural probe geometry after insertion [38] (Figure 5b). A similar mechanism (pulling back the neural probe shank after insertion) was suggested in order to deploy wings with electrodes off a polymer electrode [39] (Figure 5c). To allow moving electrodes after implantation to increase selectivity and lifetime of polyimide-based intrafascicular electrodes, the authors of [40] integrated heat-activated shape memory actuators based on TiNi embedded into the core or a shank (Figure 5d). Actuators were attached to the back of a neural probe shank allowing extremely slow implantation, for example using as epoxy-based shape memory materials [34] (Figure 5e). Parylene neural probe shanks were equipped with electrode projections that deploy during insertion. Conjugated polymer actuators were used to flex these projections inside before insertion and deactivated as the shank is inserted [41] (Figure 5f).
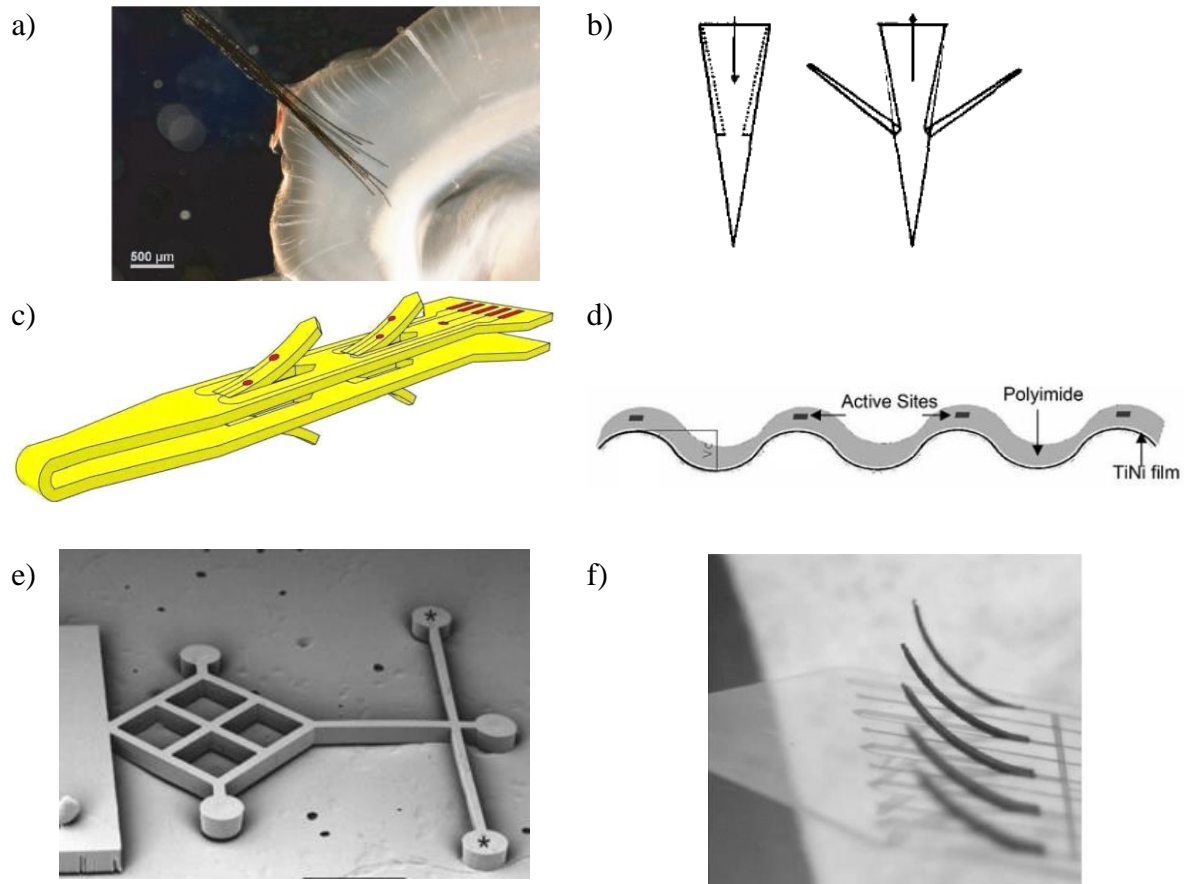
Figure 5: Illustrations of neural probe actuation mechanisms. a) gelatin embedded wire bundles [37], b) bi-stable recording tips [38], c) self-opening Parylene neural probe [39], d) and e) shape memory actuators [40, 34], f) conjugated polymer actuators on Parylene neural probes [41]

A thought experiment suggests that there are preferable properties of actuation mechanisms for neural probes with deploying electrodes. If the connection to the electrodes softens or releases after deployment, they can better comply with the movement of tissue relative to the shank. Surgical procedures are critical and should not be unnecessarily complicated. The electrodes should only be surrounded by micrometer fine structures to mitigate built up of scar tissue. A straight deployment trajectory aligned with the geometry of the deploying structure minimizes

17

tissue damage compared to a curved trajectory or slicing. The actuator, furthermore, should not take up much space or enlarge the shank of the neural probe much. To the knowledge of the author, these properties have not been realized in any actuation concept employed to neural probes.

Addressing these needs, this thesis chapter introduces an actuation mechanism based on hydrogels. Soft-actuators make use of the large and forceful change of geometry in hydrogels after coming into contact with water [42]. Such self-actuated materials can operate without control signals and electrical connections. Actuators made of resorbable hydrogels will reduce their volume after implantation and become soft. This thesis chapter revolves around design and fabrication of neural probes with integrated silicon springs that are coated in a starch-based hydrogel to deploy electrodes.

2.2   Concept of electrode actuation

Deploying electrodes poses two main performance requirements on the actuator: how far it should be able to deploy the electrodes and how fast it should do that. To interface with healthy neurons, the electrodes should be deployed far enough to reach outside the layers of tissue damaged by implantation and presence of the shank. For that the actuator needs to supply sufficient force throughout the required travel to advance the electrodes through the surrounding tissue.

This paragraph discusses the choice of the amount of travel the actuator should support. This is to answer the question at what distance from the implanted shank the recording quality of the electrodes would be sufficiently less affected. This is a criterion difficult to determine. It is still not fully understood which and to what extent mechanisms lead to recording failure. Possible failure mechanisms include high impedance scar tissue and neural death or damage. These depend on many factors including shank size, anchoring or insertion method. The extent of the foreign

body response depends on the size and anchoring of the implanted device [28, 33, 27]. The health of neurons likely depends on many factors such as the density of nearby inflammatory cells, density of surrounding neurons and concentration of inflammatory factors. Histological studies like [20, 43] investigated the geometry of the immune response around silicon probes implanted for up to 12 weeks into rat brains. The authors of [43] used silicon neural probes with 200 μm width at the base, tapering down to 2 μm at the tip. The probes were firmly anchored to the skull for their quantitative histological study. The experiments show that the density of neurons (cells per volume) within 50 μm of the shank tissue interface drops by roughly 60 %, but recovers to normal in a bin further away (50-100 μm). Activated microglia and macrophages are present in high concentrations within 80 um of the shank. Other components of the immune response such as hypertrophic astrocytes extend several hundred microns into the tissue [44]. The authors of [28, 33, 27] show that smaller implants evoke a more contained immune reaction. For example, the scar tissue around probe shanks reduced to a 15 μm wide lattice only extends by several tens of μm, while solid shanks are surrounded by more than 100 μm of scar tissue [27]. In conclusion, above mentioned studies suggest that if the developed neural probes are 200 μm wide at the base, tapering towards the tip and 15 μm thick and anchored to the skull, for the electrodes to record from outside the dense sheath of scar tissue formed around implanted shanks and from tissue with a density of neurons comparable to that found in brains without implanted shanks, they need to deploy by more than 100 μm. The design goal for the travel of the actuator is set to be at least 100 μm.

The actuation mechanism should delay deployment or be slow enough such that the probe can be fully inserted before the electrodes move outside the protected position. The speed of deployment should be chosen such that the tissue response is minimized. The time it takes for a probe shank to

19

be fully inserted depends on the insertion speed and depth. A wide range of insertion speeds is employed. Its choice depends on inserted device and type of tissue. For example, pneumatic insertion is extremely fast ($\approx$10 m / s) and commonly used with Blackrock Uath Arrays [45]. The tissue response of neural probes inserted at 0.82 mm/s and 1 mm/40 min was compared in [34]. They concluded that the extremely slow insertion speed reduced astrocytosis, a component of the foreign body response. The authors of [46] compared the effect of two insertion speeds on long-term tissue response. A Parylene-coated silicon probe was implanted into rat brains at 10 µm/s and 100 µm/s, to a depth of 9 mm. The tissue response after 6 weeks showed no difference between the two insertion speeds. This literature review indicates that the range of practical insertion durations is wide and ranges from extremely fast (few ms) to extremely slow (hours). The design goal for the onset/speed of actuation was set such that the actuator would not deploy for several tens of seconds to allow for insertion with a reasonable speed and then deploy slowly within several tens of minutes to hours, in order to minimize tissue damage. The selected goals for the actuator performance are summarized in Table 2.

Table 2: Summary of chosen actuator requirements

Actuator requirements	
Travel	more than 100 µm to deploy outside sheath of dense scar tissue
Timing	deploy slowly enough/delayed to allow for implantation (several tens of seconds)
Biocompatibility	occupy tolerable volume, operate in isotonic liquid no excessive heat, no high voltages, no toxic materials

The concept of the designed actuator is as follows (Figure 6): The electrodes of the neural probes are at the tip of needles that are connected to a shank through micro-springs. Before implantation, the springs are coated with a hydrogel that retracts the springs as it dehydrates. After implantation, the gel comes in contact with bodily fluids and slowly releases the springs, allowing them to deploy the electrodes (Figure 6).
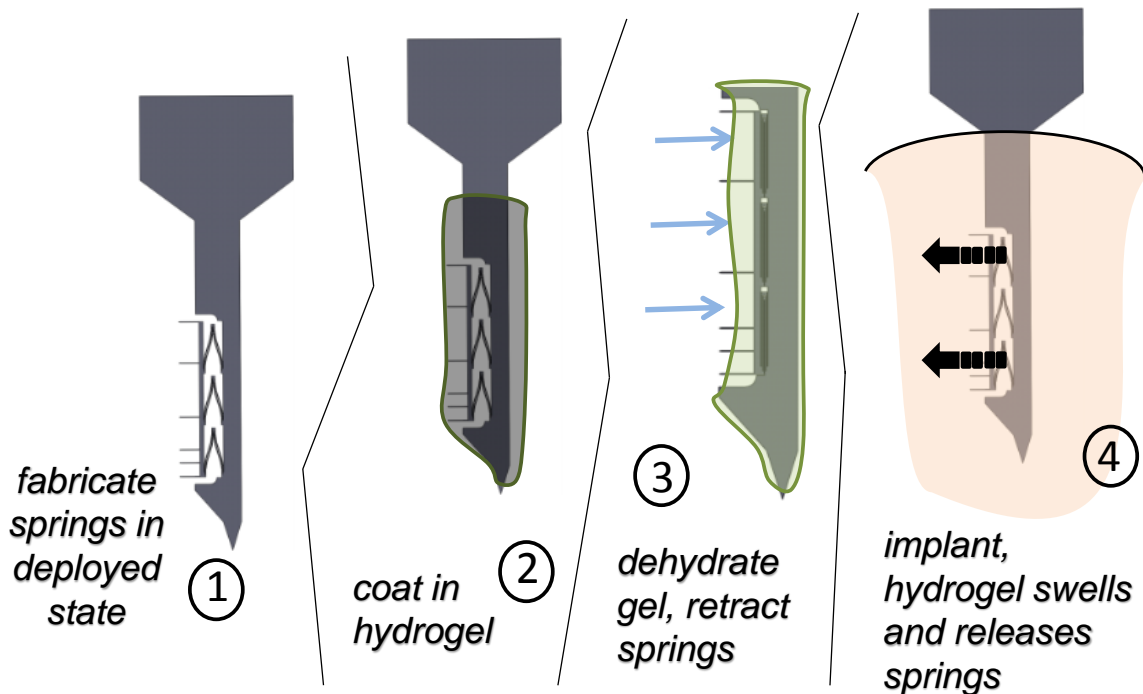
Figure 6: 1. The probes are fabricated with springs in deployed state. 2. The springs are coated with a hydrogel. 3. As the hydrogel dehydrates, the springs retract, pulling the electrodes into a protected position close to the shank. 4. After implantation the hydrogel swells releasing the springs deploy and interface tissue away from the shank.

The advantages of this actuation concept are that there is no need for external control signals, extra interconnects or a power supply. Furthermore, the actuation does not require changing the temperature of the surrounding tissue, applying voltages or using chemically reacting materials.

The springs are extremely compliant when fully deflected. In that state, they leave the electrodes floating almost freely inside tissue. The electrodes deploy in a straight trajectory. This minimizes the footprint of the deploying structures and likely causes less tissue damage that a curved trajectory or slicing.

2.3   Spring design

When designing springs, there are two properties to consider that likely have conflicting effects: The amount of space the springs take up scales with the number of electrical contacts they can support. The mechanical stress occurring during retracting of the springs (which needs to be provided by the hydrogel) scales with the force they provide to push the needles through tissue.

Following design goals were made for the springs:

- provide required travel and force

- take up little volume, do not extend the shank width much

- carry the electrical interconnects from the electrodes to the shank

- allow to be retracted and released by a hydrogel

A special spring design was developed that alleviates the above mentioned trade-offs. To get better insight in the developed design, a mechanical model of the spring deflection was developed.

The springs consist of silicon and carry an electrically conductive trace on top that is insulated against the surrounding. One spring arm consists of two arcs facing in opposite directions (Figure 7). Rather than bending across an anchor like a fixed-free beam loaded at the free end, they roll down on the shank and on the comb holding the needles as they deflect. This creates a uniform stress distribution along their length when deflected, allowing for large deflections without fracture (Figure 7). This also provides the hydrogel a large surface area to pull on. Capillary action has

larger effect on surfaces being in close contact. Instead of increasing the width of springs to fit multiple interconnects side-by-side on a single spring arm, several springs with small width are nested inside each other, and each carrying a single interconnect. Figure 8 shows the assembly of spring arms into sets of springs and typical dimensions of spring arms.

a)
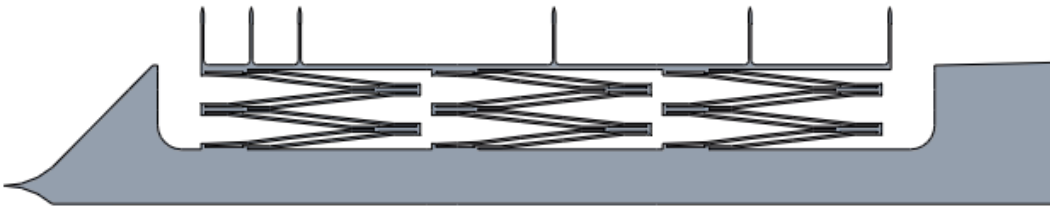
The complete set of springs consists of three pairs of two nested springs connected in parallel.
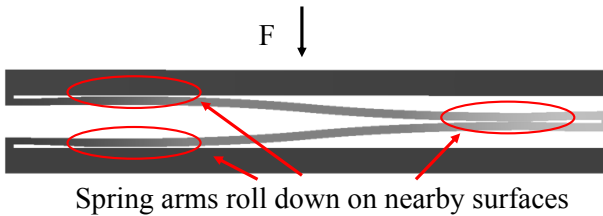
b)   c)
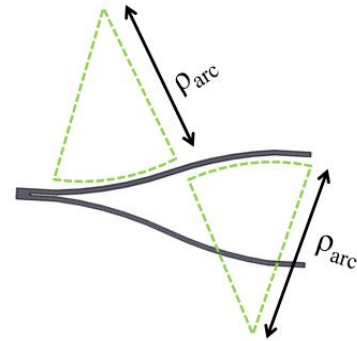
Figure 7: Drawings illustrating spring design and operation. a) A probe shank with a set of double-folded, double-nested springs b) A spring arm rolling down on a substrate as it retracts c) A spring arm consists of two connected arcs with a constant radius of curvature.

a)

A set of springs consists of a parallel connection of a serial connection of two spring arms

b)

60 μm

5 μm

344 μm

Two spring arms in serial connection
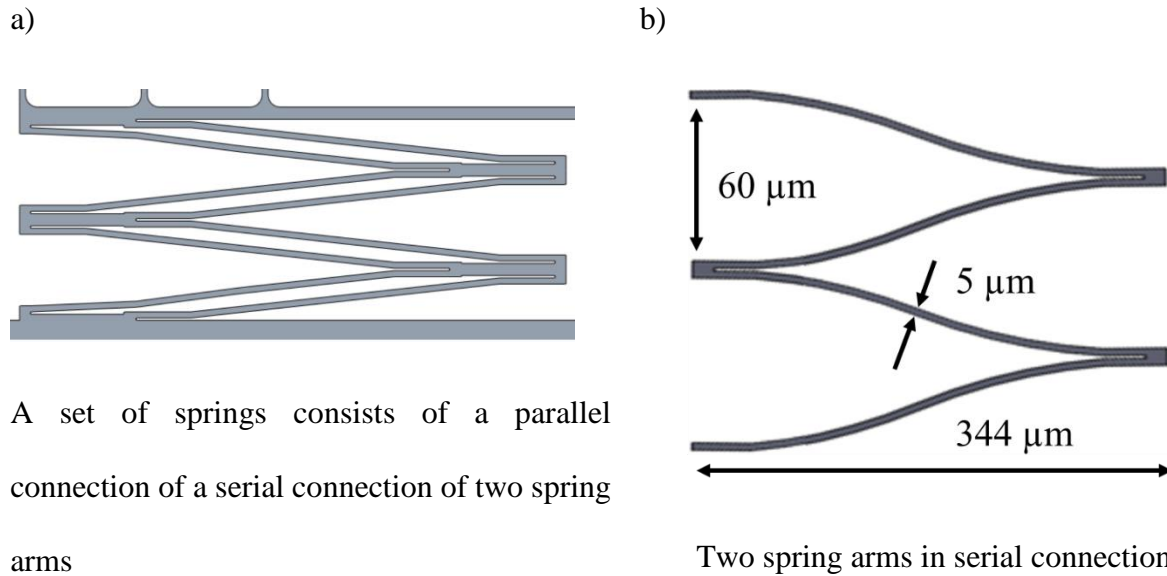
Figure 8: Spring assembly a) the label "set of springs" refers to a parallel connection of a serial connection of two spring arms. b) typical dimensions of two spring arms in serial connection.

The springs should not exceed fracture stress during retraction. The stress during deflection of the springs is maximum when they are fully retracted; in that state the arced shaped spring arm rolls on the supporting structure to a straight shape. It can be approximated by equation (1):

$$\sigma_{max} = \frac{E \times h}{2 \times \rho_{arc}}$$

(1)

With E - the Young's modulus, h – the width of the springs and ρ_{arc} – the radius of curvature of the arc. This yields the design implication that, in order to minimize the distance to the neutral plane, the width of the springs needs to be minimized. The minimum width of the spring is limited by the photolithographic minimum feature sizes and by the minimum required force the springs should exert to push the needles through tissue and starch gel (which increases with the spring width). Likewise, increasing the radius of curvature will decrease the maximum stress in the springs, but it will lower the travel for a given arc length and exerted force.

The force the springs exert at a given deflection determines how far they can deploy the needles through tissue. To approximate the force-displacement relation of the springs, a model based on the Euler-Bernoulli beam theory is derived [47]. Conclusions from the derived numerical model were calculated and plotted using Matlab (Mathworks, Natick, MA). One spring arm is modeled as a beam with fixed-guided support, deforming under a point load. A beam with fixed-guided support is modeled as a beam with half the length and fixed-free support (Figure 9). The spring is anchored only at its end. The tethering forces can be approximated by a point-load applied to the end of the spring arm.
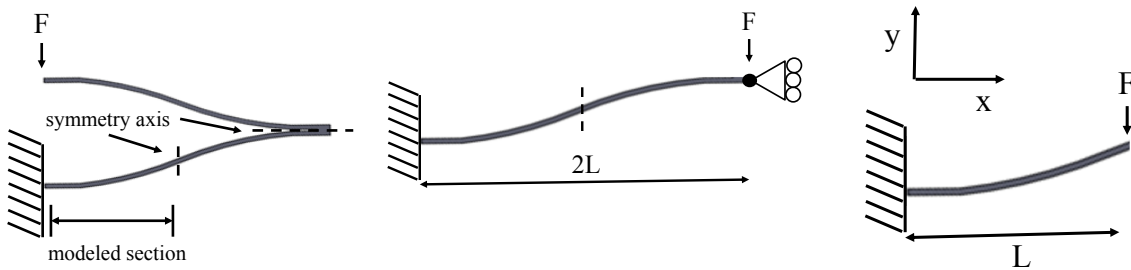
Figure 9: Modeled section of the spring arm. Four arcs in series forming one spring arm. Under the given boundary conditions, two arcs behave similar to a fixed-guided beam with twice their length. Modeling the deflection of one single arc is sufficient to describe the behavior of the set of springs. A single arc behaves similar to a fixed-free beam.

For the beam to reach equilibrium, the applied external moment needs to be matched at every section along the beam by a reactive internal moment (equation (2)). The external moment of a section is proportional to the magnitude of a point load applied to the tip of the beam and to the distance of the segment to the tip of the beam (equation (3). The internal moment is proportional to the stiffness of the beam material, its bending moment of inertia, and to the inverse of the

induced radius of curvature in that segment (equation (4). The beam is modeled to have a rectangular cross-section. Thus the bending moment of inertia is uniform along the length of the beam and can be calculated using equation (5).

$$M_{ext} = M_{int} \qquad (2)$$

$$M_{ext} = F \times (L - x) \qquad (3)$$

$$M_{int} = \frac{E \times I}{\rho(x)} \qquad (4)$$

$$I = \frac{b \times h^3}{12} \qquad (5)$$

M_{ext} and M_{int} are the external and internal moments resulting from applied force F, $\rho(x)$ the curvature of beam at position x induced by the external load and I is the bending moment of inertia of the beam.

This set of equations calculates the bending moment of inertia of the spring arms assuming a constant projected cross-section along their length. However, for large deflections or for pre-curved beams with length that is comparable to their radius, this assumption is wrong. In the designs modeled, the change of projected thickness is small and hence neglected. It can be included with a minor modification when needed. Since the bending moment of inertia will then be dependent on the final beam shape, solving the differential equation can be done by iteration. The thickness of the beam needs to be changed to its projection, as shown in Figure 10b and in equation (6).
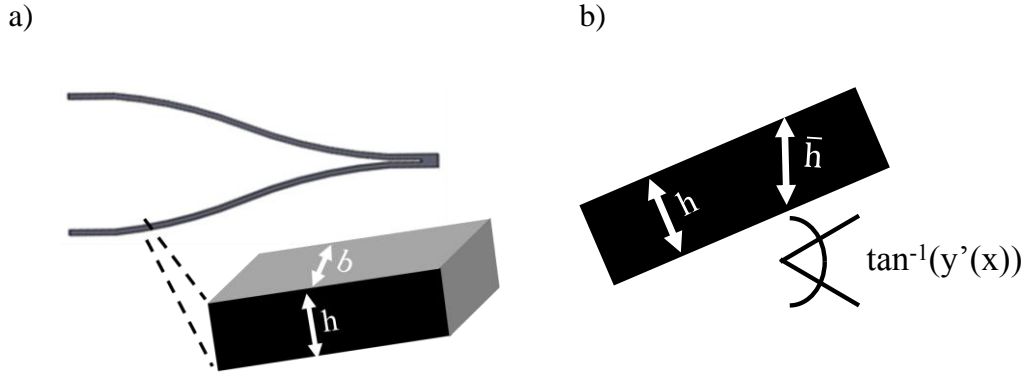
Figure 10: a) spring dimensions with h, the width, and b, the thickness of springs. b) $\bar{h}$ is the projected width adjusting for the curvature.

The projection $\bar{h}(x)$ can be calculated by equation (6):

$$\bar{h}(x) = \frac{h}{\cos(\tan^{-1}(y'(x)))} \qquad (6)$$

To include the effect of the spring rolling on the shank, the curvature ρ(x) is capped to that of the pre-curvature of the arc. If an applied force would curve a section of the spring further than its built-in curvature in the opposite direction, this section will only deflect to a straight shape equation, as described in equation (7). At this point it comes into contact with the support structure and the deflection is stopped.

$$y''(x) = \begin{cases} \dfrac{1}{\rho(x)} \ for \ \rho(x) < \ \rho_{arc} \\ \dfrac{1}{\rho_{arc}} \ else \end{cases} \qquad (7)$$

$y''(x)$ stands for the second derivative of y, the position of the neutral plane of the spring at location x, with respect to x.

The beam deflection y is derived from the curvature y'' by integration using appropriate boundary conditions: zero slope and zero deflection at the fixed end (y'(x=0) = 0 and y(x=0) = 0).

The deflected beam shape for a given load is calculated by superimposing the built-in, arc shaped form of the spring without any load, to the deflection calculated as described above (equation (8)).

$$\bar{y}(x) = y(x) + \rho_{arc} \times (1 - \cos(\sin^{-1}(\frac{x}{\rho_{arc}})))$$
(8)

To provide an example, these equations were solved for a spring with typical dimensions. The Young's modulus of silicon is assumed to be 159 GPa [48]. Solving for $\bar{y}$ with ρ_{arc}=1000 µm, L=173 µm, h=10 µm, w=5 µm, and applying a load of 500 µN at the free end of the beam yields following figures: Figure 11 contrasts the curvature of a fixed free beam with and without support (curvature not capped). Under the applied load, the maximum stress (close to the anchor and at the top of the beam) in the supported spring arm is with -380 MPa much smaller than the 2.1 GPa in the unsupported beam.
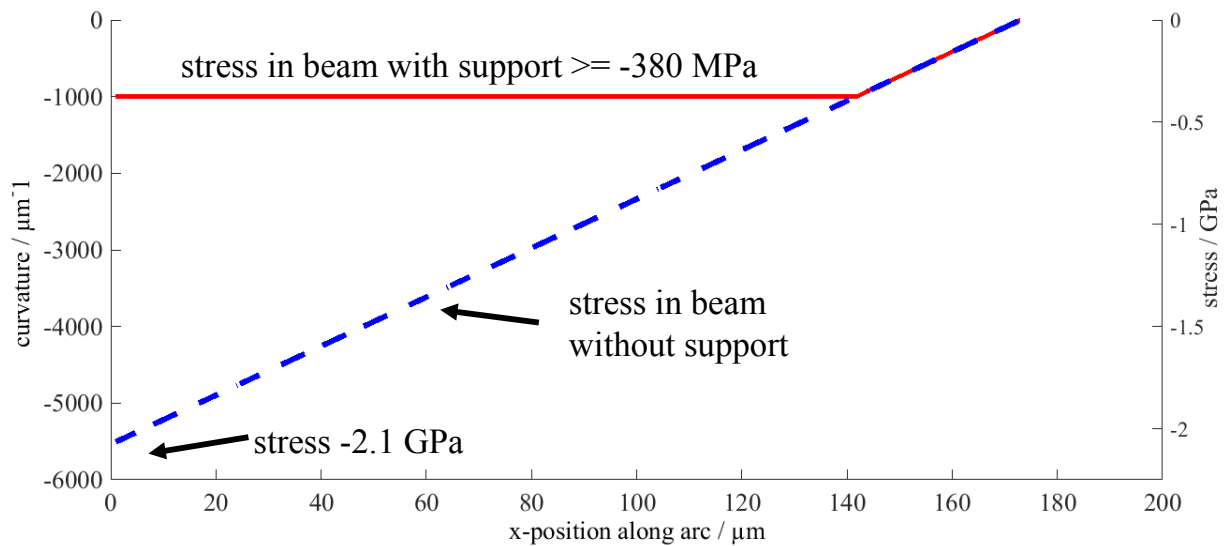
Figure 11: The modeled curvature and maximum stress of two pre-curved, fixed-free beams under applied load. One of the beams rolls down on a support (red, solid). The other one bends freely (blue, dashed). As the beam rolls on the support, its curvature (and with it the stress) is capped. The maximum curvature is dictated by the inverse initial curvature of the beam. Without support, the curvature increases linearly along the length of the beam.

Figure 12 shows the deflection of the beams. The figure indicate that the supported beam can exert a larger force at the same displacement. Figure 13 shows the resulting beam shapes using he deflection shown in Figure 12. Figure 13 is generated by superimposing the deflections to the built-in, curved shape of the beams.
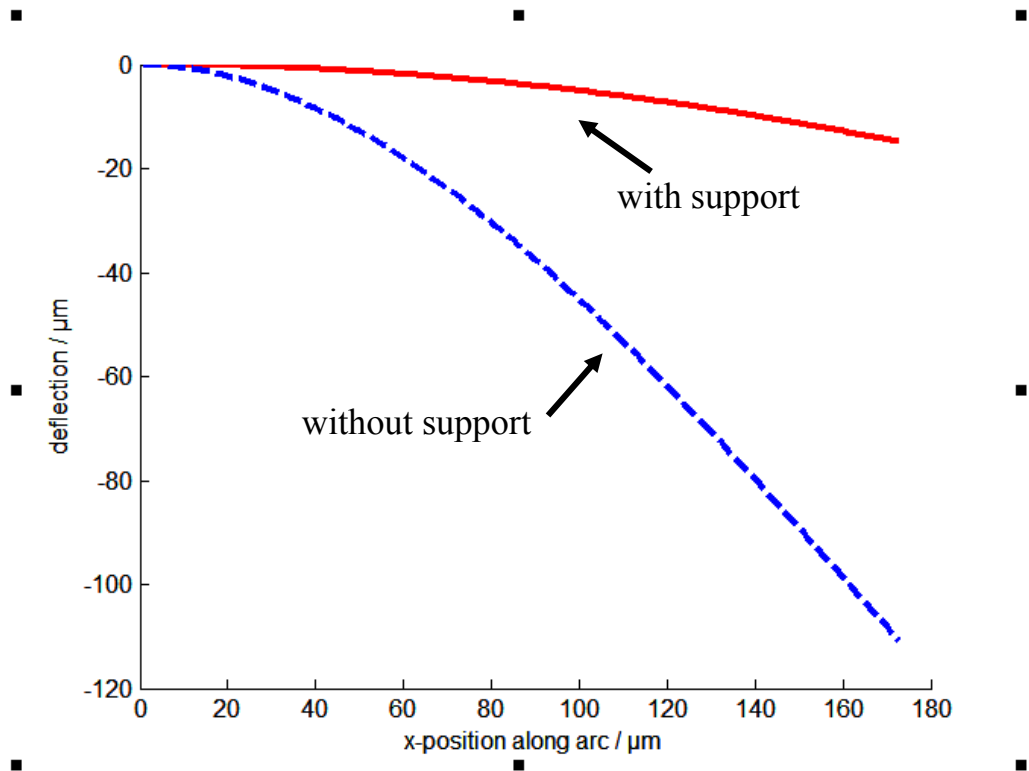
Figure 12: Deflected distance along the length of two fixed-free beams loaded with 500 μN. Again, one of the beams rolls down on a support (red, solid), the other one does not (blue, dashed). Without support, the deflection of the beam is strongly increased.
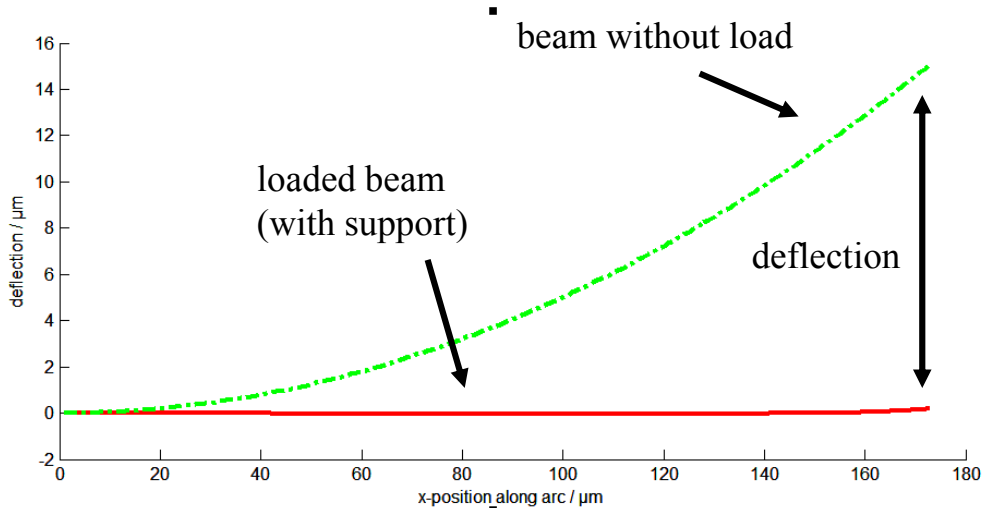
Figure 13: Shapes of a pre-curved beam with and without applied load (500μN), rolling on a support. The difference of the tip positions is taken as the deflection of the beam. This corresponds to the distance this spring segment can deploy the electrodes.

Figure 14 shows the load-deflection curve of a set of six springs in parallel, as used on the developed neural probes. Each spring consists of eight arcs in series. The load-deflection curve is non-linear, the springs are relatively soft when deployed and stiff when retracted. The springs will be inserted in retracted state (high deflection) where they exert the highest force. As they deploy after insertion, their force decreases until it matches the force exerted by surrounding tissue. For example, if the force needed to pierce tissue was 0.2 mN, the springs will deploy by 90 μm from their retracted position. The slope of the curve at low deflections indicates that springs become softer after deploying. The softer the springs are, the less resistance they offer the electrodes to 'float' with the tissue. When the springs are retracted, they increase their stiffness. This provides sufficient force to pierce the needles through tissue.

31
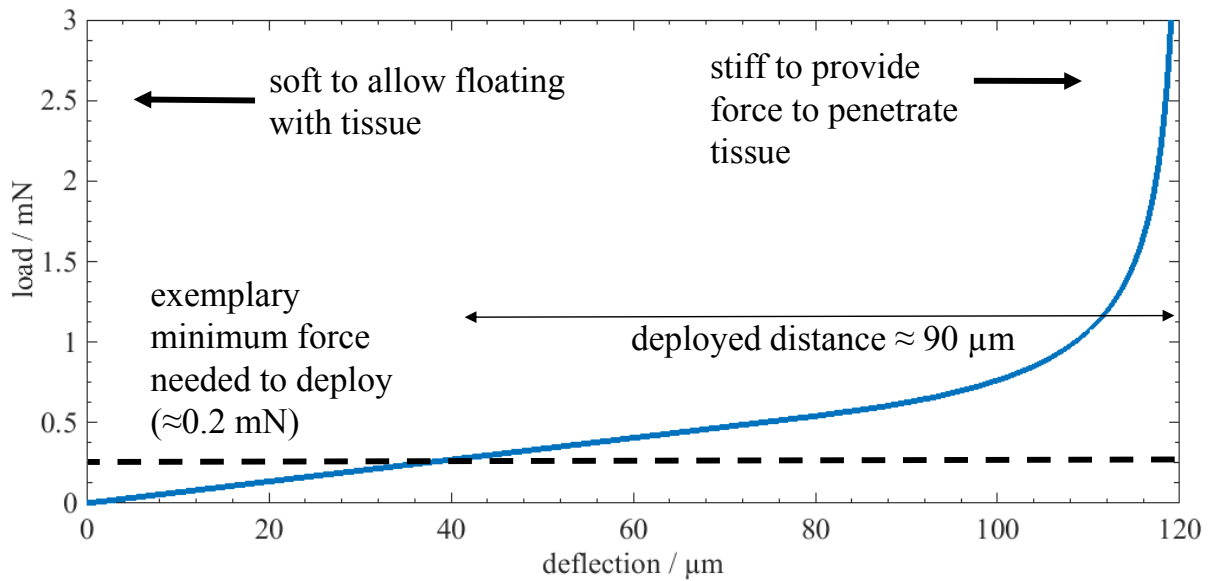
Figure 14: Modeled load-deflection curve of a complete set of springs (eight arcs in series form one set of spring arms, six spring arms are connected in parallel). The load-deflection curve is non-linear. The springs are relatively soft when deflected, and relatively stiff when retracted. Softness allows the deployed electrodes to float with tissue. Stiffness provides sufficient force to advance electrodes through tissue.

Table 3 summarizes some calculated properties of one of the fabricated spring designs.

Table 3: Calculated/Designed spring specifications

Parameter	*Force when 90% retracted / spring constant at low deflections*	*Length/ thickness/ width*	*Maximum deflection*	*Max.stress in springs (on surface, when fully retracted)*
Provided in a fabricated example	0.96 mN / 6.9 N/m	346 μm/ 10 μm/ 5 μm	120 μm	0.425 GPa (fracture stress of silicon ≈2.8 GPa [49])

As described in paragraph 3.4 concerning starch-hydrogels compressing springs, the compression was strong enough to crack springs in characteristic locations close to an the edge. At the edges of the springs, the spring arms are close to another surface, allowing the starch gel to "pull on". The springs were redesigned with two modifications to prevent them from forming cracks (Figure 15). Larger openings between spring arms were avoided such that they come into contact and stop bending before cracking occurs. Also, all corners of the spring arms were rounded to relieve stress.
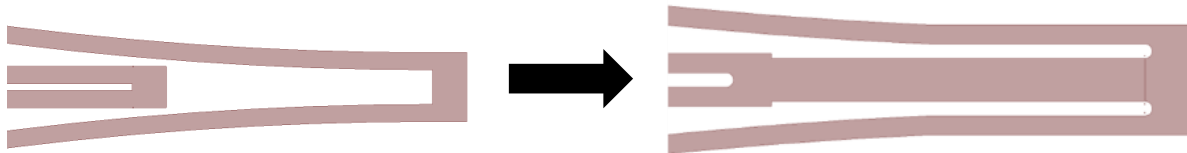
Figure 15: Sketch of an early spring design that often cracked when retracted by starch. Two design modifications prevented that: A structure was added that allows the spring arms to roll down on, close to the edges, and all corners were rounded.

An early attempt to form springs in a similar design in Parylene was abandoned for two reasons: Experiments on Parylene springs (Figure 16a), retracted by manipulators, showed that Parylene spring arms tend to stick together once they came into contact. Also, Parylene formed cracks very easily when under mechanical stress, especially along edges that were rough as a side-effect from fabrication (Figure 16b).

a)   b)
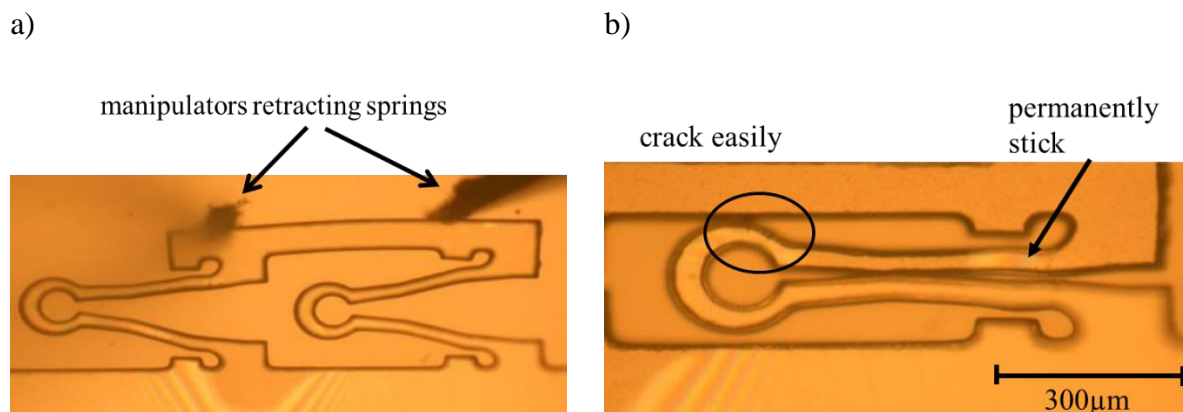
Figure 16: Parylene springs retracted by manipulators formed cracks and often suffered stiction.

2.4   Starch-hydrogels for actuation of springs

A mechanisms needed to be found to retract and lock the springs before insertion, and to release them after. Several mechanisms were considered for this purpose, including the capillary action of water, electrowetting, external manipulators and biodissolvable glues or hydrogels.

Relatively weak springs can be retracted with capillary action of pure water. As they were immersed in water, they trapped small amounts of water between adjacent surfaces. When the water began to evaporate, the springs retracted, leaving only a thin film of water in between surfaces. When the retracted springs were immersed into water, the capillary action disappeared and the springs released. The capillary action of water was only able to retract springs as shallow as 2 μm. This seemed not practical, considering that the springs need to be strong enough to deploy the electrodes through tissue.

Electrowetting bases on changes the contact angle of a water drop on a dielectric from the Young's angle to the electrowetted contact angle [50]. This can be used to form actuators with large force and travel. The actuation mechanism would take advantage of capillary forces of water attracting a surface, and use electrowetting to move the water. To apply this concept to actuation of springs, however, would require to form dielectrics and electrodes along the sidewall of the springs. This would change the used fabrication process drastically.

Another option considered was the use a combination of external manipulators to retract the springs and glues to lock and release them. There are various dissolvable glues, for example sugar syrup, polyethylene-glycol or poly(lactic-*co*-glycolic acid) (PLGA). These would release the springs after insertion, once biological fluids dissolved the glue. However, employing external manipulators appeared to likely require much individual handling of the delicate structures of the

probes. Also, the required access to those structures then limits their design. Furthermore, the used glues either released the springs immediately after contact with water (sugar syrup, polyethylene-glycol) or unevenly, meaning one side long before the other, (PLGA) when in contact with water. One reason for this uneven release could be that the glues used had a relatively long dissolution time (hours). So a small variation in thickness or composition of the glue can have a large effect on the mechanics of the spring release.

Several hydrogels were investigated for their ability to retract and release the springs. Agar, gelatin, glycogen and polyethylene glycol were dip-coated on the springs. They were able to retract weak springs, but released them instantaneously when in contact with water. Hydrogels based on various origins of starch such as corn rice, tapioca or potato plants were also investigated. Only corn starch was able to fully retract springs that were likely strong enough to deploy sufficiently far through tissue. Hence corn starch was further investigated. For the experiments, a modified corn starch called "Crisp Film Starch" obtained from National Starch was used. Pure starch releases the springs readily when in contact with water at body temperature. It was found that iodizing the starch gel leads to it swelling slowly and gradually. A detailed explanation of the phenomenon is discussed in Chapter 3. Although iodine can have a beneficial effect on wound healing [51], free iodine is cytotoxic, increasing with its concentration. To reduce the concentration of free iodine, Povidone iodine (an iodine slow-release agent) [51] is used for iodizing.

It is critical that the springs do not deploy much during insertion. Iodized, starch coated springs deploy with an initial jump right after coming in contact with water as explained in paragraph 3.6 . To minimize this initial jump, PLGA is coated on top of the iodized starch. PLGA is a FDA-approved, biodissolvable material that has been used as neural drug-delivery vehicle [52] and in conjunction with neural probes as dissolving scaffold [52]. A sketch of the assembly used is show

in Figure 17, along with explanations of the function of the individual components. In summary, the springs are meant to provide the force to deploy the electrodes, starch gel is used to retract the springs and to slow their deployment, and PLGA is used to delay the deploy of the springs sufficiently to allow for complete insertion.

PLGA
(delay
release)

starch
(retract,
slow release)

Springs
(deploy)

Figure 17: Sketch illustrating intended function and location of starch and PLGA on the springs.

Starch-hydrogel needs to be sterilized before implantation when used with chronic, biological experiments or any in clinical applications. Biodissolvable materials are often hard to sterilize because they tend to be soluble in water, heat-sensitive, radiation sensitive and to absorb toxic chemicals. However, in case of starch-hydrogel, there might be a few options to address the requirement of sterilization: It is likely useful that starch is used in conjunction with iodine. Iodine has been used as antiseptic in clinical applications [53]. Furthermore, starch hydrogel appears to still fulfill its desired function even after exposure to hot air (100 °C) for 10 min (data shown in section 3.6). Another possibility is to sterilize the starch-granules before preparing the gel. Experiments showed (data not shown) that starch granules can be exposed to air at 160 °C for 30 min without losing the ability to form a gel.

Table 4 compares the developed actuator to two other autonomous, implantable actuators. It is somewhat difficult to compare actuation mechanisms relying on published designs since they were likely optimized for different applications. One apparent property of starch-gel is that it does not take up much volume and hence is favorable for implantation. It is furthermore biodissolvable, what can be an advantage. In case of the epoxy shape memory and the bilayer actuators, the onset

of actuation after contact with biological tissue is not documented in sufficiently high resolution (seconds) to determine if they would be able to provide sufficient delay for insertion of neural probes. As is seems, this is not the case and considerable actuation commences right away. The epoxy shape memory actuation shows potential for large travel (several hundred micrometers, depending on beam dimensions). This mechanism is furthermore providing actuation in the direction of lateral translation, what might be preferable in case of deploying electrodes of neural probe. The bilayer actuators can be made extremely small. With the proposed fabrication process, they can only provide out-of-plane rotation.

Table 4: Biocompatible, temperature triggered, autonomous, large displacement micro actuators and some of their typical/published properties

Author, Reference, Material	Translation / Rotation	Force	Speed / Delay	Softening when deployed	typical size of active layer
(This work) Starch-gel coated springs	120 µm Translation	200 µN at 120 µm deflection	20 s onset – hrs for full deployment	Yes	5 µm thick before, tens of µm after hydration
Restrepo '06), [34], epoxy shape memory	400 µm, Translation	100 µN	Exponential with time, ≈ 100 µm after 1hr	No	100 x 200 µm
Gracias '08, [72], bi-layer Cr/Cu, cresnel novolak	> 90 ° Rotation	Can cut connective tissue	Not published, presumably seconds	No	7 µm thick

2.5   Needles and shank design

The dimensions of the needles result from a compromise between small size for reduced tissue encapsulation, minimum features given by fabrication limitations and required mechanical stability. As mentioned earlier, the biological encapsulation reduces strongly around implants with sub-cellular size (5-10 μm) [27, 28, 33, 54, 55]. A lower limit for the width and thickness of the needles is given by the ability to pattern and align a conductor across the needle with enough clearance to each side such that it can be covered from all sides with an insulator. The needles can be very flexible, since the tissue inside the brain is not offering much mechanical resistance. However, if the needles become too flimsy, the deployment might not happen in a straight trajectory and needles could buckle and break during insertion or starch dehydration. The needles along with the springs used in the experiments are designed to be 5 μm wide and 5 or 10 μm thick for reliable and simple fabrication. More shallow designs with 2 μm width and 5 μm thickness were also fabricated. Needle designs up to an order of magnitude smaller are possible using e-beam lithography [56]. The length of the needles is set to be 100 μm such the electrodes are able to reach outside the encapsulation sheath around the shank.

The shank needs to be wide enough to harbor the electrical interconnects, springs, needles and electrodes. It also needs to provide sufficient stiffness to penetrate through tissue. The main contributors of the width of the shank are the needles and the springs. The stiffness of the shank, required for reliable insertion, can be enhanced without increasing the width much. For example by forming vertical stiffeners [57]. Electrical interconnects can be patterned on silicon with sub-micron pitch [56] so the shank width will not increase by more than a few microns per interconnect. A wider shank will induce a larger inflammation, and lower the acceptable pitch to neighboring shanks. If the width of the shank can be reduced, the electrodes likely do not need to be deployed

as far. A more shallow shank is preferable because it minimizes the overall tissue damage and it allows for other shanks to be implanted in closer proximity. An optimum shank design will be as shallow as possible while still deploying the electrodes just outside the sheath of scar tissue.

The above mentioned minimization of the shank width was out of scope for this thesis; a shank width sufficient for reliable insertion is chosen (Figure 18). The spring configuration employed for the design used in the described experiments adds about 50 µm width to the shank (cumulative width of the spring beams in retracted position). The needles add 100 µm. The rest of the shank is designed to be 140 µm wide.
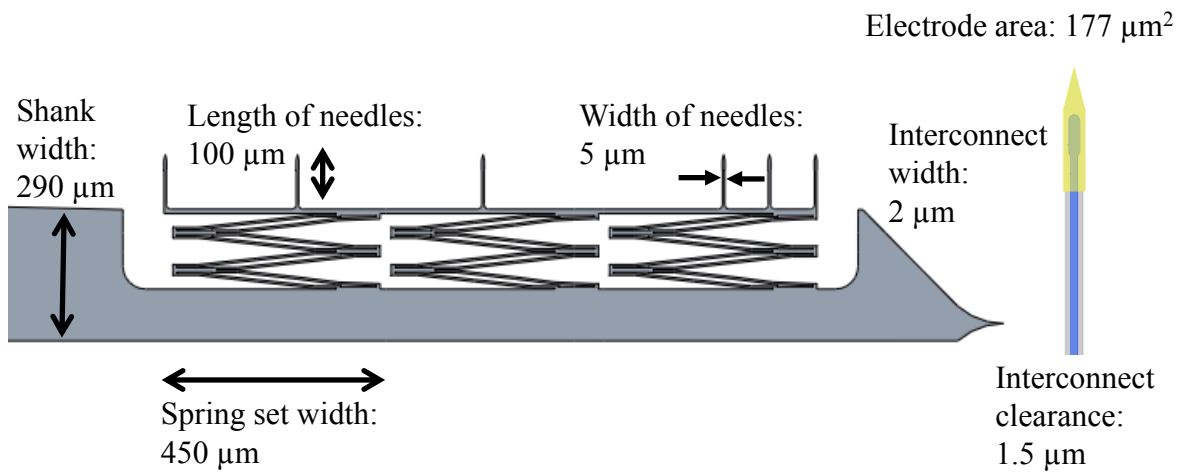
Figure 18: Neural probe dimensions chosen for most of the experimental work.

Other designs were fabricated as well. In some, the shank width was reduced together with the distance the electrodes deploy, resulting in dimensions shown in Figure 19a. Another design increased the electrode count to 16 (Figure 19b).

a)

Needle length: 45 μm   Spring travel: 50 μm

Shank width: 100 μm

b)

16 Electrodes

Shank width: 270 μm
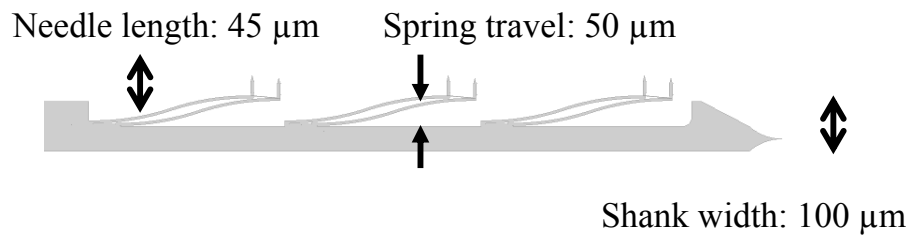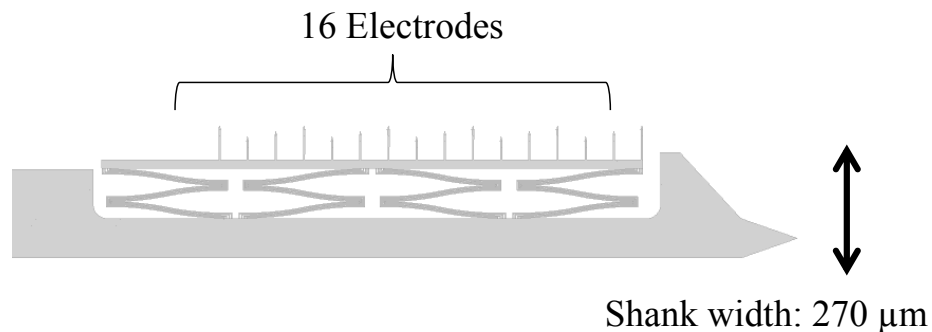
Figure 19: a) Shank dimensions of a more shallow design. The width was reduced at the cost of reducing the deployed distance. b) Layout of a shank with 16 deployable electrodes. Both designs were fabricated and are electrically functional.

2.6   Finite-element model of the tissue stress induced by neural probes with deployed electrodes

Motivation

Deploying electrodes after implantation might improve chronic stability if the scar tissue around the deployed electrodes is reduced compared to that accumulating around the shank. It seems plausible that reducing the mechanical stress that neural probes induce into the surrounding tissue (caused by respiration, pulse, head movements) will reduce the amount of scar tissue accumulated.

It was hypothesized, and in some cases found, that neural probes, that are not firmly anchored to the skull [33], and flexible neural probes [30, 31, 32], reduce some components of the tissue response. For this thesis project, a FEM simulation was conducted to analyze the effect of springs and fine needles on the mechanical stress induced into tissue. Finite element method (FEM) simulations of mechanical interaction between neural probes and brain tissue were conducted previously [44, 58, 59].

Setup

The stress inside the brain tissue around deployed needles is caused by (undesired) movement between the two. In order to isolate the effect of employing flexible springs and needles, three shank geometries (Figure 20) were compared: a traditional square shaped shank (referred to as "shank"), a shank with needle extensions with springs (referred to as "spring") and a shank needles but without springs (referred to as "needle"). A cube of brain tissue with dimensions 500x500x500 μm^3 (500x500x700 μm^3 in case of "spring") is surrounding the silicon probe geometries. The probe geometries consist of a 400 μm long, 14 μm thick and 140 μm wide silicon shank. The "needle" geometry has 5 μm-wide, 14 μm-thick and 100 μm-long needles attached. The "spring" geometry has a spring with120 μm travel inserted between the needles and shank. COMSOL Multiphysics 4.4., (COMSOL, Inc., MA, USA) was used as simulator.

a) "shank"   b) "needle"   c) "spring"
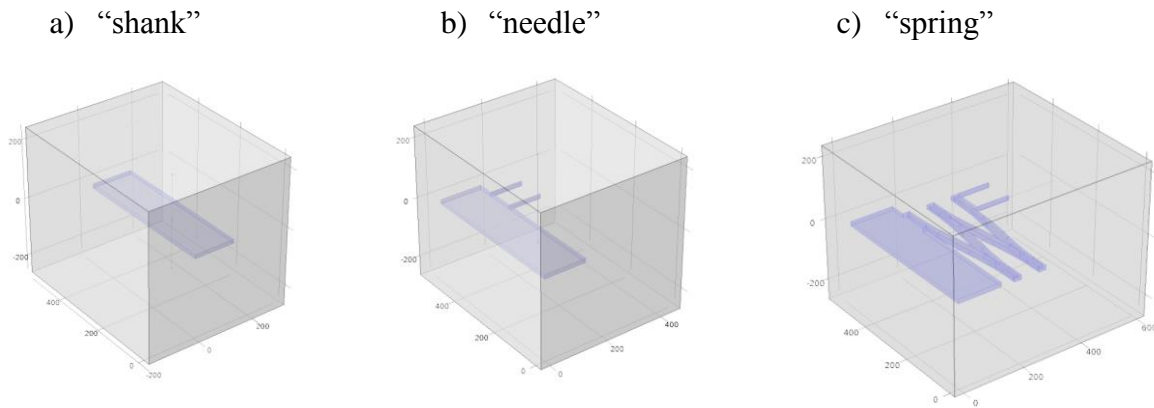
Figure 20: Simulated probe geometries surrounded by cube-shaped brain tissue. a) Geometry referred to as "shank" design, modelling a typical neural probe shank b) "needle" design, modelling needles attached to a shank c) "spring" design, modelling needles connected to a shank by springs as used in this thesis.

The mechanical boundary conditions were defined as follows (Figure 21): The tissue is assumed to be firmly connected to the springs (no slip). This is presumably more accurate once dense scar tissue built up around the implant than soon after insertion or while the electrodes deploy. To induce movement, one side of the brain tissue block is displaced by 5 µm towards the silicon shank. This distance is arbitrarily chosen, extracted values are meant to be interpreted in relation to each other. Two scenarios were simulated: The tissue is displaced along a trajectory parallel to the width of the shank (referred to as "side", Figure 21a). In the other case, the tissue is displaced along the thickness of the shank (referred to as "front", Figure 21b). The long side (case of "side") or the short side (case of "front") of the silicon shank is fixed and does not move.
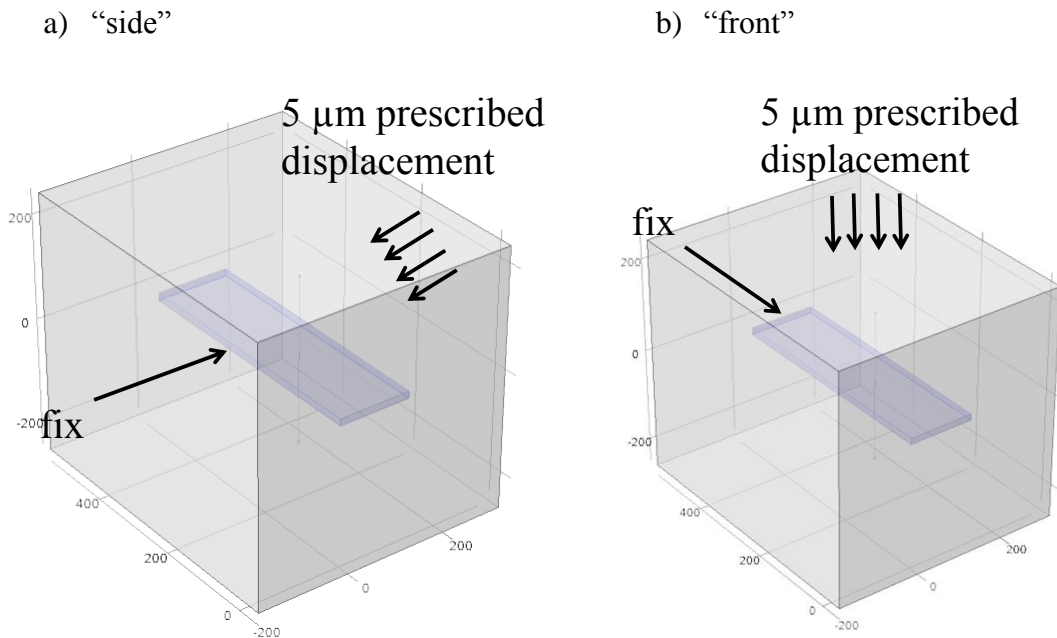
Figure 21: Boundary conditions of the simulation. Two scenarios were simulated for all designs. The scenario in a) shows the brain tissue displacing along a trajectory parallel to the width of the probe (referred to as "side"). Here the long side of the probe shank is immobilized. The scenario in b) shows the brain tissue displacing along a trajectory parallel to the thickness of the probe (referred to as "front"). Here the short side of the probe shank is fixed.

The material properties were defines as follow: If the brain tissue is white matter and undergoing slow compressions (on the order of 0.5 mm/s), it can be modeled to have a uniform, isotropic Young's modulus of 12,500 kPa and a Poisson ratio of 0.49 [60]. Frequency dependent effects (damping, inertia) are not considered, only the steady state solution is extracted. Silicon is modeled to have an averaged isotropic Young's modulus of 159 GPa and an averaged Poisson's ratio of 0.23 [48].

Results

Figure 22 shows the results for the "shank" geometry, for tissue-displacement in both "side" (Figure 22a) and "front" (Figure 22b) direction. Figure 23 shows these results for the "needle" geometry, Figure 24 shows these results for the "spring" geometry. Figure 25 shows the displacement of the springs. The stresses and displacements are color-coded. The relative relation between magnitude and color is shown above the tables. An absolute value of the color red is listed above each plot.

Figure 26 shows a graph of the magnitude of the stress along a path (Figure 26a for tissue-displacement in "side" direction, Figure 26b for tissue-displacement in "front" direction). In Figure 26a, the shank-tissue interface is located at x=0. In Figure 26b, the shank extends from x=-7 to 7. The tissue was displaced towards positive x-values.

a) "side", red-800 N/m²   b) "front", red-800 N/m²
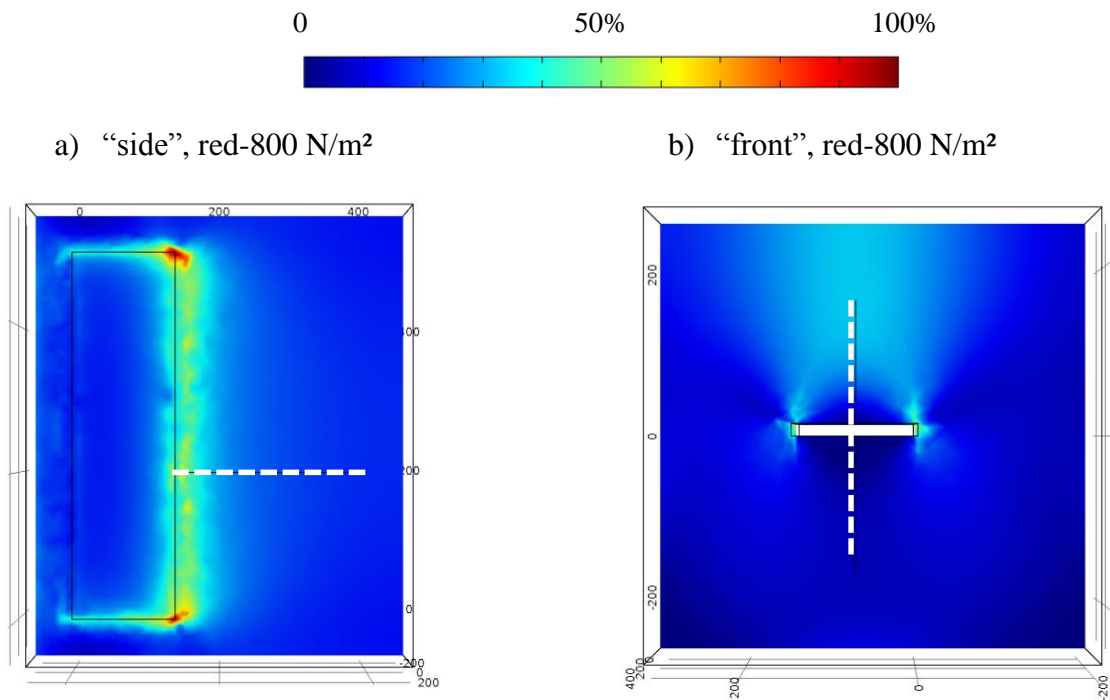
Figure 22: Simulated stress inside tissue around the "shank" geometry. a) results for tissue-displacement in "side" direction and b) results for tissue-displacement in "front" direction. The stresses are color-coded. The relative relation between magnitude and color is shown on top of the figure, and an absolute value of the color red is listed above each plot.
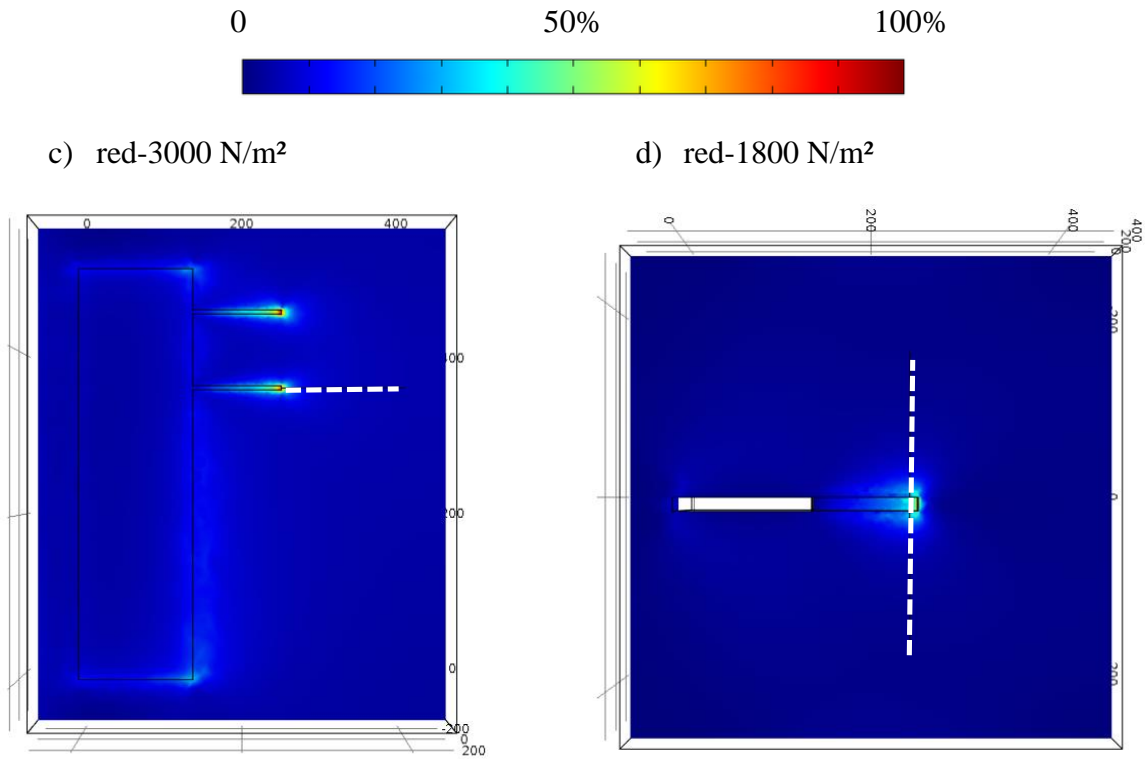
Figure 23: Simulated stress inside tissue around the "needle" geometry. a) results for tissue-displacement in "side" direction and b) results for tissue-displacement in "front" direction. The stresses are color-coded. The relative relation between magnitude and color is shown on top of the figure, and an absolute value of the color red is listed above each plot.
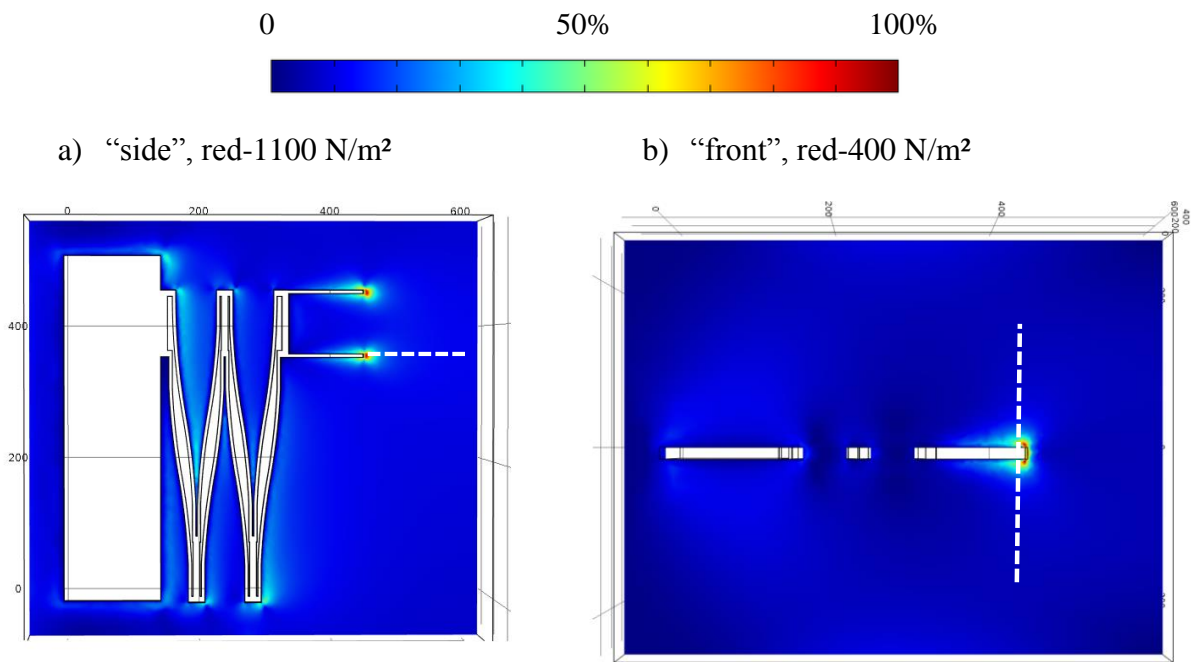
Figure 24: Simulated stress inside tissue around the "spring" geometry. a) results for tissue-displacement in "side" direction and b) results for tissue-displacement in "front" direction. The stresses are color-coded. The relative relation between magnitude and color is shown on top of the figure, and an absolute value of the color red is listed above each plot.
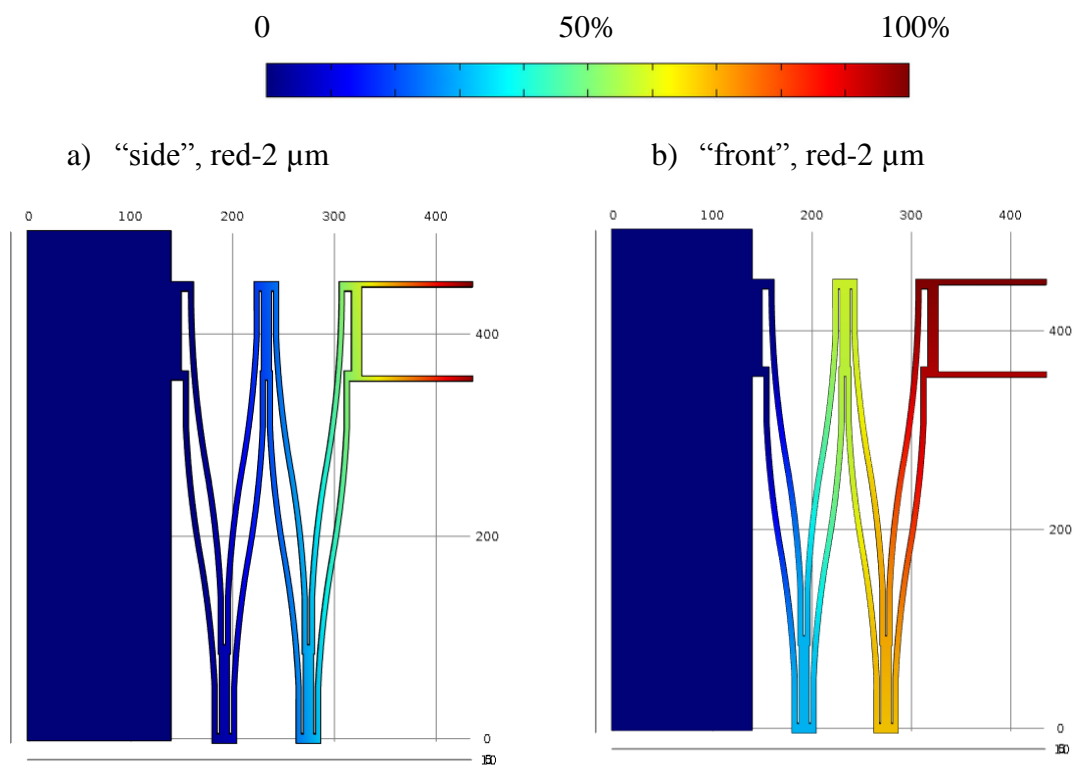
Figure 25: Simulated displacement of the "spring" geometry. a) results for tissue-displacement in "side" direction and b) results for tissue-displacement in "front" direction. The displacements are color-coded. The relative relation between magnitude and color is shown on top of the figure, and an absolute value of the color red is listed above each plot.

a) "side"
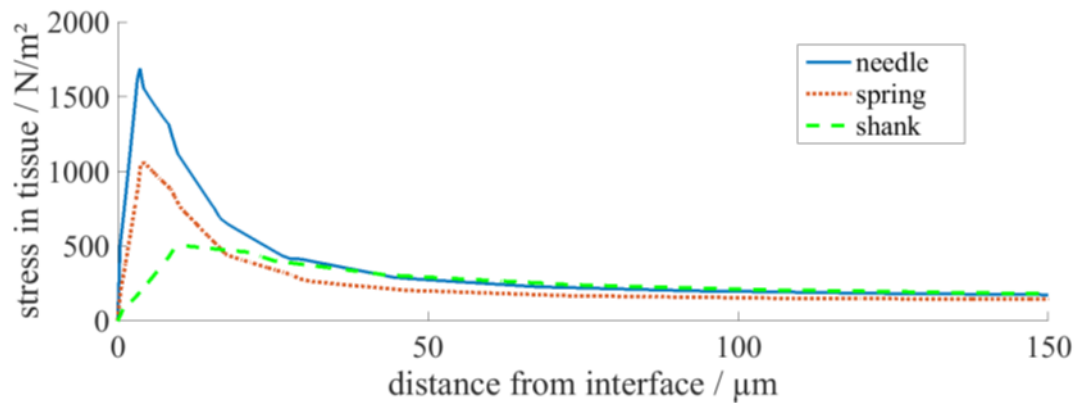
b) "front"
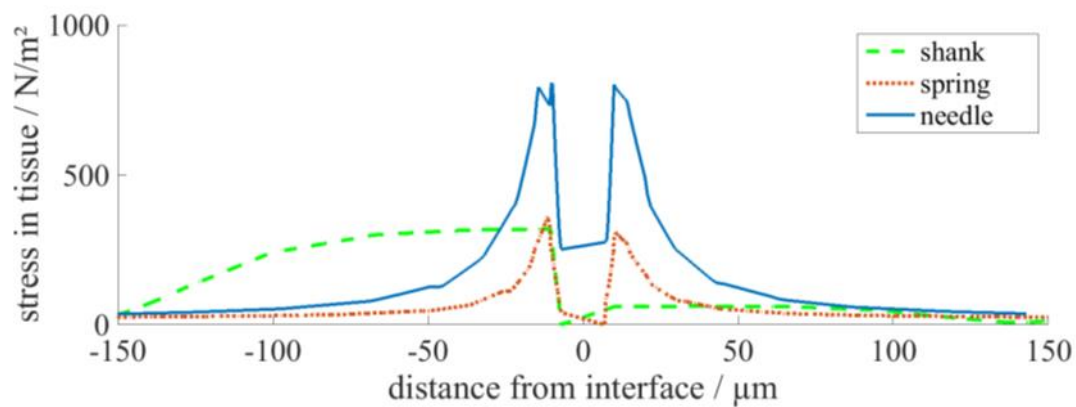
Figure 26: This graph shows the magnitude of the stress along a path - a) for tissue-displacement in "side" direction, and b) for tissue-displacement in "front" direction). In a), the shank-tissue interface is located at x=0, in b), the shank extends from x=-7 to 7. The tissue was displaced towards positive x-values.

Discussion

The resulting simulated stress inside the tissue around the shank and needle geometries can be lumped into a near (<30 µm) and a far (>30 µm) zone. The near zone is containing a large portion of neurons that are recorded from. In the near zone, the stress around needles is about a factor 4

51

higher than that around the shank. This illustrates how smaller structures, that are somewhat fixed in position, potentially cause higher stress inside tissue in response to relative displacement. The reduced stress around larger structures might be a reason that allowed relatively large microwire electrodes with 50 μm diameter to record with a high SNR stably over 80 days [23]. Even if less scar tissue is accumulated around smaller implants, they still might cause more damage to the fine neural structures due to the higher stress they induce. The stress in the tissue in the far-zone of all geometries is very similar. The simulation furthermore shows that the springs are flexible enough to partially compensate for the displacement in the tissue around them: The tip of the needles (location of deployed electrodes) that are attached by springs moves about 2 μm in response to 5 μm tissue displacement. The stress induced in tissue in the near-zone is reduced by 1/3 to 1/2 compared to that around needles without springs. In the far zone, the stress drops slightly below that around the other two geometries.

2.7   Fabrication

The silicon probes were fabricated using the well-established Michigan probes process, described by [61]. In short (Figure 27): the thickness of the probe shanks, needles and springs is defined by the depth of an etch-stop formed by boron doping of silicon. The outline of the shanks is defined by deep reactive ion etching. The electrical interconnects between electrodes and contact pads consist of 6000 Å thick phosphorous-doped polysilicon, insulated by a stress compensated 3000/1500/3000 Å thick silicon oxide/nitride/oxide stack. The electrode metals consist of 200/700 Å thick sputtered Ti/Pt.

a) *Boron doping of the surface of a silicon wafer*

b) *LPCVD polysilicon between two stacks of silicon oxide and silicon nitride. Sputter metals to form electrodes and contact pads.*

c) *DRIE to pattern silicon*

d) *Release in EDP*

Legend:
- Boron doped silicon
- O/N/O
- Polysilicon
- Metal

Figure 27: Fabrication of silicon neural probes using the dissolved wafer process developed at the University of Michigan.

Most fabricated probes have a uniform thickness of around 15 μm. Some probes were fabricated to have reduced thickness in the needles. Figure 28 shows a SEM close-up on needles with reduced thickness. The transition between thick and thin silicon has a smooth slope. This can also be used to sharpen the tip of the probe shank, or to create smooth edges along the shank to reduce stress induced into the tissue.
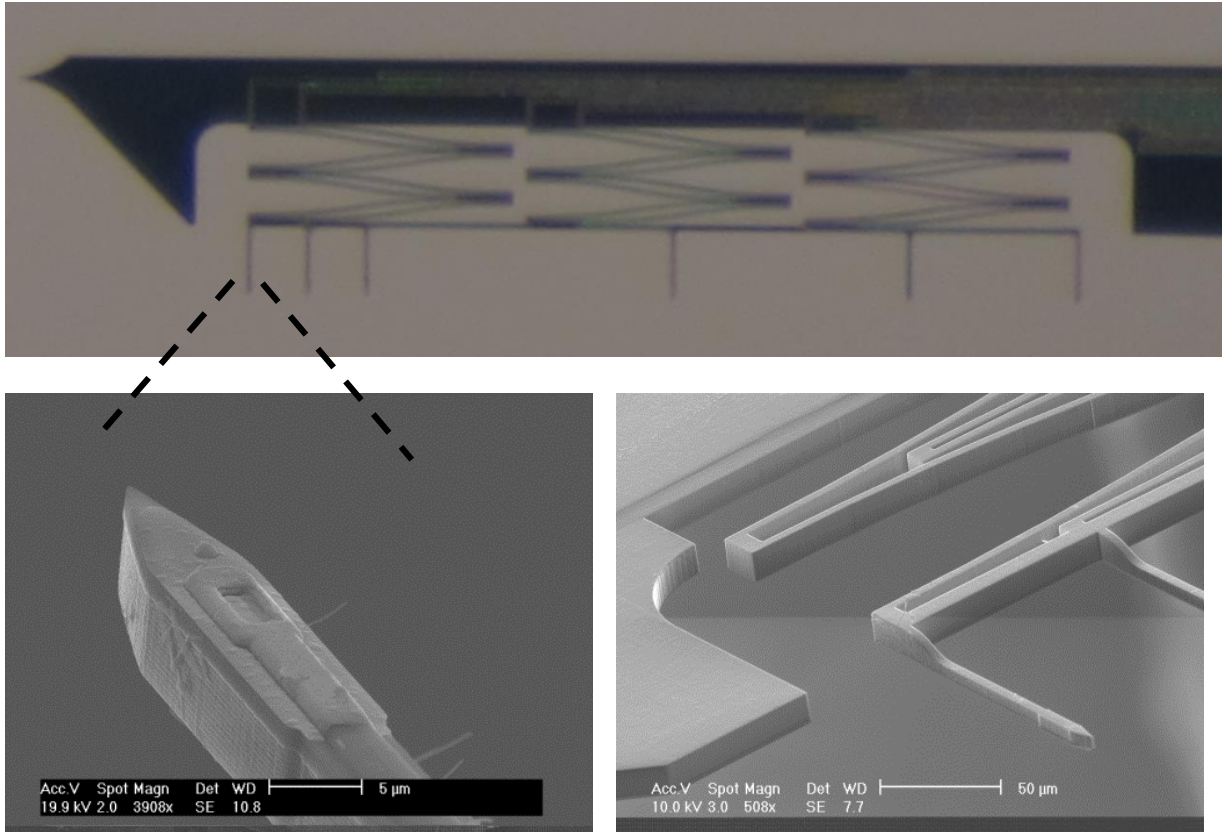
Figure 28: Micrograph of a fabricated probe shank with two SEM close-ups on the springs, needles and the electrodes at the end of the tips.

Previously, neural probes were fabricated such that they separate from the wafer during wet etching in ethylenediamine pyrochatechol (EDP). A design modification used in this work leaves all neural probes attached to a frame by small pins (Figure 29). This protects the delicate needles and springs, facilitates handling, and allows for post-release wafer-level. To release individual probes, the pins can easily be broken.
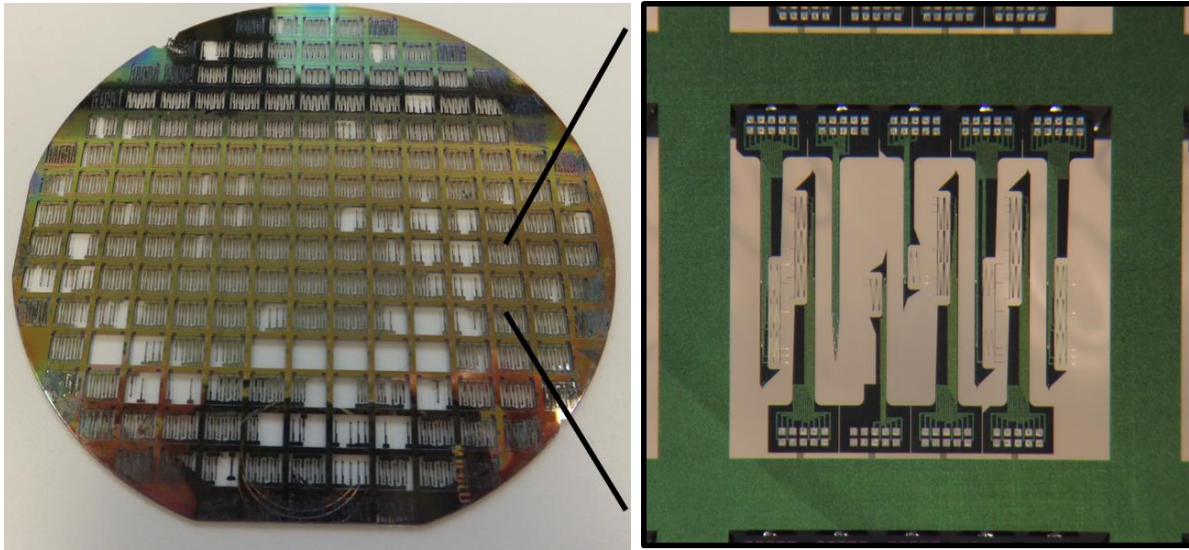
Figure 29: Neural probes connected by a frame, fabricated on a 4" wafer.

2.8 Insertion and deployment experiments

This section describes experiments that evaluate how the springs on neural probes can be retracted by starch hydrogel, and how far and fast the springs deploy after insertion. It is important that the electrodes deploy far enough to reach outside the sheath of scar tissue. Furthermore, the deployment should leave sufficient delay for the shank to be fully inserted. Since most brain tissues are non-transparent, the electrodes cannot be directly observed after insertion. Hence a brain model consisting of transparent agar gel was used. Neural probe shanks were inserted into this brain model and observed through a camera with attached zoom lens.

Methods

The springs were first retracted in air using a micromanipulator. This allowed observing the shape of the retracted spring.

A transparent brain phantom was prepared from agar gel. According to [62], 0.6 % agar gelled in water resembles several mechanical and rheological properties of brain tissue. The agar brain phantom was prepared by heating 1.2 g powdered agar in 200 ml de-ionized water to 90 °C. To minimize precipitation, the solution was cooled quickly. This was done by boiling agar gel in 2x concentration and once done, thinning it with cooled water to the appropriate concentration. The heated solution was then poured into a glass container with planar walls for observation. The gelled agar was covered with a thin film of water to prevent drying of the surface. For the experiments, the gel was heated to 37.5 °C on a hotplate, controlled with temperature feedback. For observation, a camera with zoom lens, connected to a computer with a USB video adapter for recording was used.

Two neural probe designs with integrated springs with different dimension were investigated. They were called "Assembly 1" and "Assembly 2". Their properties are listed in Table 5. "Assembly 1" is an iterated design, altered for better performance.

Table 5: Characteristics of compared assemblies

	Springs	**Starch coating**
Assembly 1	160 μm travel	Starch iodized in Povidone iodine (for better compatibility) and coated with PLGA (to delay deploying)
Assembly 2	120 μm travel	Starch iodized in Lugol's solution

The starch hydrogel was prepared by boiling starch granules in water. It was then manually dispensed on the springs using a syringe with a fine needle, under a microscope. The starch gel

was then dipped into Povidone iodine to iodize it. Finally, the starch gel was coated with PLGA by first dissolving PLGA in acetone (1 g/20 ml, stir for 24 hrs) and then dip-coating the starch-coated springs with it. Before that, the starch-coated springs were allowed to dehydrate for 24 hours. This process is described in more detail in section 3.3 .

Both probe assemblies were inserted into agar gel using a manually controlled z-stage at approximately 1 mm/s.

Results

The image in Figure 30 shows a part of a spring in air that was retracted using a micromanipulator.
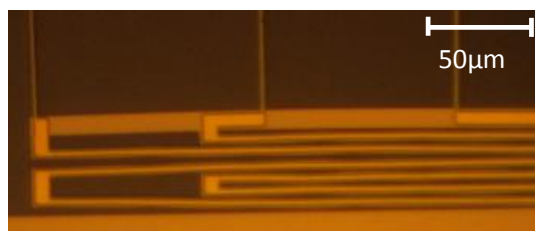
Figure 30: Silicon springs fully retracted by an external manipulator.

Figure 31 shows neural probes from "Assembly 2" before and after coating with starch hydrogel. Relatively small, free standing structures like the needles and the tip of the probe did not retain much starch. The middle section of the shank and the springs retained most of it. The needles retracted by almost their full travel of 120 µm or 160 µm, but a small gap (around 5 µm) remained between adjacent surfaces.
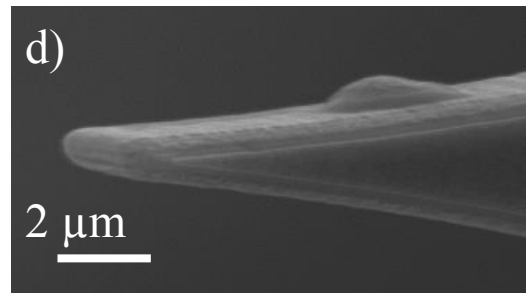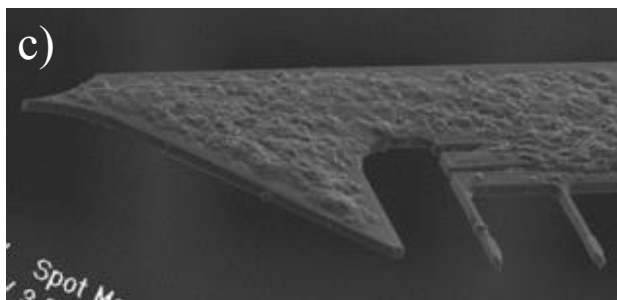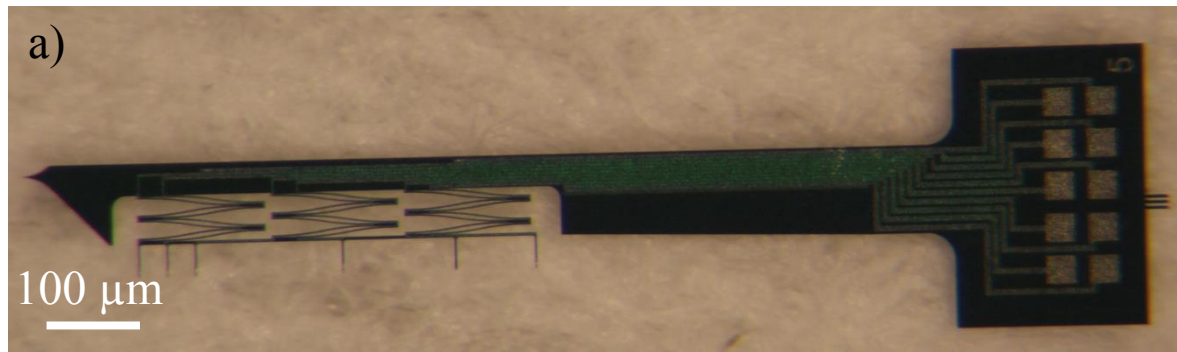
Figure 31: Retracting springs on neural probes from "Assembly 2". a) micrograph of a probe before coating with starch b) after coating with starch, iodizing and dehydrating. c) SEM image of springs, needles and tip and d) close-up on the tip.

Figure 32 and Figure 34a show "Assembly 1" inserted into agar gel and monitored for two hours and thirty minutes. Figure 33 and Figure 34b show this data for "Assembly 2".

In air
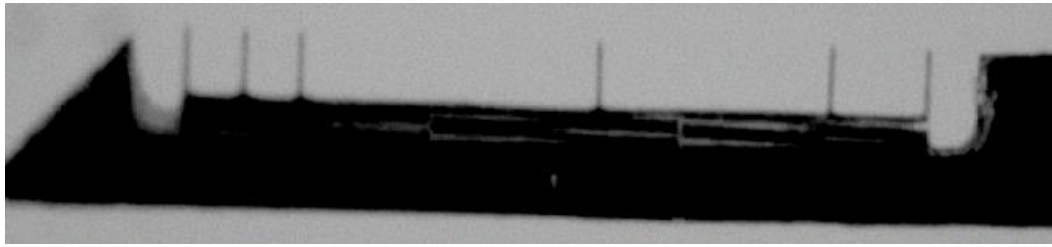
In agar at 37°C
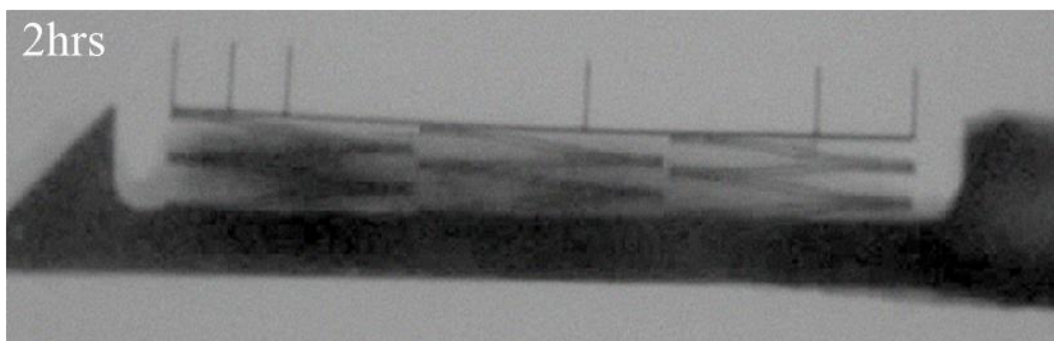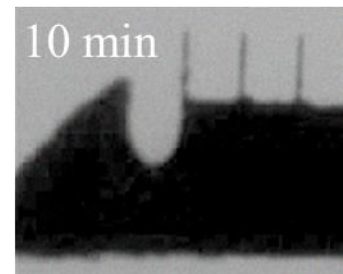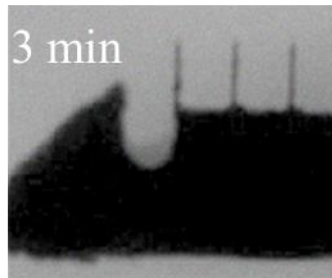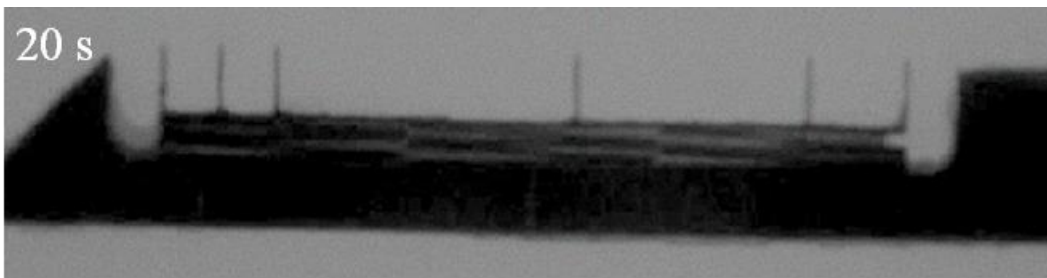
Figure 32: Images showing a neural probe from "assembly 1" deploying in agar gel. The time stamps correspond to the amount of time passed since insertion.

In agar at 37°C
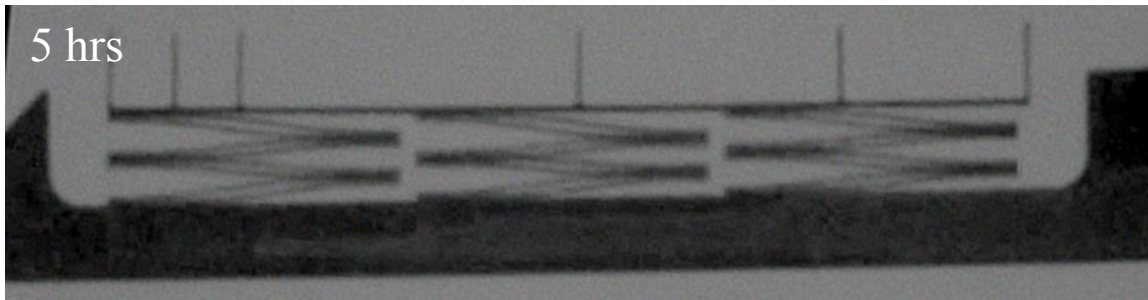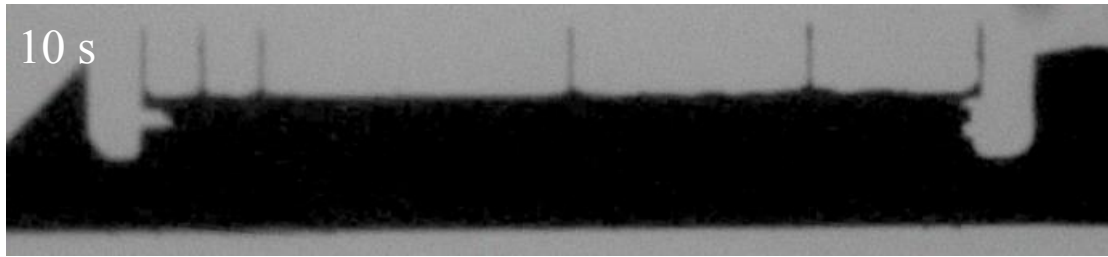
Figure 33: Images showing a neural probe from "assembly 2" deploying in agar gel. The time stamps correspond to the amount of time passed since insertion. The starch gel was iodinzed in Lugol's iodine, no PLGA coating was employed.

a)
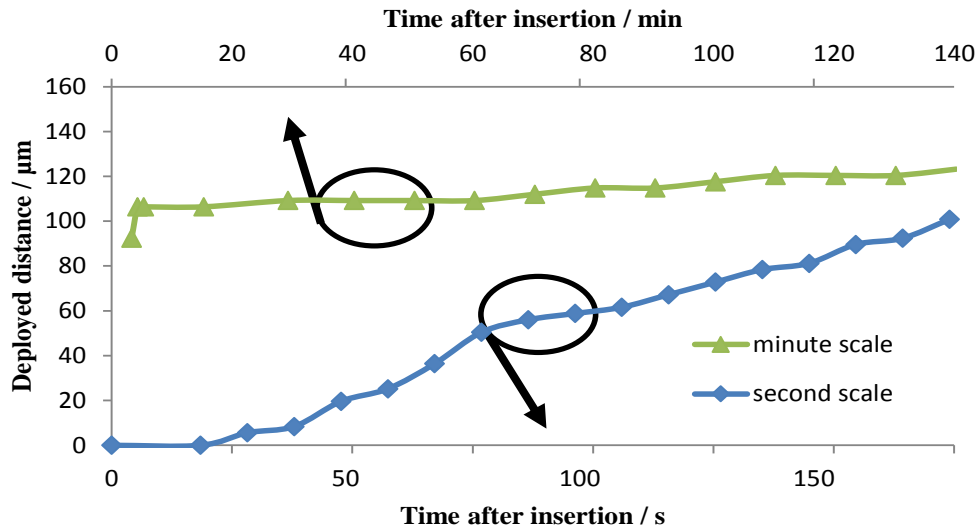
b)
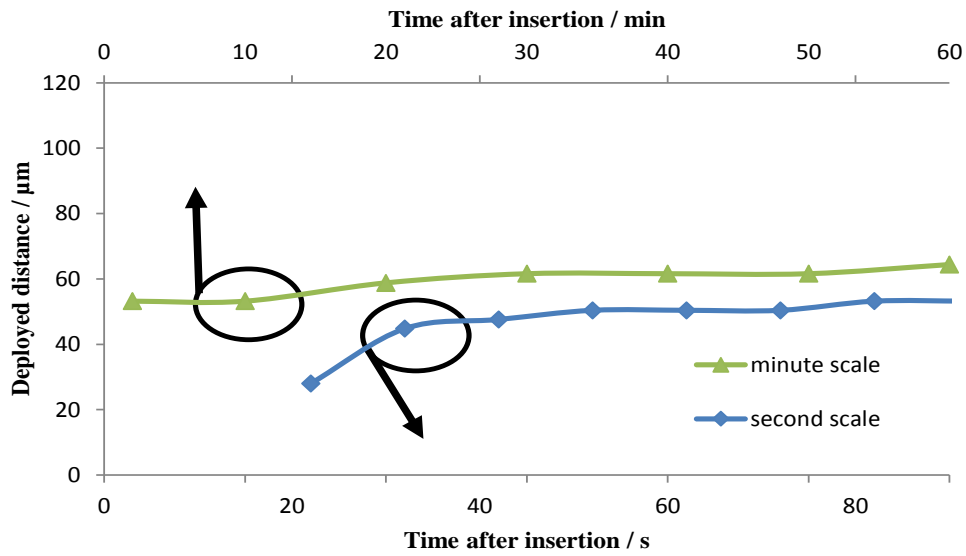
Figure 34: Measured distance of springs deployed in agar vs. time after insertion. a) "Assembly 1" and b) "Assembly 2".

Coating and Retracting

The springs could be retracted completely and without cracking by micromanipulators. In that state, they contributed little width to the shank.

The starch gel distributed between the springs and on top of the shank surfaces. It did not, or just minimally, cover the tip of the shank or the needles with electrodes. This has the advantage that the tips of the shank and needles remain sharp, and that the electrodes are not covered in thick starch gel.

The dehydrating starch-gel retracted the springs sufficiently for the needles to be shielded by the tip of the shank during insertion.

Deploying

The needles on either assembly did not bend considerably during insertion or during deploying. Most likely, due to their short length, they would rather slice through the agar gel than bend. During insertion, the needles are only subjected to forces that would make the bend in case they are not completely covered by the tip of the shank.

In case of "Assembly 1", the electrodes deployed by roughly 120 µm over the course of two hours. The deployment can be divided into three parts: For the first 20 s they deploy less than a few microns, within the first three minutes they deploy linearly by roughly 100 µm (0.5 µm/s) and for the following two hours they deploy additional 20 µm (0.17 µm/min).

In case of "Assembly 2", two shortcomings were observed: as shown in Figure 33a, the springs deployed with an initial jump, on the order of several tens of microns, as soon as they came into

contact with the agar gel. Furthermore, as shown in Figure 33b, the electrodes did not deploy by more than 70 µm. This is likely not enough to position them outside the sheath of scar tissue formed around the shank.

The starch/PLGA combination experiments suggest that these shanks can be inserted for about 20 s before the needles move by more than a few microns, leaving the protected position close to the shank. For a 2 mm long shank, this would allow for a minimum insertion speed of 100 µm/s which is within the range of common practices. Pure starch (no PLGA coating), even when it was iodized, deployed with an initial jump almost coincidental with coming into contact with water.

In the designs investigated, all deploying needles were connected to a bar that is connected to all springs. One concern with deploying these needles is, that this should happen evenly. No one side should deploy faster than the other. A straight deployment trajectory should be maintained. The results indicate that this happened in the experiments. Early experiments showed, though, that when starch was applied unevenly, some needles would deploy delayed or not at all. Applying starch using a syringe, as it is described here, allowed for fine control over the amount of starch distributed. Furthermore, starch-coated springs can be deployed multiple times. The behavior of the springs that are deployed multiple times did not change severely (given that they were re-iodized after each time). This provides for a reliable way to ensure even release of the springs (by doing a test run, and adding starch if necessary).

2.9   Electrode design considerations and impedance tests

Adding the capability to deploy electrodes off the shank of neural probes poses restrictions on the size, number, density and distribution of the deployed electrodes compared to those fabricated directly on the shank. It furthermore needed to be investigated if the coating of the probes with

starch and PLGA is detrimental to the electrode performance. This section discusses design considerations of electrode size and number, and electrical impedance testing of the deploying electrodes.

One design concern was if it is possible to form useful electrodes at the end of the micrometer-small needles. It was shown previously that it is possible to form electrodes with dimensions on the order of several micrometers, capable of single-unit recording: The authors of [63] simulated recording performance of electrodes in neural tissue. According to their results, the area of electrodes does not impact the signal-to-noise ratio (SNR) much- rather the electrode-tissue impedance matters. Their smallest investigated geometric area was 177 μm^2 and it recorded with the highest SNR (even though larger electrodes performed only slightly worse). The majority of the noise picked up from electrodes originates from neural background activity, but the electrode interface also contributes some noise. The lower the impedance, the lower the noise amplitude [64]. The electrode impedance scales with the electrode surface area which can be increased without increasing their geometric area by roughening their surface, for example by depositing conducting polymers [65].

The required count, density and spatial distribution of electrodes depends on the application. Electrodes are capable of recording from single neurons within a 140 µm radius [66] (depending on the type of neuron and orientation of the electrode). Increasing the pitch between electrodes beyond that (such that the same neurons are recorded by multiple electrodes) facilitates or allows spike-sorting [67] (assigning individual neurons to recorded spike forms). This can be done, for example using a tetrode configuration [24]. When recording from the neocortex, it can be of interest to distribute electrodes to record from brain layers (planes parallel/lines perpendicular to

the brain surface in gyri/sulci) or brain (lines perpendicular/ planes parallel to the brain surface in gyri/sulci).

The number of deployed electrodes is limited by electrical routing. Electrical interconnects from the electrodes to the shank need to be routed across the springs or across separate flexible traces (Figure 35 a) and b)). The springs were designed to be shallow and do not fit multiple traces side-by side (although moderately simple process modifications are possible that would allow stacking several traces on top of each other). Leaving out stacking interconnects, an inherent trade-off would set the number of electrodes to be less or equal to the number of springs. With current spring designs, the length of two nested springs (projected on the length of the shank) is 450 μm. According to that, for every 450 μm of shank length there can be two electrodes connected. The electrodes can be arranged freely along the length of the shank, with one electrode per needle (meaning that the electrodes can be distributed freely along the length of the shank with the exception for multiple electrodes in the same plane perpendicular to the shank length). The pitch between needles and the length of needles can be arbitrary chosen.

a)

b)   c)

Needles

Springs

Shank

Electrodes

Insulator
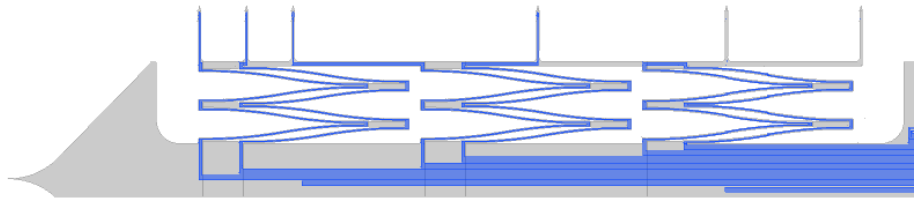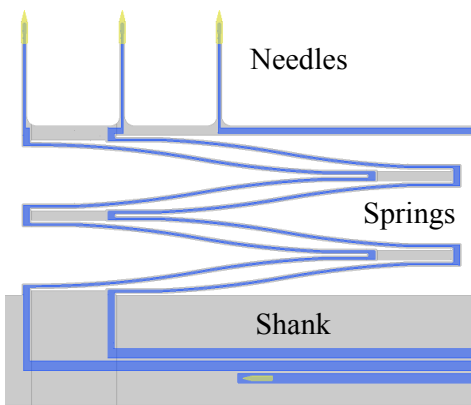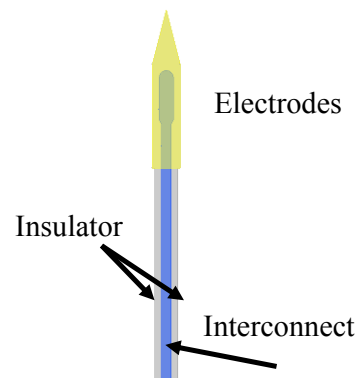
Interconnect

Figure 35: Drawings of interconnect routing and electrode distribution - a) a shank with six springs can connect six electrodes that are arbitrarily distributed along the length of the shank connecting to the springs - b) A single set of springs with interconnects routed on top of them - c) a single needle with one electrode.

The impedance of an electrode can be lowered without increasing its geometric surface area by coating it with a conductive material, forming a rough surface [68]. A lower electrode impedance can lower the noise, and the detrimental effect of parasitic impedances. One of the materials used to do that is PEDOT (poly(3,4-ethylenedioxythiophene)) [69]. PEDOT is a polymer that can be doped to become electrically conductive. In case of this project, PEDOT was doped with para-

toluensulfonate (pTS). This is indicated as PEDOT:pTS. PEDOT associated with pTS was shown to have superior adhesion to substrates [65].

Methods

The electrodes on the shank have an area of 130 μm^2, and the electrodes at the end of needles have an area of 177 μm^2.

The electrodes were coated with PEDOT:pTS as follows: a solution of 0.01 M 3,4-ethylenedioxythiophene (483028, Sigma-Aldrich, St. Louis, MO) and 0.1 M sodium p-toluenesulfonate (152536, Sigma-Aldrich, St. Louis, MO) was electrodeposited on them by applying 100 pA/electrode for 600 seconds. This forms a layer of poly(3,4-ethylenedioxythiophene):sodium p-toluensulfonate (PEDOT:pTS).

The impedance of the electrodes was measured with a PGSTAT12 Autolab (EcoChemie, Utrecht, Netherlands), controlled by a vendor-supplied NOVA software. The electrodes were submerged in an isotonic phosphate buffered saline (PBS) solution (BP3994, Fisher, Waltham, MA). A stainless steel rod was used as the counter electrode, and an Ag|AgCl electrode (RE-5B, BASi, West Lafayette, IN) was used as the reference electrode. The impedance measurements were performed by applying 10 mV$_{RMS}$ swept from 10 Hz to 31 kHz. A custom Matlab (Mathworks, Natick, MA) script was used to analyze and plot the output data. The impedance of the electrodes was measured as fabricated, after plating with PEDOT:pTS, after coating with starch, iodizing, and adding PLGA. To investigate the effect of starch and PLGA on electrodes, with and without PEDOT, both versions were tested separately.

Results

Figure 36 and Figure 37 show the impedance of electrodes without PEDOT:pTS plating. Figure 38 and Figure 39 show the impedance of electrodes plated with PEDOT:pTS. Electrodes at the end of needles and those directly on the shank are listed separately. The magnitude and phase was averaged over 4 electrodes. Spectrum plots and non-averaged impedances can be found in the appendix (Figure 85 - Figure 92).
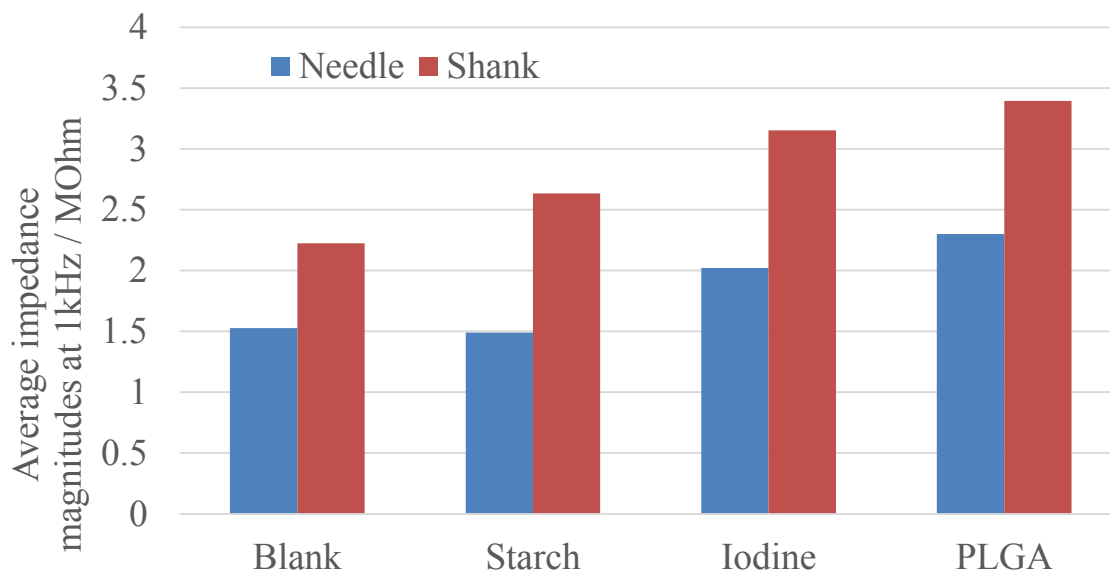
Figure 36: Average electrode impedance magnitudes at 1 kHz without PEDOT:pTS
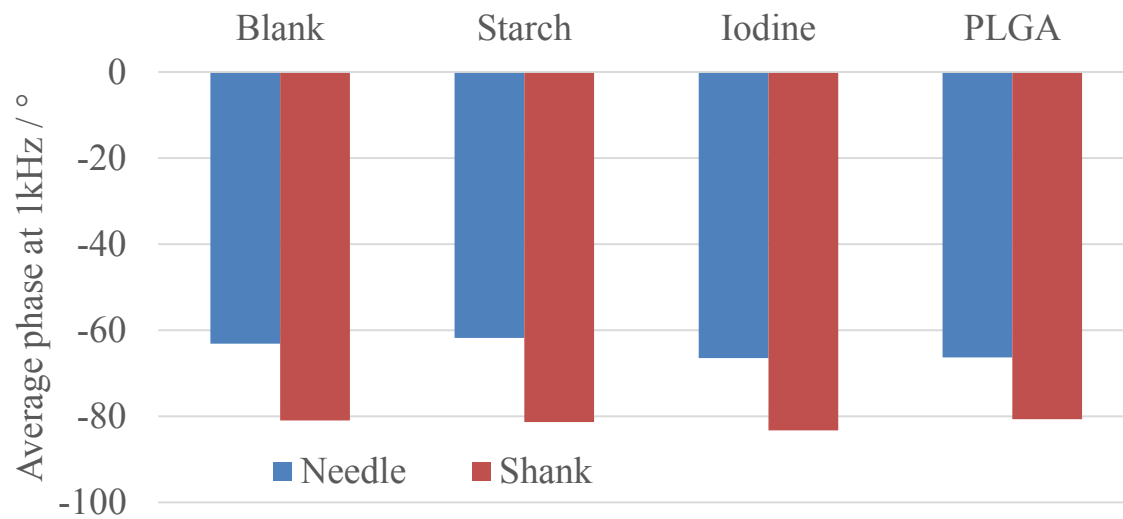
Figure 37: Average electrode impedance phases at 1 kHz without PEDOT:pTS
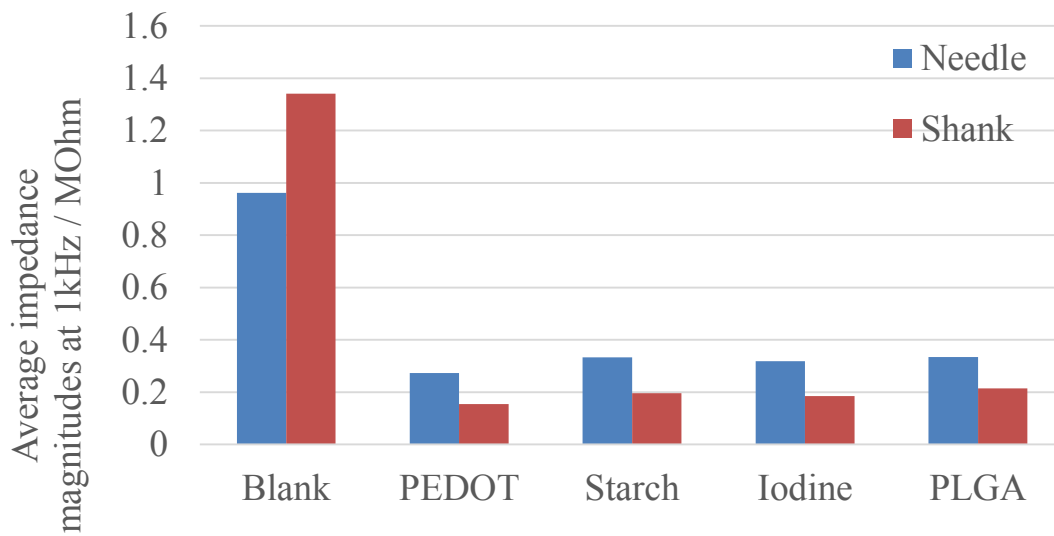
Figure 38: Average electrode impedance magnitudes at 1 kHz with PEDOT:pTS
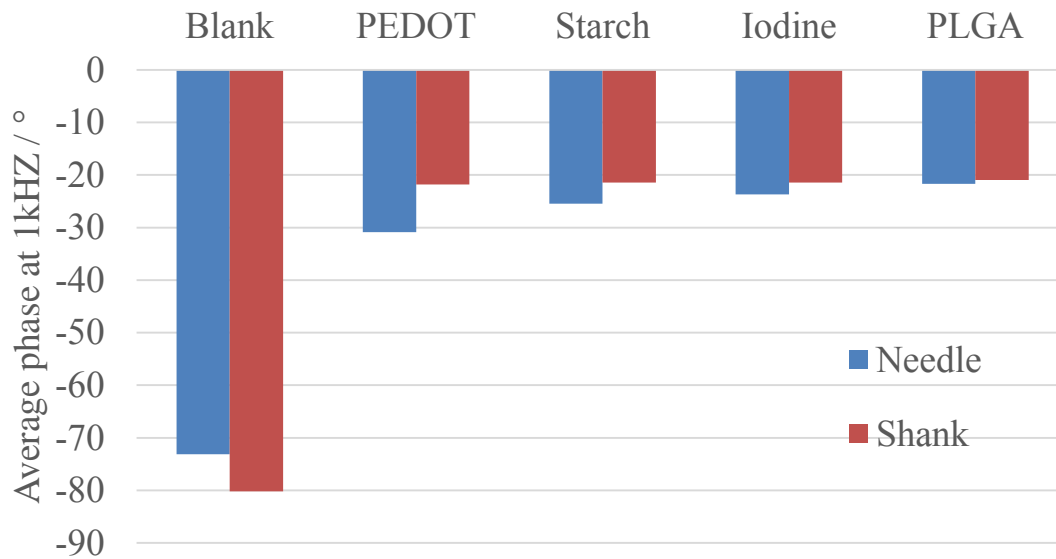
Figure 39: Average electrode impedance phases at 1 kHz with PEDOT:pTS

Discussion

The impedances of electrodes on the shank were initially higher than those at the end of needles. This is likely because their area is smaller by design (130 μm² vs. 177 μm²). As fabricated, the electrode impedance was around 1.5-2 MOhms. For many recording setups this is too high and hence PEDOT:pTS was deposited. This lowered the impedance values to well acceptable values. After depositing PEDOT:pTS, the electrodes on the needles had slightly higher impedances than those on the shank (300 kOhm vs. 180 kOhm). There are two possible reasons for that: The electrodes on needles (unlike those on the shank) are connected by shallow polysilicon traces across springs and needles. When the electrode impedance is lowered sufficiently, the resistance of these traces becomes considerable. Furthermore, during electroplating PEDOT:pTS, all electrodes were connected in parallel. Since the electrodes on the shank are smaller, the deposited PEDOT:pTS will likely have different electrical properties on either electrode design.

The measurements indicate that PEDOT:pTS lowers the electrode impedance from 1-1.4 MOhm to below 300 kΩ. This should be sufficiently low for high quality recordings. Neither coating with starch, povidone iodine nor PLGA increased the impedance of electrodes coated with PEDOT:pTS much (valid for electrodes on the needles and on the shank).

The impedance of electrodes on the shank that are not plated with PEDOT:pTS did increase considerably after coating with starch. The reasons for this different behavior are unknown. PEDOT:pTS might be porous and only its surface might accumulates fragments of starch gel. Since, in that case, a large area of the PEDOT below the surface is still exposed to water, the impedance would not suffer much.

2.10   Piezoresistive gauges to estimate deployed distance

Once the probes are implanted into brain tissue, it will be important to determine if and how far the springs deploy. Since brain tissue is nontransparent in most cases, this is not straightforward. One way to do this is to integrate a sensor that measures the deployed distance. To realize such a sensor, the polysilicon leads on some springs were distributed in a way to increase the change in their electrical resistance as the springs deflect (Figure 40). This was done by shifting the traces to positions closer to the outside of the spring –increasing the stress magnitude, and routing the traces on sides of the springs building up either all compressive or all tensile stress under deflection. The piezoresistive tracks on springs are meant to provide a means of indicating the position of the springs after insertion.

a)
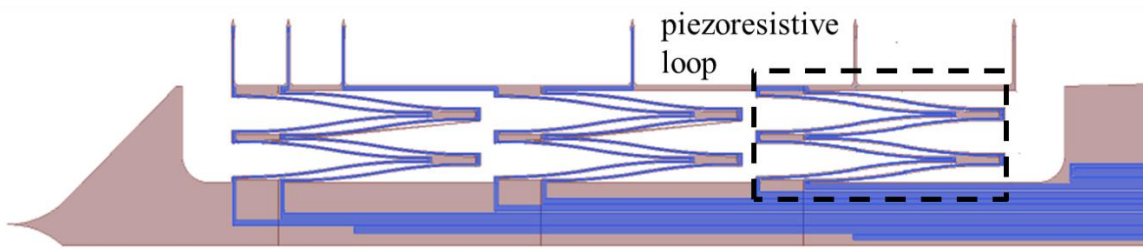
b)
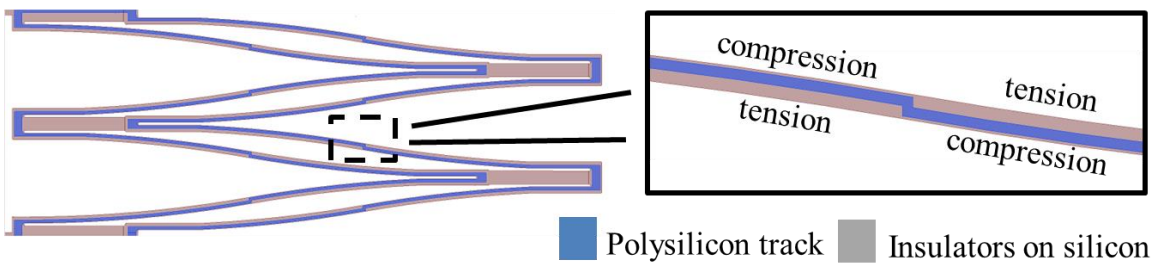
Figure 40: Polysilicon (blue) on silicon springs (gray) routed to form piezoresistors serving as sensors for the distance the springs deployed. a) full set of springs, b) spring with piezoresistive polysilicon routed to compress as springs retract.

Design and analysis

The resistance of the polysilicon route was calculated using a similar model as was used for the spring deflection in section 2.3 . The model is also based on the Euler-Bernoulli beam theory, derived from [47]. The mechanical stress, $\sigma(x)$, in an element of the polysilicon track is, to first order, proportional to the curvature of the deformation of the spring $\rho(x)$, and to the distance z between the center of the track and the neutral axis of the spring (equation (9) and Figure 41a and b):

$$\sigma(x) = \frac{z \times E}{\rho(x)} \approx z \times E \times y''(x) \qquad\qquad (9)$$

The electrical resistance, $\rho_{el}(x)$ of an element of piezoresistive material is linked to the stress by the piezo coefficient π:

$$\rho_{el}(x) = \rho 0_{el} \times (1 + \pi \times \sigma(x)) \qquad\qquad (10)$$

The electrical resistance of the whole track is derived by integration over its length L:

$$R_{spring} = \int_0^L \rho_{el}(x)\,dx/A \qquad\qquad (11)$$

with E–the Young's modulus of polysilicon. Solving equation (11) yielded Figure 41c.

a)

average height of interconnect

z

neutral plane

b)

1μm

2 μm

0.5 μm

c)
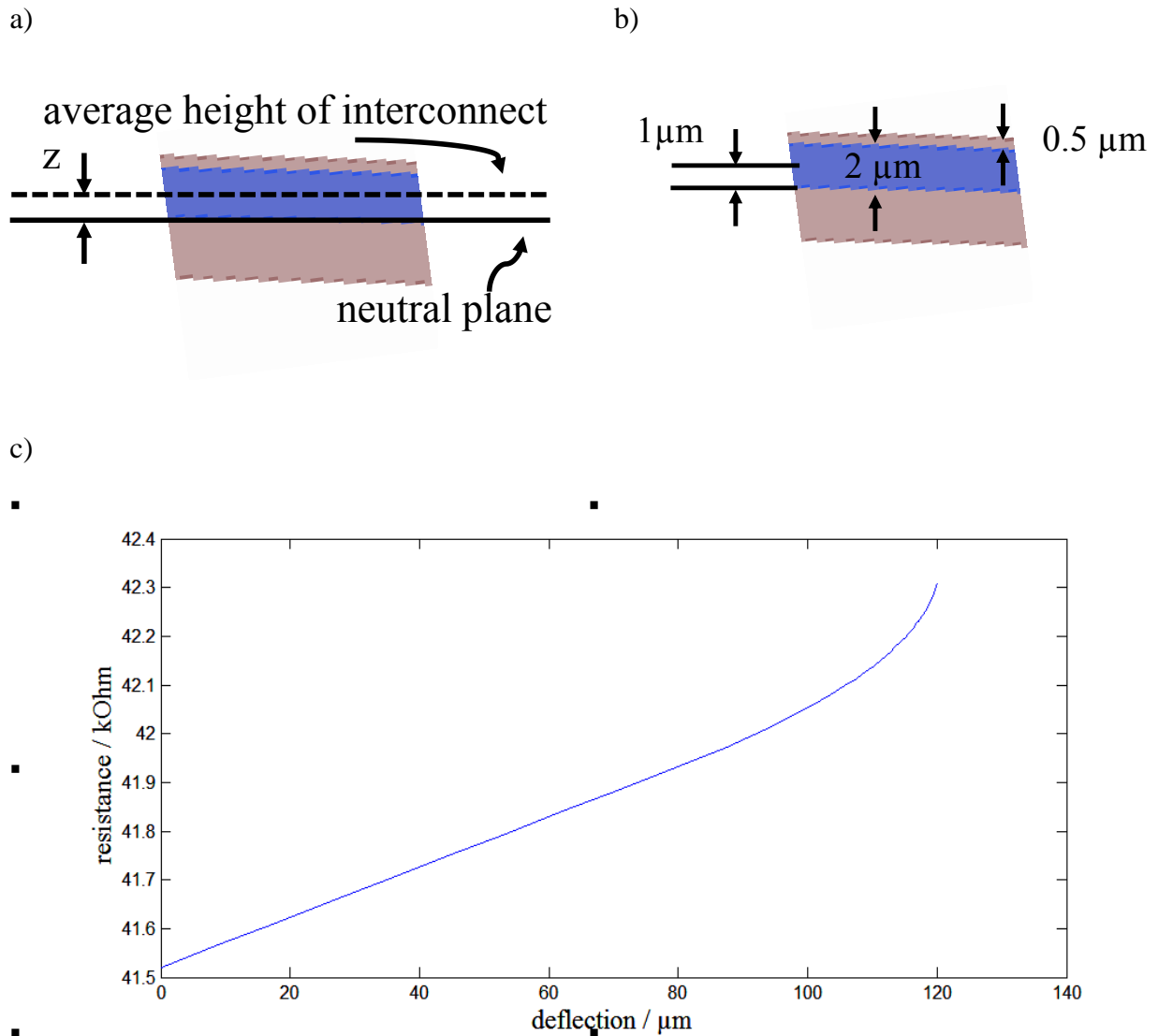
Figure 41: Piezoresistor dimensions and results from analytical modeling of characteristics.

a) illustration of the meaning of "z" as the average height of interconnects above the neutral plane. b) dimensions of interconnect width and spring width. c) Analytically derived plot of spring interconnect resistance vs. spring deflection (for springs with 120 μm travel).

When the springs are implanted, their temperature will change from room temperature to body temperature. In mammals, this can be more than 16 °C. The resistance of the polysilicon track does

not only change with stress but also with temperature. A first-order approximation of the amount of the change is:

$$\rho_{el}(x) = \rho 0_{el} \times (1 + \alpha \times \Delta T)$$
(12)

With α, the temperature coefficient of resistance and ΔT the temperature change. For phosphorous doped polysilicon, α is between -1000 and -2000 ppm/K [70]. For a temperature change of 16 °C, this results in a resistance change of -1.6 % (assuming -1500 ppm/K). This would lower the resistance of a polysilicon loop with 41.52 kOhm resistance at room temperature by 664 Ohm. This change is similar to that caused by 80 µm deflection (although opposite in sign, for the example chosen). Hence compensation for temperature induced resistance changes is necessary. For that, a dummy polysilicon interconnect, R_d, is looped on the shank where it is not exposed to the mechanical stress caused by spring deflection. The spring and shank interconnects are connected in a voltage divider configuration. The output voltage of the sensor is read out at the point of their connection (Figure 42). Since this voltage is proportional to the ratio of both resistances, their temperature induced resistance changes cancel, and only the stress modulates the output voltage (equations (13) and (14)).

$$V_{out} = V_{dc} \times \frac{R_d \times (1 + \alpha \times \Delta T)}{R_d \times (1 + \alpha \times \Delta T) + R_{spring}(\sigma(x)) \times (1 + \alpha \times \Delta T)}$$
(13)

$$= V_{dc} \times \frac{R_d}{R_d + R_{spring}(\sigma(x))}$$
(14)
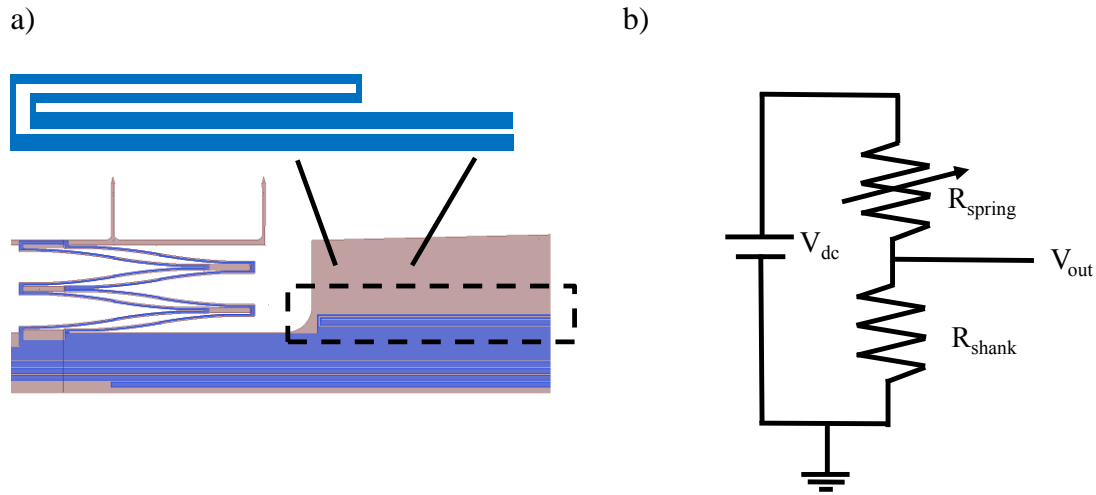
Figure 42: Temperature compensation for piezo-resistive spring. A dummy loop out of polysilicon is formed on the shank and used in a voltage-divider configuration, cancelling-in first order, the effects of the temperature coefficient of resistance on the output voltage.

Methods

To get some insight into their functioning, the piezo gauges were calibrated in air. This was done by moving the springs with a micromanipulator, while 2 V dc were applied. The output voltage was recorded at defined positions. This was done on four probes named P1-P4.

In another experiment, the piezo gauges were tested how they perform under more realistic conditions. For that, a section of lamb cadaver brain is heated to 37 °C in a temperature-controlled saline water bath. A neural probe shank with springs, one of which has a piezoresistive track routed on top, is coated with iodized starch and inserted. Figure 43 shows the setup used to measure the deployment of springs through cadaver lamb brain.
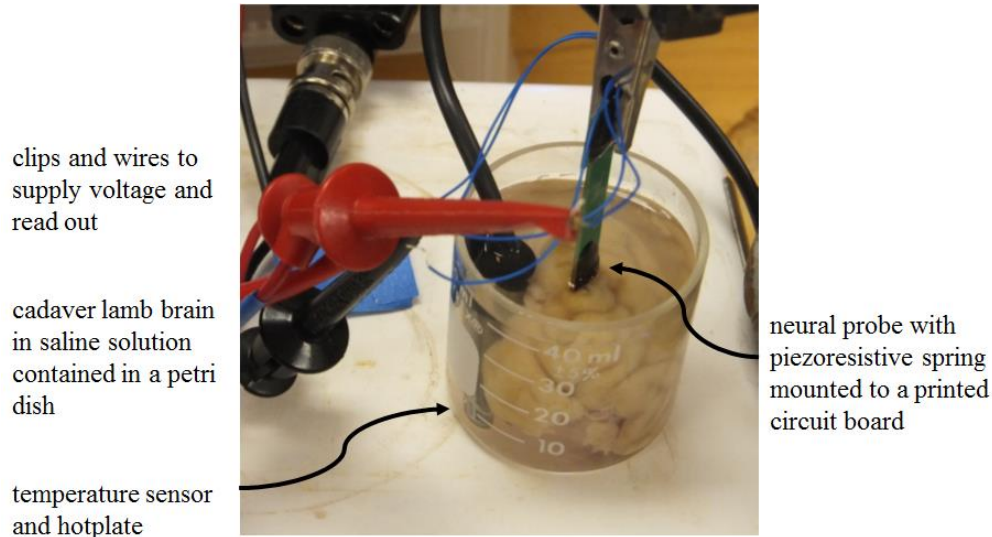
Figure 43: Neural probes with piezo-resistive springs inserted into a cadaver lamb brain.

To read out the piezoresistive gauge, 1 V is applied across the piezoresistive track and the loop for temperature compensation. Although the sensitivity of the sensor is, according to equation (13), proportional to the applied voltage, only 1 V was chosen. A voltage low enough to not hydrolyze water at a fast rate is safer for use in biological applications. The output voltage of the voltage divider was recorded. The voltages were supplied and recorded using a Lab VIEW program controlling a NI-DAQ. The voltages were sampled at 1 kHz, and 1000 samples were averaged to produce one measurement.

Results

The fabricated springs with polysilicon tracks routed as piezoresistors are shown in Figure 44. The figure shows two examples of extreme alignments. About 30 % of the piezoresistors were properly aligned. Even though the samples that were misaligned by more than 0.5 μm did not have silicon dioxide/nitride protecting the polysilicon tracks during EDP etching (see paragraph 2.7), almost none of the tracks were etched and still formed coherent electrical connection.

silicon dioxide   polysilicon

5μm
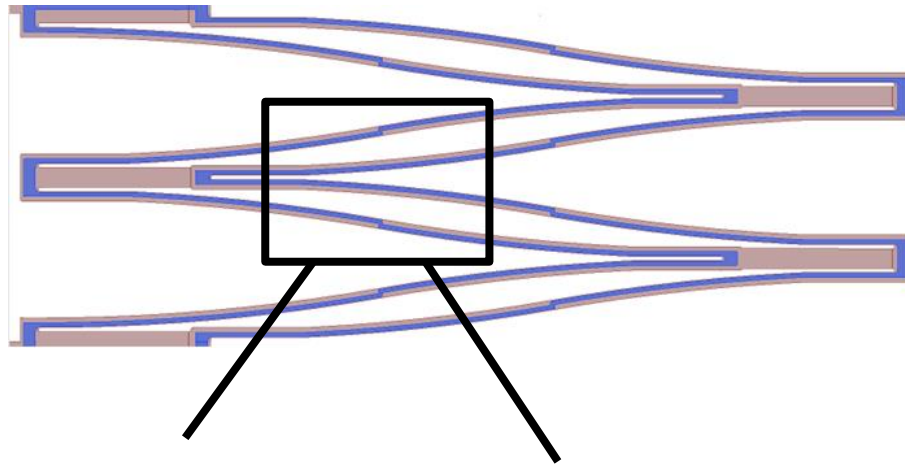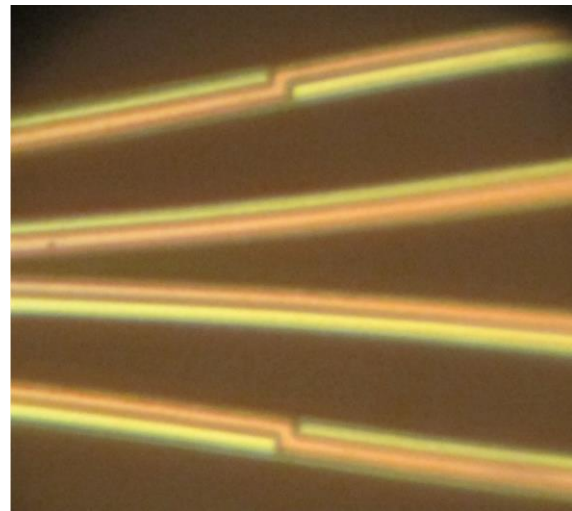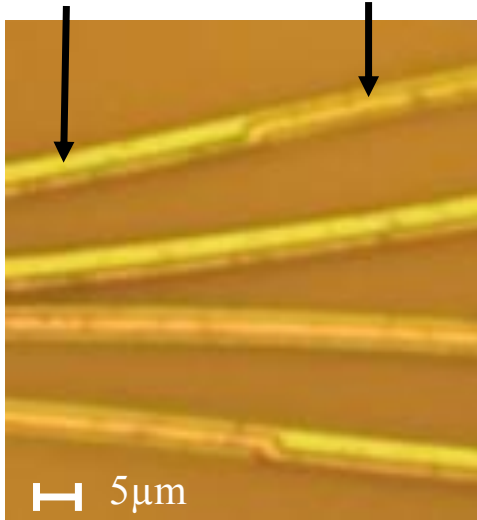
Figure 44: Piezoresistive interconnects on a spring with proper (a) and bad alignment (b).

The resistance of polysilicon looped through one set of springs was measured to be around 20 kΩ.

The resistance changes for full retraction of the springs were around 200 Ω.

The results of the calibration of the piezo-gauges are shown in Figure 45. Here springs of an earlier design with approximately 200 kΩ resistance were used. The calibration measurements show that the output voltage of the voltage divider changes by 0.6-1.2 mV.
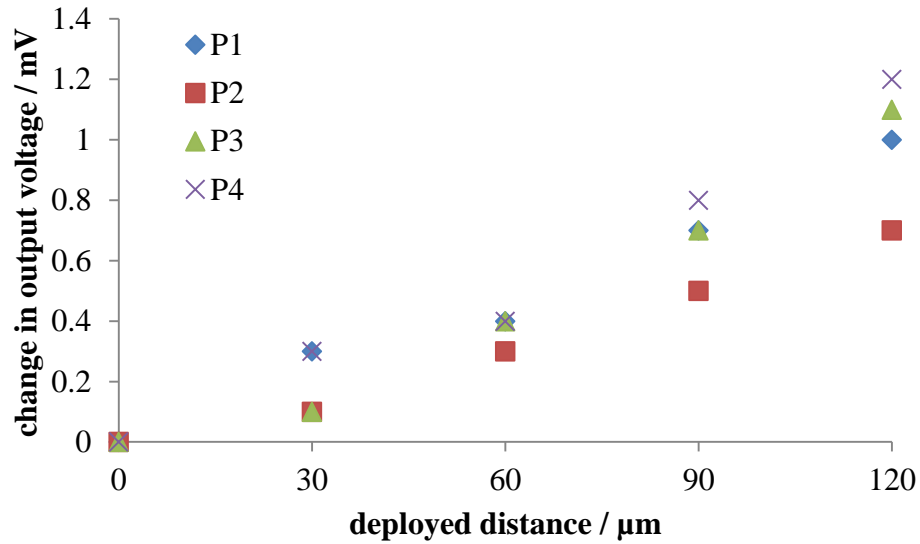
Figure 45: Calibration data of piezoresistive gauges. The change of the output voltage of the voltage divider while applying 1 V is plotted against the distance the springs are deflected.

The output voltages recorded over time of the piezoresistors inserted into the lamb cadaver brain are shown in Figure 46.
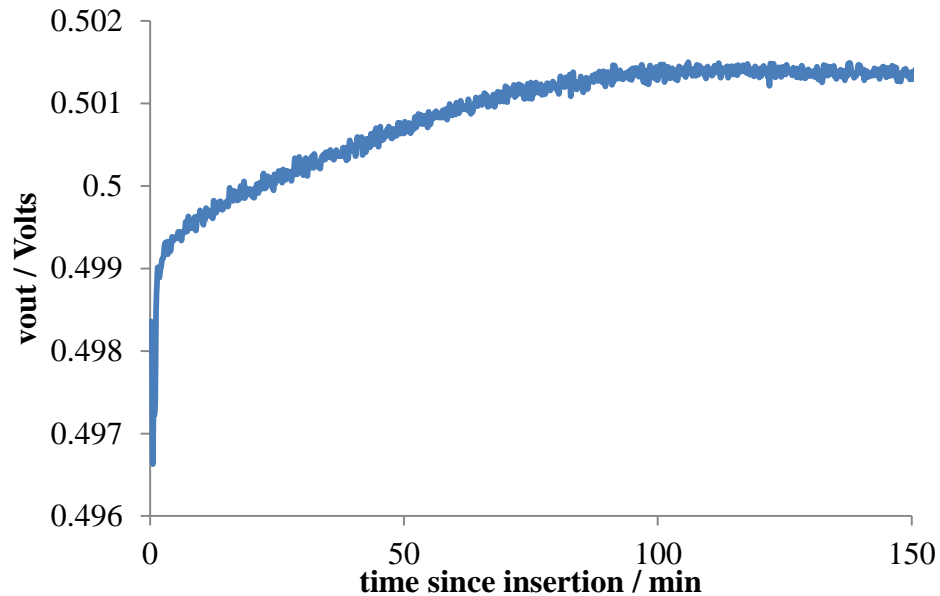
Figure 46: Output voltage of the voltage divider between piezo-gauge and temperature compensation resistor. The probe with both resistors was inserted into a lamb-cadaver brain soaked in saline water that was heated to 37 °C. For the read-out, 1 V was applied across both resistors.

Discussion

Although only about 30 % of the fabricated springs were aligned properly (the polysilicon did not protrude the edge of the spring), most of them did provide electrical functionality. This might have been due to passivation provided by Teflon deposited during DRIE etching for sidewall-passivation. The misaligned samples appeared to be useful for acute measurements. However, for chronic use, precise alignment is necessary since the side-wall passivation might not provide reliable protection against bodily fluids for long. Using more careful alignment or tools with

precise automated alignments like that provided in many steppers, a repeatable alignment within 200 nm should be achievable with reasonable cost.

The calibration data suggests a change in output voltage on the order of one milli-Volt for a full deflection of the spring. Compared to the noise-level at the given sample rate ($\approx$0.15 mV), this is a reasonable resolution. With averaging the noise level will reduce further.

The output voltage of the voltage divider in the *in-vitro* experiment shows three clear sections. Initially, there is a sharp increase in voltage visible. This might be caused by the jump in deployment, as observed in the deployment experiments described in paragraph 2.4 . The rapid change in temperature and immersion into water might also have contributed to this jump. After the jump, a slow and gradual voltage increase became apparent. This could be caused by the springs deploying though brain tissue. The deployment lasted around 90 min, which is somewhat longer than what was observed in experiments using agar-gel instead of brain tissue. This could be caused by different diffusion coefficients and mechanical resistance of agar gel and brain tissue. After 90 min of deployment, the output voltage settled and did not continue changing.
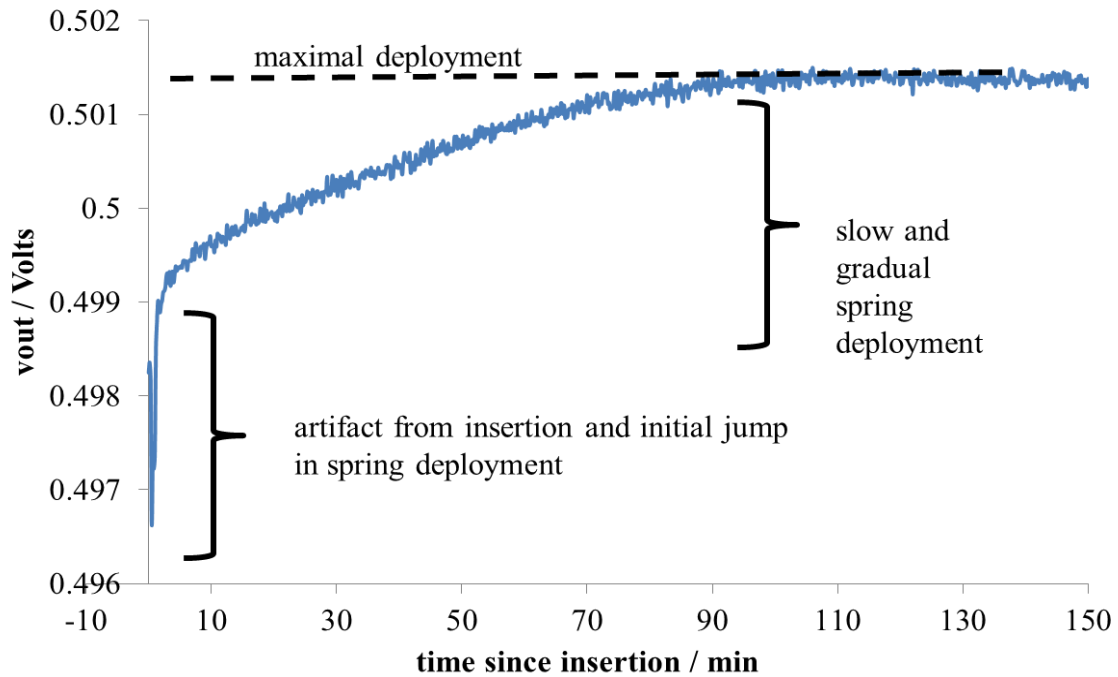
Figure 47: Time-course of the output voltage of the voltage divider and interpretations of the three sections.

One disadvantage of the piezoresistors in their current form is that they require two leads across the springs that could be used for electrodes. The electrode count is limited by space available for interconnects, since they need to be routed across the springs. This can be improved by connecting the two leads to one electrode, so only one electrode needs to be sacrificed. Alternatively, the resistors could be formed in a metal layer that is deposited over the springs. This would still allow for polysilicon tracks to be formed underneath.

2.11   Pilot *in-vivo* study of neural probes with deployable electrodes

This section reports on an *in-vivo* experiment investigating if the developed neural probes with deployable electrodes can be implanted into rat motor cortices (M1 left, M1 right, S1 right) without breaking and if they are capable of recording action potentials. This study was done in collaboration with Dr. Paras Patel.

<u>Methods</u>

Three neural probes were used in this experiment. All had integrated springs with 120 μm travel that were coated with starch that was iodized with Povidone iodine. These springs were not coated with PLGA since this was not available at the time of the experiment. The neural probes were glued to a printed circuit board. Electrical connections were wirebonded to immersion gold tracks on the PCB, and insulated using epoxy glue (353ND-T, EPO-TEK, Massachusetts, USA).

For these experiments, adult male Long Evans rats weighing 300 – 350 g were used. Anesthesia was initialized with 5% isoflurane (v/v). The rats were maintained under anesthesia with an intraperitoneal injection of ketamine (50 mg/mL) / xylazine (5 mg/mL). A dosage of 0.125 mL per 100 g of body weight was never exceeded. Regular intraperitoneal injections of ketamine (50 mg/mL) were given. The head was shaved at and around the area of the incision site. The shaved area was swabbed using alternating applications of betadine and 70% ethanol. Ointment was applied to the eyes to keep them from drying during surgery. Ear bars were mounted in both ears and fixed in a stereotax. After making an incision, the skin flaps were pulled apart using hemostats and the skull surface was cleaned using cotton swabs and 2% hydrogen peroxide (v/v). A burr bit (19008-07, Fine Science Tools, Foster City, CA) was used to drill a hole around the periphery of the skull for a bone screw (19010-00, Fine Science Tools, Foster City, CA). Next,

three 2 mm x 3 mm craniotomies were made over the right and left hemisphere's motor cortices, and over the right somatosensory cortex using coordinates from a reference atlas [60]. Reference and ground wires originating from the PCB were electrically shorted and attached to the bone screw. Recordings took place while the rats were under ketamine/xylazine anesthesia.

All acquisition of electrophysiology recordings were taken using a ZC16 headstage, RA16PA pre-amplifier and RX5 Pentusa base station (Tucker-Davis Technologies, Alachua, FL). During data acquisition the pre-amplifier high pass filtered at 2.2 Hz, anti-aliased filtered at 7.5 kHz, and sampled at a rate of ~25 kHz. Recordings at each surgical site were divided into blocks lasting 2 min. The neural probe depth was adjusted between multiple recording blocks on the same site. After band pass filtering between 250 and 5 kHz using a 4th order Butterworth filter, the recorded waveforms were inspected and plots extracted. The noise level was calculated by taking the root-mean-square voltage of the channel across a 16 s period not containing visible spikes, after filtering, and multiplying it with a factor of 3. This was done similarly in related work [16].

The implantation coordinates and depths (targeting large pyramidal cells in layer V and VI) were:

Site1: depth: 2mm, anterior : 2.5 mm, interaural: 11.5mm of bregma targeting M1, left

Site2: depth: 2.3mm, anterior 1.8mm, interaural 7.2mm of bregma, targeting S1, right

Site3: 3mm. anterior : 2.5 mm, interaural: 11.5mm of bregma targeting M2, right

These sites are illustrated in Figure 48.
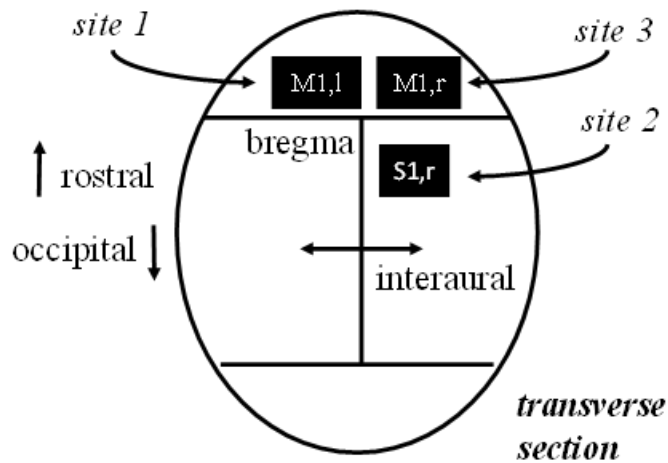
Figure 48: Map of sutures on the skull illustrating insertion sites. The left and right primary motor cortices and the primary right sensory cortex are targeted.

Results

Figure 49 shows a neural probe shank before, during and after implantation. During this experiment, the right S1 area was targeted. No shank buckling was observed during implantation. The shank was inserted with retracted needles. After the recording session, the shank was explanted. During explantation, the needles appeared fully deployed. Furthermore, all needles of the shank appeared to be intact after explantation (visual inspection).

Figure 50 shows exemplary transient waveforms of selected channels.
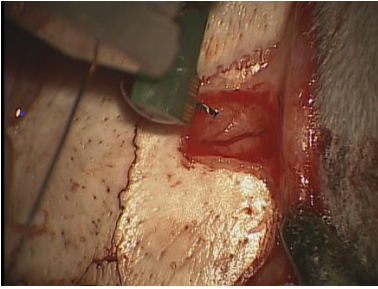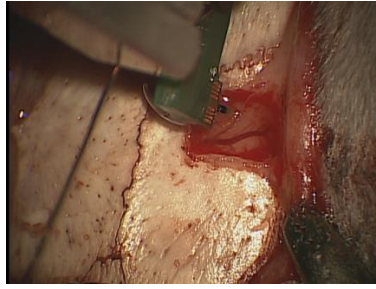
a)　　　　　　　　　　b)　　　　　　　　　　c)
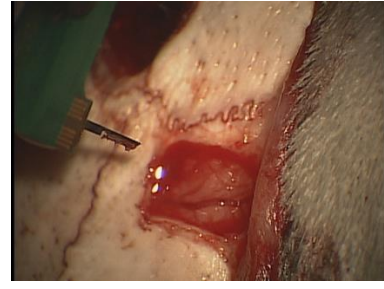
Figure 49: Images of probe insertion, indwelling and explantation. a) the right sensory cortex s1 is exposed b) the probe is inserted, no bleeding observed, c) after recording, the probe is explanted and still appears to be intact. A small amount of bleeding is observed.

Site 1, Electrode 2 Channel RMS (16 s): 2.3 µV →6.6 µV noise Signal amplitudes ≈ 40 and 90 µVpp	
Site 3, Electrode 1 Channel RMS (16 s): 7.9 µV → 23.7 µV noise Signal amplitudes ≈ 110 µVpp	
Site 1, Electrode 3 Channel RMS (16s): 5 µV → 15 µV noise Signal amplitudes ≈ 40 and 110 µVpp	
Location of electrodes on shank	
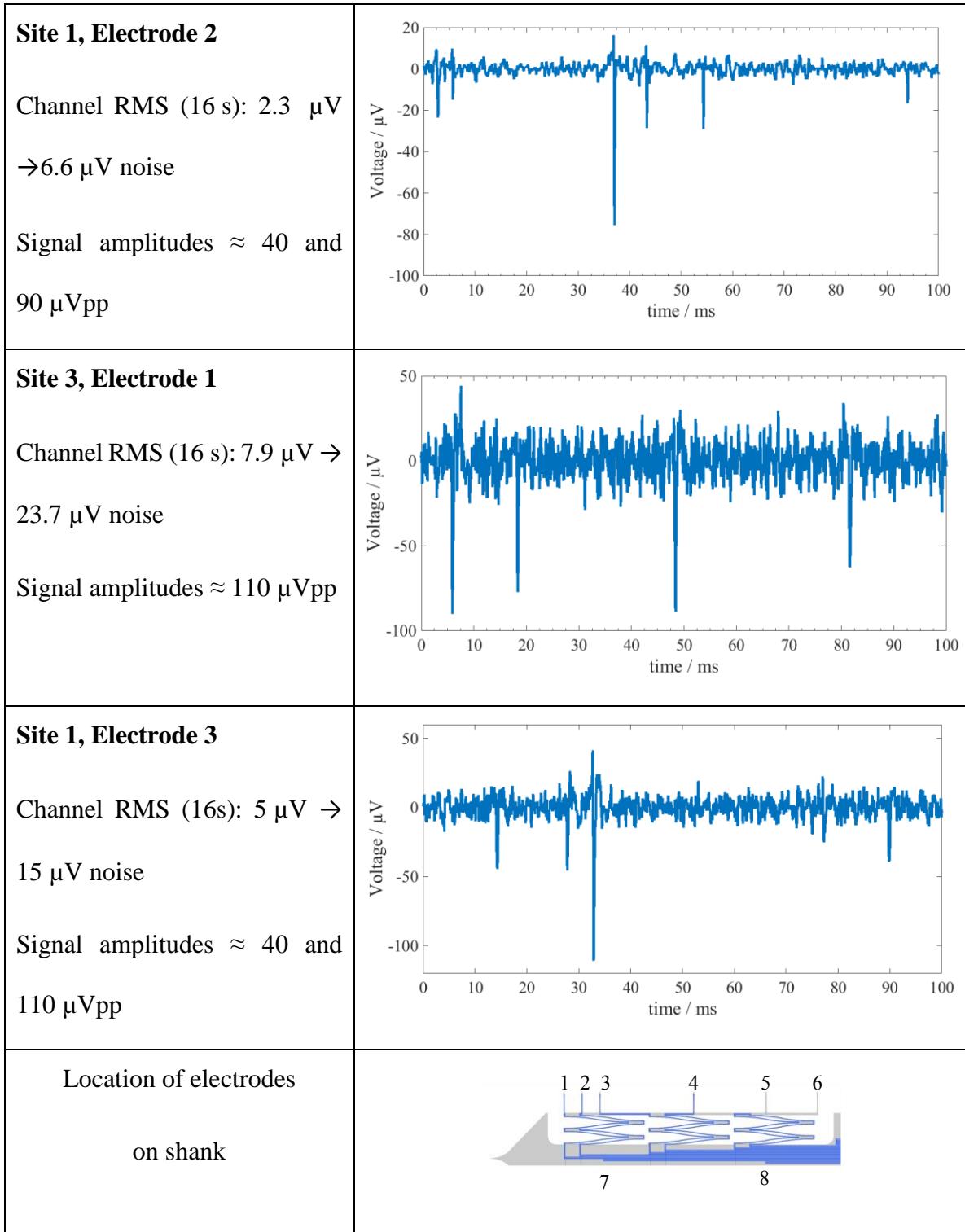
Figure 50: Exemplary waveforms and corresponding location of electrodes they were recorded from. Electrodes 1-3 recorded similar signals on all three implantation sites. The other electrodes did not record signals distinguishable from noise.

Discussion

The probes explanted with deployed electrodes after being inserted with retracted electrodes. This indicates that the electrodes did deploy. It furthermore indicates that, in this acute experiment, the probes can be explanted with deployed electrodes without the needles breaking. This means that the needles were strong and flexible enough to move through tissue perpendicular to their length. Allowing complete explantation without leaving debris behind can be a requirement for implants used in clinical applications.

The insertion did not cause excessive buckling of the shank, or dimpling of the brain. This was a concern since the shank is unusually wide. The insertion, furthermore, was performed with a typical, manually operated z-stage. It certainly is an advantage that these neural probes do not require extremely fast insertion.

The recorded neural signals indicate that the fabricated neural probes with deployable electrodes are capable of acutely recording action potentials. The starch gel, iodized with Povidone iodine, did not render the PEDOT:pTS-coated electrodes incapable of recording. Although not verified in this experiment, electrodes coated with PLGA had similar impedances and are assumed to perform similarly. The noise levels of the recordings shown are between 6.6 µV and 23.7 µV. This allowed the spikes, presumably originating from neural action potentials, to be clearly distinguished. The recorded signals came, in all cases, only from electrodes #1-3. These are the three upper deployed electrodes. There might be several circumstances causing that. The electrodes further back on the shank might not have picked up signals because they did not reach the large pyramidal neurons in layer IV and V of the motor cortex. Another reason might be tissue damage and hemorrhage caused by insertion of the relatively wide shanks.

2.12   General discussion

The main motivation of deploying electrodes away from the shank after implantation is to position them such that they become less susceptible to the immune response and insertion damage around the shank. The structures connecting to electrodes can be made extremely fine and flexible, as they are protected by the shank during insertion (and do not need to provide force for insertion). Hence the electrodes likely interface with healthier neurons. This does not compromise the mechanical stability of the shank. Disadvantages include the increased shank width compared to traditional neural probe designs and constraints on the number, position and local density of electrodes due to reduced space for routing.

To deploy the electrodes, an actuator was developed that is based on silicon springs that are retracted and released by a starch-based hydrogel. This constitutes a practical and easy-to-use mechanism. It does not require specialized equipment to be operated for implantation. It also does not increase the process complexity much (no extra steps/materials required for microfabrication, starch hydrogel is easy-to-use). Since the springs deploy until their reactive force balances the resistance of the tissue, and the hydrogel coating them is biodegradable, the deployed electrodes are floating almost freely inside tissue. A flexible connection between the probe shank and the skull was shown to reduce the tissue damage caused by relative motion between the brain and the skull [33]. Since in the case of spring-deployed electrodes the electrodes are tethered to the shank, micromotion of the shank might be more tolerable. Floating electrodes also might pick up less motion artifacts. There are some disadvantages of the developed autonomous one-time actuation. Once the electrodes deployed, repositioning the probe shank vertically becomes troublesome. Since in that state the needles slice tissue along their length, they will induce a larger amount of tissue damage (this also applies to removing the shank with deployed electrodes from the brain).

Also, this will bring the needles at risk of breaking. The concept considerably increases the width of the shank. This will induce a larger amount of tissue damage during insertion of the shank. A wider shank puts constraints on the formation of shank arrays in order to monitor a volume of tissue. This can be required for some applications, especially for brain-machine interfaces, due to the distribution of the neurons of interest. Furthermore, since the electrode interconnects are routed on top of the springs, the number, density and distribution of electrodes is limited. Stacking multiple interconnects on top of each other could alleviate this limitation.

The experiment on monitoring deploying needles through an agar brain model showed that the electrodes deployed by more than 100 µm. This is, according to studies investigating the geometry of the immune response, sufficient to reposition the electrodes outside the dense sheath of scar tissue forming around the shank. The onset of the deployment was delayed by around 20 s. This should leave sufficient time for a typical implantation of the probe shank (without the need for a pneumatic inserter). This experiment demonstrated that the developed actuation mechanism provides enough travel, force and appropriate timing.

The impedance of the fabricated electrodes, after plating PEDOT:pTS, was lowered to below 300 kOhm. This should suffice for most recording systems. The application of starch gel, Povidone iodine and PLGA did not increase the impedance of these electrodes much. This shows that electrodes with practical impedances can be fabricated at the end of the fine needles. Also, the hydrogel coatings appear to be compatible with the PEDOT:pTS plated electrodes.

The *in-vivo* experiment showed that neural probes with deploying electrodes can be inserted without causing much bleeding and explanted without breaking. The recorded waveforms indicate that the upper three electrodes picked up action potentials. Although no empirical evidence that

the electrodes indeed deployed after insertion was found, the experiments conducted on agar brain models, the piezoresistors measurements on the cadaver lamb brain, and the probes explanting with deployed electrodes during the *in-vivo* study, strongly suggest that the electrodes deployed after insertion.

2.13   Conclusions

This thesis chapter describes the development of the first practical prototypes of neural probes with deployable electrodes for enhance chronic stability. The experiments indicate that suitable mechanisms for this purpose were developed.

The developed mechanical actuation mechanism is based on hydrogel coated springs. The springs were coated with a starch based hydrogel for retraction and controlled deployment. The hydrogel is strong enough to almost completely retract the springs. After iodizing the starch and adding a layer of PLGA, the springs deploy delayed by 20 s after coming in contact with agar brain surrogate. This leaves sufficient time for insertion of a shank with many commonly used methods.

A special spring design based on a "roll on" deflection was developed. Using an agar brain surrogate, the springs were shown to provide sufficient force and travel to deploy electrodes by more than 120 µm. Literature indicates that this is sufficient to reach outside the dense sheath of scar tissue forming around the shank.

A FEM simulation was conducted that models the stress inside tissue around neural probes in response to the tissue moving with respect to the electrodes. The simulation compared the stress around a shank, around a shank with needles and around shank with springs and needles. The results indicate that the small geometries, like needles, amplify the stress compared to the shank

by a factor of 2-3. However, using flexible springs decreases the stress, in some cases to values slightly below those around the larger shank of traditional neural probes.

The impact of the developed starch and PLGA coatings on the electrodes was investigated by measuring impedance spectra. If the electrodes were plated with PEDOT:pTS the impedance only increased marginally and remained in a usable magnitude around 350 kΩ.

A pilot *in-vivo* study was conducted with the developed prototypes (omitting the PLGA coating since that was not employed until after the study was conducted). The study revealed that the developed prototypes could be inserted into nervous tissue and handled without requiring uncommon methods. The electrodes at the end of needles were able to record transient waveforms that are likely neural action potentials.

CHAPTER 3

STARCH HYDROGELS
FOR ACTUATION OF MICROMECHANICAL DEVICES

This chapter discusses starch hydrogels as mechanical actuators for micro-mechanical applications, especially in biomedical areas. Starch gel can be used for micro-machined sensors and actuators that need non-electrically triggered and driven one-time actuation or release mechanisms (e.g., stents, valves, one-time release devices). As exemplary application, starch hydrogel is used to retract and deploy silicon microsprings.

- Micrometer-thin starch hydrogel can compress a set of six 12 µm thick, 5 µm wide and 350 µm long silicon springs with 160 µm travel by approximately 140 µm. According to an analytical model, at this deflection, the springs collectively react with 1.2 mN.

- Immersed in water at or above room temperature (21 °C), the starch coated springs deploy within a few seconds. However, if the starch gel is iodized after dehydration, the springs deploy slowly and gradually (over the course of several tens of minutes) in water around body temperature (37 °C), after an initial jump of several tens of micrometers. If the water is at room temperature (21 °C) the springs deploy only partially and then stall.

- Starch hydrogel tolerates temperatures of 100 °C for 10 min without drastically changing the timing of the deployment of the springs. If the hydrogel was heated in air to 160 °C for

30 min, it dissolves quickly in water. If the gel was heated to 200 °C, the springs do not deploy at all. This property can be used to permanently fold structures in a self-assembly fashion.

- Starch is biodissolvable, it can be micromachined, it is currently employed in clinical applications for drug-delivery, and it is easy-to-use.

This chapter furthermore reports on mechanisms of applying, patterning and removing starch hydrogel, and ways of tailoring its properties.

3.1   Introduction

Hydrogels are polymer networks that are swollen with water, which can make up a large portion of their mass. Hydrogels have immense potential to form mechanical transducers, since changes in their amount of swelling are accompanied by large forces, travel, and are sensitive to various stimuli such as temperature or presence of ions [71].

Starch is a natural polymer found in grains of plants. It can form a hydrogel after being heated in presence of water. When coated on surfaces in hydrated state, it enacts strong forces on them during its dehydration. Starch hydrogel remains in compressed state until exposed to water. Then it swells at a controllable, temperature dependent rate.

There is a range of biomedical applications involving self-regulated devices involving mechanical actuation on the micro-scale, whose function depends on a slow or delayed (by several tens of minutes) response to the presence of water. For example, tetherless micro-grippers for biopsy [72], temporarily stiffening structures for implantation [73], valves for uptake/delivery, self-expanding stents [74], pacemaker electrode anchors, or self-implanting devices [34]. These applications will benefit from micrometer-thin materials that enable deployment during or shortly after positioning,

while minimally increasing device volume. However, materials with these properties are rare. While on the centimeter scale or larger, many hydrogels swell slowly due to long and slow diffusion paths [75], on the micrometer scale they gain in speed and operate within seconds [42]. Micrometer-thin, biodegradable gels made from agarose, gelatin, cellulose [31] or polyethylene glycol [52] tend to swell on a time scale of seconds, whereas materials that need to undergo chemical reactions for swelling or dissolving such as poly(lactic-co-glycolic-acid) tend to react abruptly and within several hours or even days [52]. As part of this thesis work, starch-based hydrogels are investigated for their ability to passively actuate micromechanical structures.

Starch is found in most green plants and is used for energy storage. It occurs in granular form and is stored in the chloroplasts in the leaves. Starch is commercially available as powder (Figure 51).

a) b)
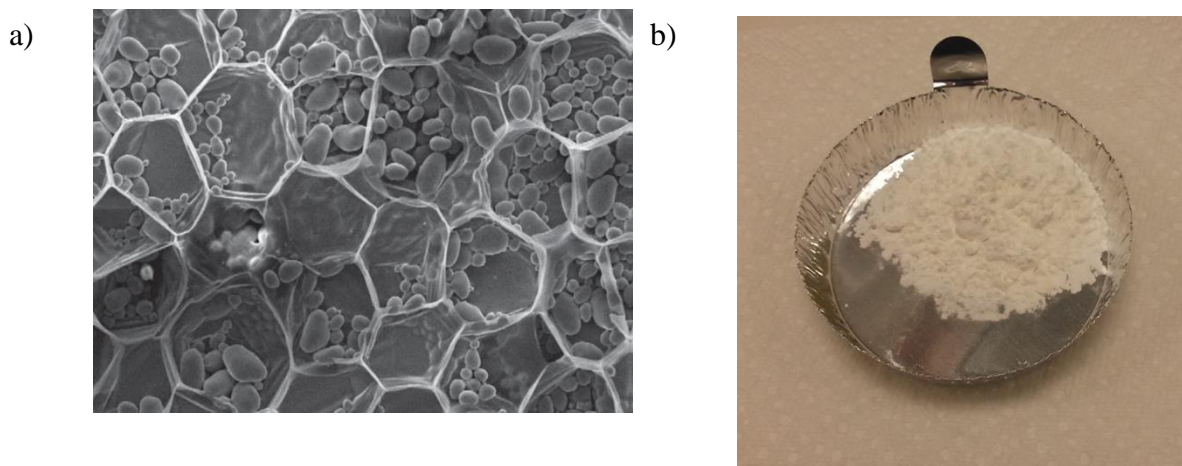
Figure 51 a) SEM image starch granules in cross-section of a stem **[76]** *b) commercially available starch powder.*

Starch granules consist of laminated sheets of bound glucose molecules. There are two molecules found in starch granules, distinguished by the way these glucose molecules are joined (Table 7). One is called amylose and is a linear molecule, the other one is called amylopectin and is branched. Both are formed by hundreds to thousands of cross-linked glucose molecules. Amylose and

amylopectin are very similar to glycogen, which serves as energy storage in animal cells. Starch is digested by many animals using a family of enzymes called amylase, which is cleaving it into small and soluble polysaccharides [77].

Starch granules become soluble in water heated above 60 °C. This process is called gelatinization [78]. When cooled after heating in water, starch forms a network that retains water, acting as a sticky gel [79]. This process is called retrogradation. Table 6 shows the arrangement of amylose and amylopectin during gelatinization and retrogradation. In this process amylose irreversibly leaches out of the granules, solving in water. The amylose and amylopectin molecules associate with each other using hydrogen bonds, still carrying water molecules. Micrometer thin layers of this retrograded starch gel undergo strong shrinking during dehydration. And conversely, dried, retrograded starch gel swells strongly when exposed to water.

Table 6: Sketch of the molecular structure of starch during gelatinization and retrogradation –adapted from [80].
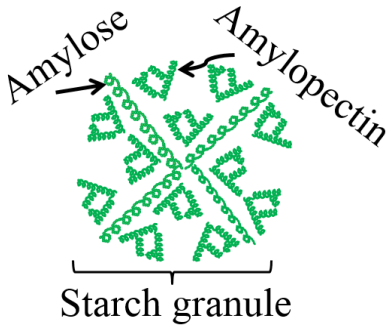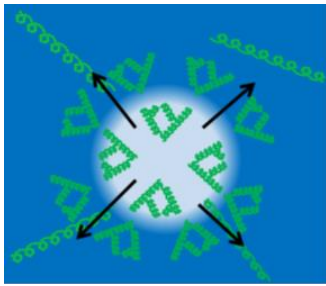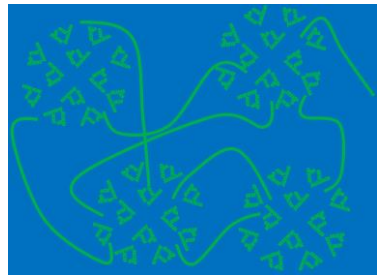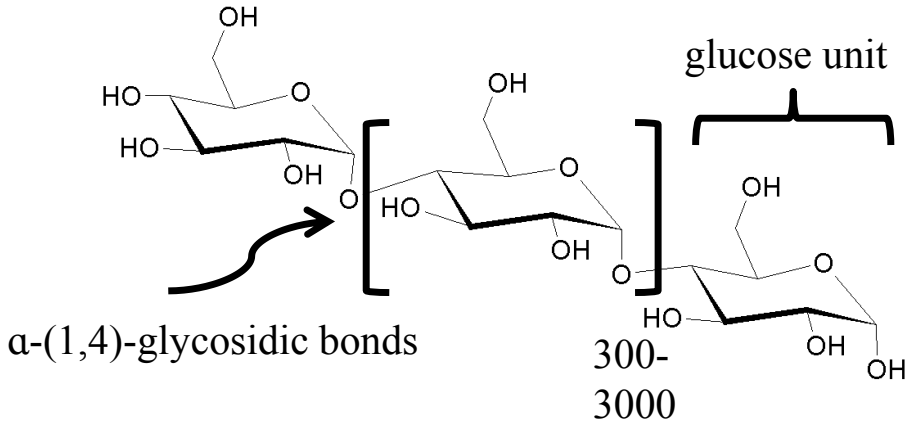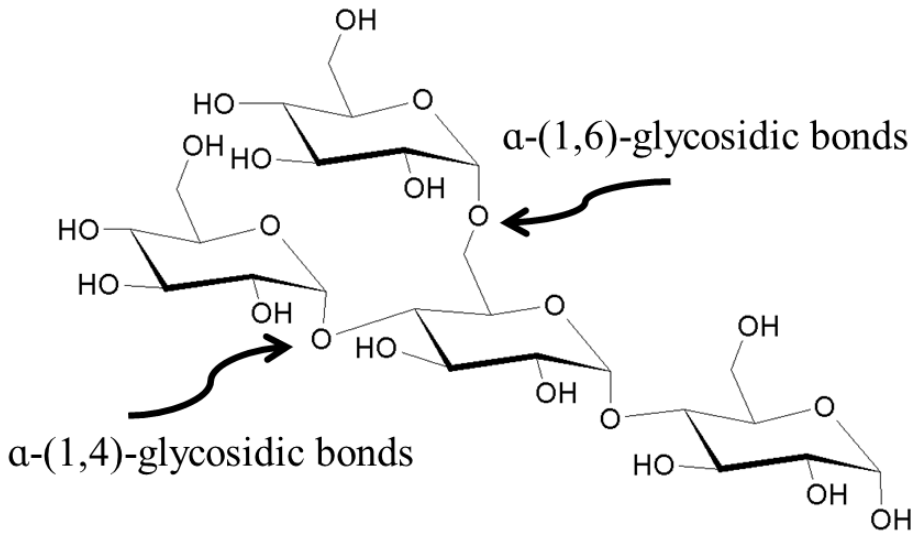
Dry starch granule consisting of amylose and amylopectin molecules.	Gelling starch granules - During heating in water amylose leaches outside the grains.	Retrograded starch gel - Amylose molecules form network and link amylopectin molecules.

Table 7: Chemical structure of starch, consisting of amylose and amylopectin.

Amylose molucules consist of 300-3000 α(1,4) linearly linked glucose units arranged in a helical structure	
α-(1,4)-glycosidic bonds glucose unit 300-3000	
Amylopectin molucure consisting of α(1,4) linked glucose units arranged in a helical structure with occasional branches formed by α(1,6) bonds	
α-(1,6)-glycosidic bonds α-(1,4)-glycosidic bonds	

Starch has been used to test for the presence of iodine and vice versa; together they complex, triiodide enters the helical structure of starch, producing a purple-black color (Figure 52a and b) [81]. The starch iodine complex is stable up to 40 ^{o}C. Interestingly, iodine is hydrophobic and iodizing starch can restrict swelling in water [82].
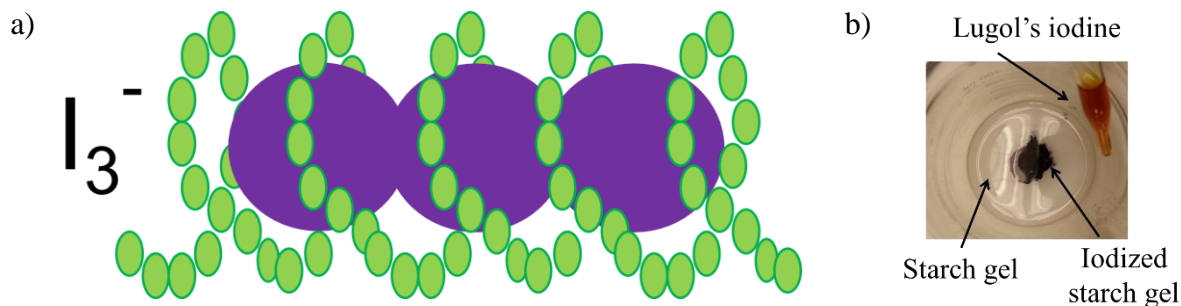
Figure 52: a) Sketch illustrating the structure of the starch-iodine complex based on **[81]** *b) characteristic dark blue color of the starch-iodine complex.*

This property led to the concept investigated in this thesis: Modulating the swelling of starch gel in water by iodizing. It is hypothesized that the relatively fast water diffusion is not an appropriate time-determining step for desired swelling of the starch gel. However, after iodizing, first the iodine concentration needs to drop sufficiently before considerable water swelling can commence. Hence relatively slow iodine diffusion becomes the time-determining step of gel swelling. This concept is summarized in Figure 53:

a)

Slow iodine diffusion

micrometer thin
starch hydrogel

b)

Fast water diffusion
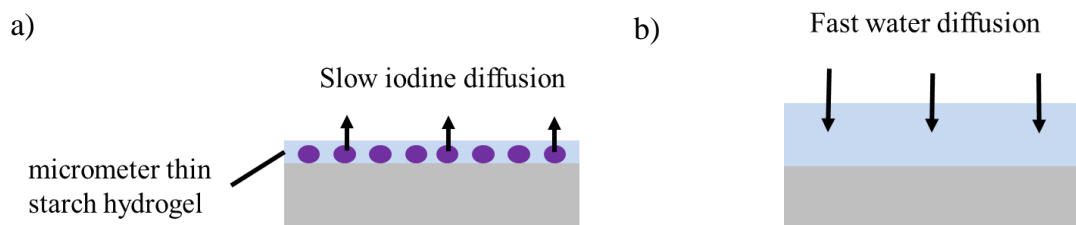
Figure 53: Illustration of the concept of modulating the swelling of starch gel by iodizing. One interpretation is that iodizing restricts swelling of starch gel. Until the concentration of iodine inside the starch gel sufficiently dropped, the gel does not swell much. This makes the relatively slow iodine diffusion the time-determining step, rather than the fast water diffusion.

Starch has been well researched and used in a wide variety of applications. It is an attractive substrate for biomedical and pharmaceutical uses, such as bone fixation and replacement because of its biodegradability and mechanical robustness [83, 76]. It is used as carrier for controlled release of drugs [84] - for example in form of cadexomer-iodine, a starch-based iodine continuous-release material developed to cleanse wounds and exert an anti-bacterial effect without damaging surrounding tissue [85]. In industrial applications starch is used as biodegradable adhesive in the papermaking process. In food production starch is used in staple foods and serves as a nutrient or as a thickener. The shape memory property of starch has been employed to form mechanical actuators on the centimeter-scale for biomedical applications [86]. Starch is easy-to-use, and reagent grade starch is commercially available at low cost from various suppliers, including Sigma Aldrich.

This thesis chapter contains an investigation of the properties of starch hydrogel relevant to form mechanical micro-actuators on the millimeter to micrometer-scale, especially for bioMEMS (micro electromechanical systems) applications. As exemplary substrate, microfabricated neural probes with integrated springs are used, which are discussed in Chapter 2. The purpose of this

actuator is to deploy electrodes away from a neural probe shank after insertion into cortical tissue (Figure 6). The deployed electrodes are hypothesized to interface with neurons that are least impaired by the implantation. In this application, starch gel serves multiple purposes: it is retracting springs, locking them in place and slowly releasing them.

 The investigations in this chapter include methods of coating and patterning starch on micrometer sized devices, characterization of the ability of starch to compress or retract structures during dehydration and the ability of starch to release these structures during swelling. Furthermore, some investigations of the process compatibility of starch gel are presented.

The following section is divided into five parts:

- Description of the springs, serving as exemplary substrates

- Preparation of starch gel, and how it is applied to substrates

- Starch gel compressing springs during dehydration

- Patterning and process compatibility of starch gel

- Starch-coated springs deploy in water as a function of water temperature

3.2   Springs

The experiments were performed on springs with 120, 160 and 200 μm travel. All springs were 5 μm wide and 12 μm thick. The springs consisted in sets of six, all in parallel connection. The spring arms were connected by a bar (Figure 54 and Figure 55). All springs were made out of silicon. Figure 56 shows SEM images of fabricated springs.
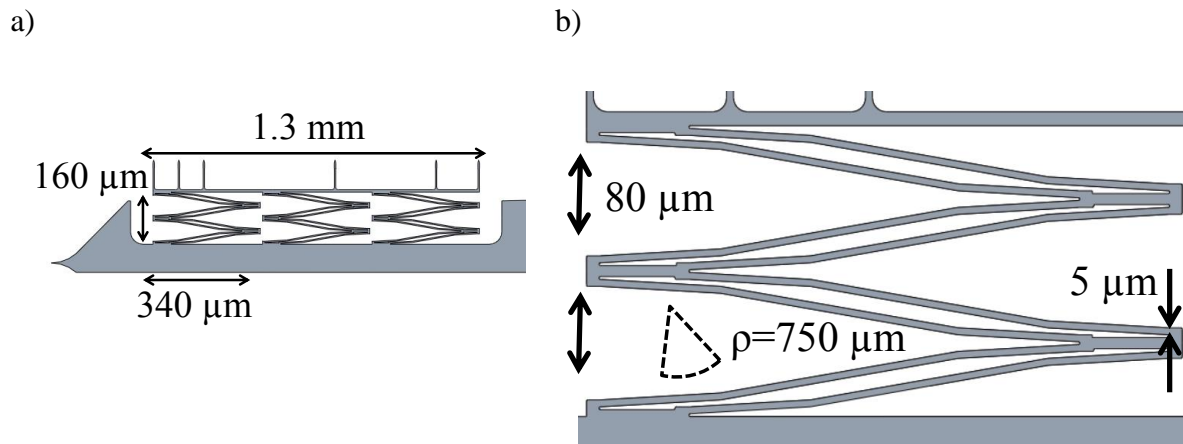
Figure 54: Dimensions of the silicon springs used as exemplary substrate. All designs had 12 μm uniform thickness and 5 μm width. a) drawing of a set of six springs with 160 μm travel b) close-up on one pair of springs
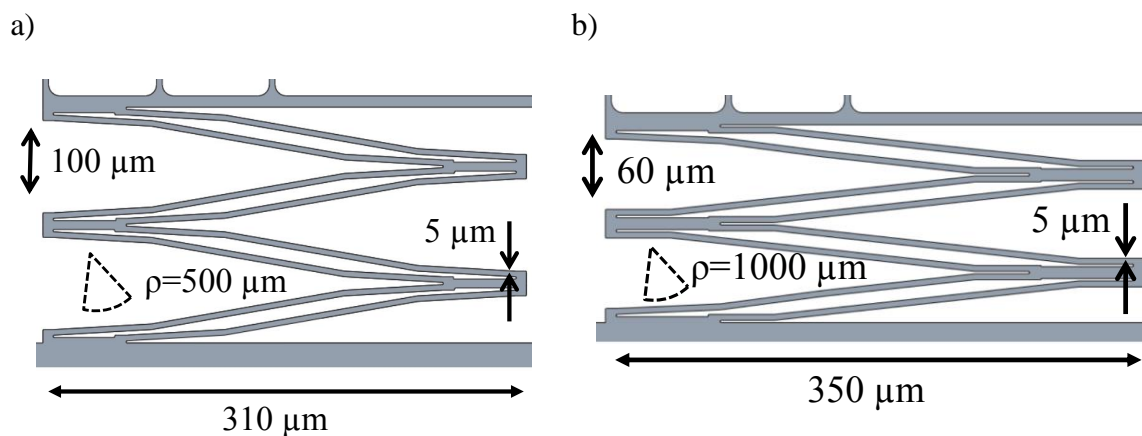
Figure 55: Close up on a set of springs with a) 120 μm travel b) 200 μm travel to show the dimensions.

a)
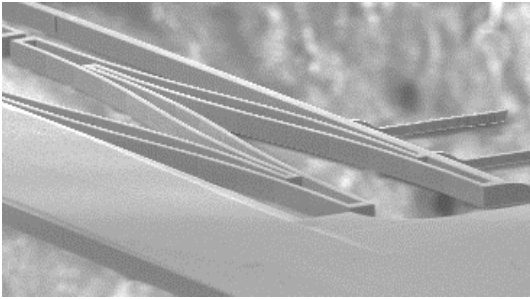
b)
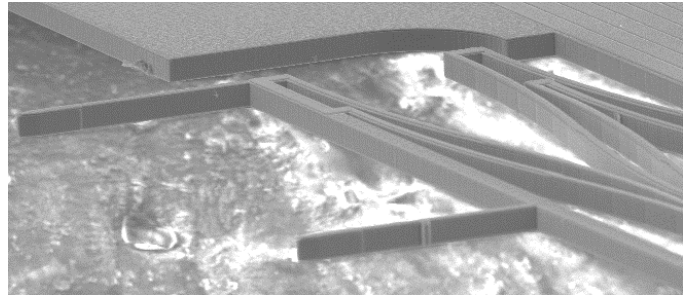
Figure 56: SEM images of silicon microsprings. a) and b) show different perspectives.

The springs are modeled to have a fairly linear force-deflection curve until almost fully retracted (Section 2.3 includes a detailed description of this model). The approximated spring constant of the springs with 160 µm travel (most frequently used), at low deflections, is 6.7 N m^{-1}. They collectively exert 1.26 mN when retracted by 140 µm. Figure 57 shows the load-deflection curves of these three spring designs.
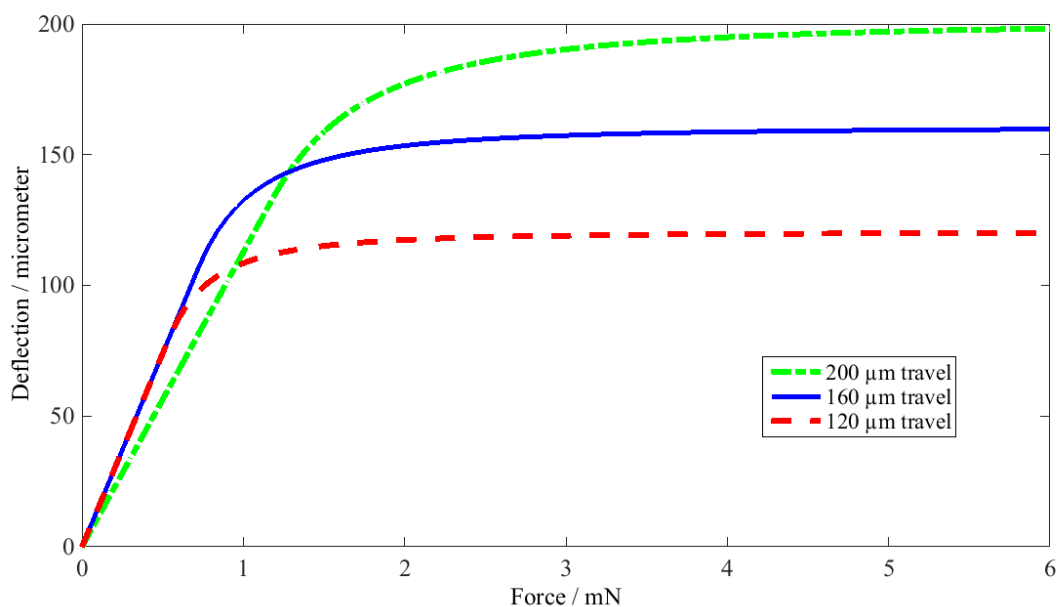
Figure 57: Analytically modelled force-deflection curves of the three spring designs used.

3.3 Starch gel preparation

All experiments were conducted with a modified high amylose corn starch called "Crisp Film Starch", obtained from Ingredion (Bridgewater, USA). The starch gel was prepared by boiling 5 g of starch granules in deionized water under stirring at 300 rpm on a hotplate for 90 min. The water was replenished as it evaporated. After approximately one hour of heating, the starch was poured through a strainer with a 500 μm pore size in order to achieve a finer gel.

In some cases starch gel was iodized after coating: For that, the starch coated probes were first immersed into deionized water for 5 s, then into 0.5 % iodine/potassium-iodide solution for 10 s (Lugol's solution), then back into deionized water for 5 s, and finally left air-drying for at least 2 hrs.

3.4 Starch gel: Coating and Compression

Methods

The coating setup consisted of a microscope with a camera mount, a fan and a fine syringe (Figure 58). The starch was dispensed on the springs using a fine needle. The springs were mounted to a printed circuit board (PCB) which was glued on a glass slide. The springs were observed through the microscope. A fan blew air on the springs to accelerate dehydration after coating. After boiling, a small part of the hot starch gel was filled into the syringe. Starch gel remained solved in water for several tens of minutes (but then needed to be freshly drawn from the remaining heated supply). A small drop was formed at the tip of the needle and was then dispensed on the substrates by drawing the drop across them. To achieve thicker coatings, the drop was drawn over the springs multiple times (allowing the gel to dehydrate between each cycle). For the spring retraction and deployment experiments, the starch gel was allowed to further dehydrate for at least 2 hrs.
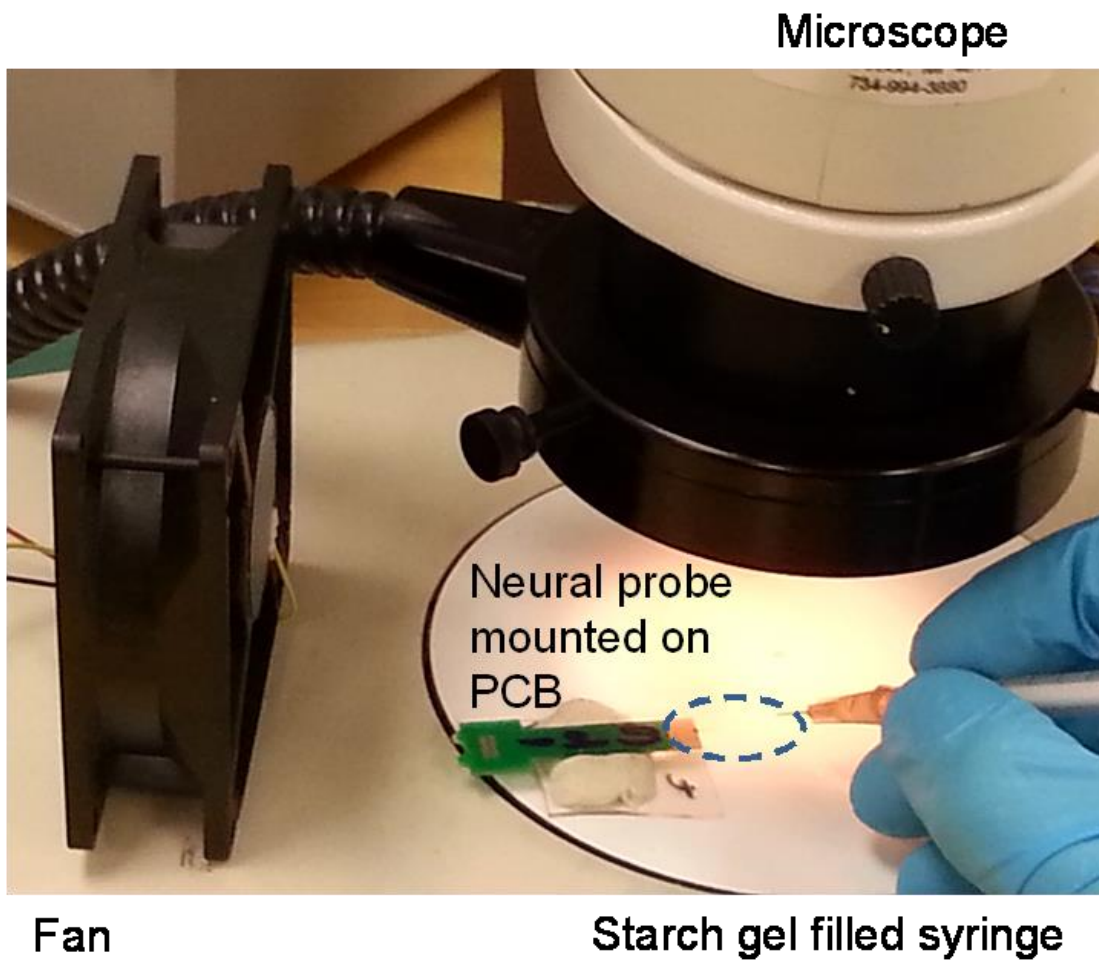
Figure 58: Setup for coating starch onto neural probes with springs mounted on a printed circuit board.

In early experiments, the springs were coated with starch gel by dip-coating. For that, the springs were immersed multiple times into boiling starch gel and then pulled back at approximately 2 mm/s. Since dispensing starch gel from a syringe produced more desirable results, dip-coating was abandoned. All other experiments were conducted with dispensed starch.

Spin-coating is a method often used in microfabrication. Hence it was explored how starch gel can be spun on glass cover slips. For that, boiled starch gel was dispensed on glass cover slips mounted on a spin coater and spun for 30 s at 1 to 5 krpm in steps of 1 krpm.

Results

Figure 59 shows SEM images of silicon springs coated with starch gel by dispensing from a syringe. The starch gel distributed across larger surfaces of the substrate and in between the springs. It did not stick to the 5μm narrow needles or to pointy the tip of the shank.
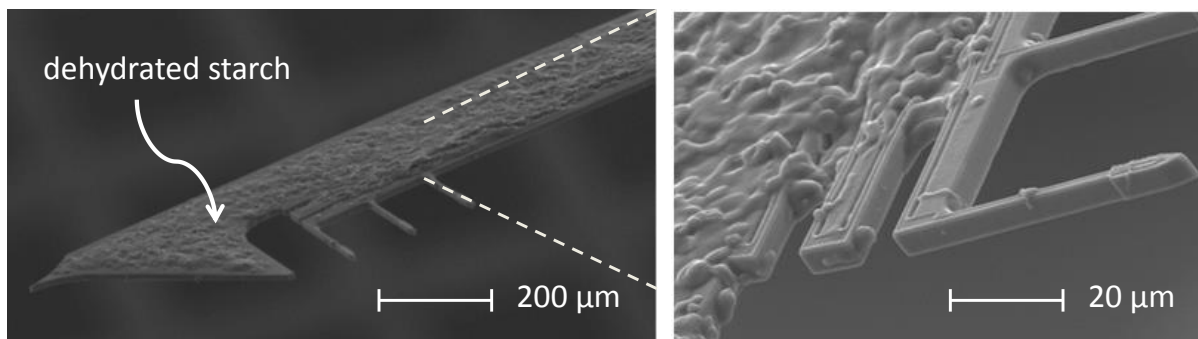
Figure 59: Starch-gel coated silicon neural probe shank. The starch distributed across larger surfaces and did not cover micrometer fine, freestanding structures. The shank remained straight after the starch dehydrated.

Figure 60 shows a series of micrographs of springs coated in starch that were retracting while the starch dries. With increasing starch thickness, it took increasingly longer for the starch to dehydrate. For thicknesses in excess of several microns, the starch appeared to be dehydrated after 2–3 minutes. The springs retracted increasingly further with increasing starch thickness.

Table 8 shows how starch gel compressed springs with different maximum travel.
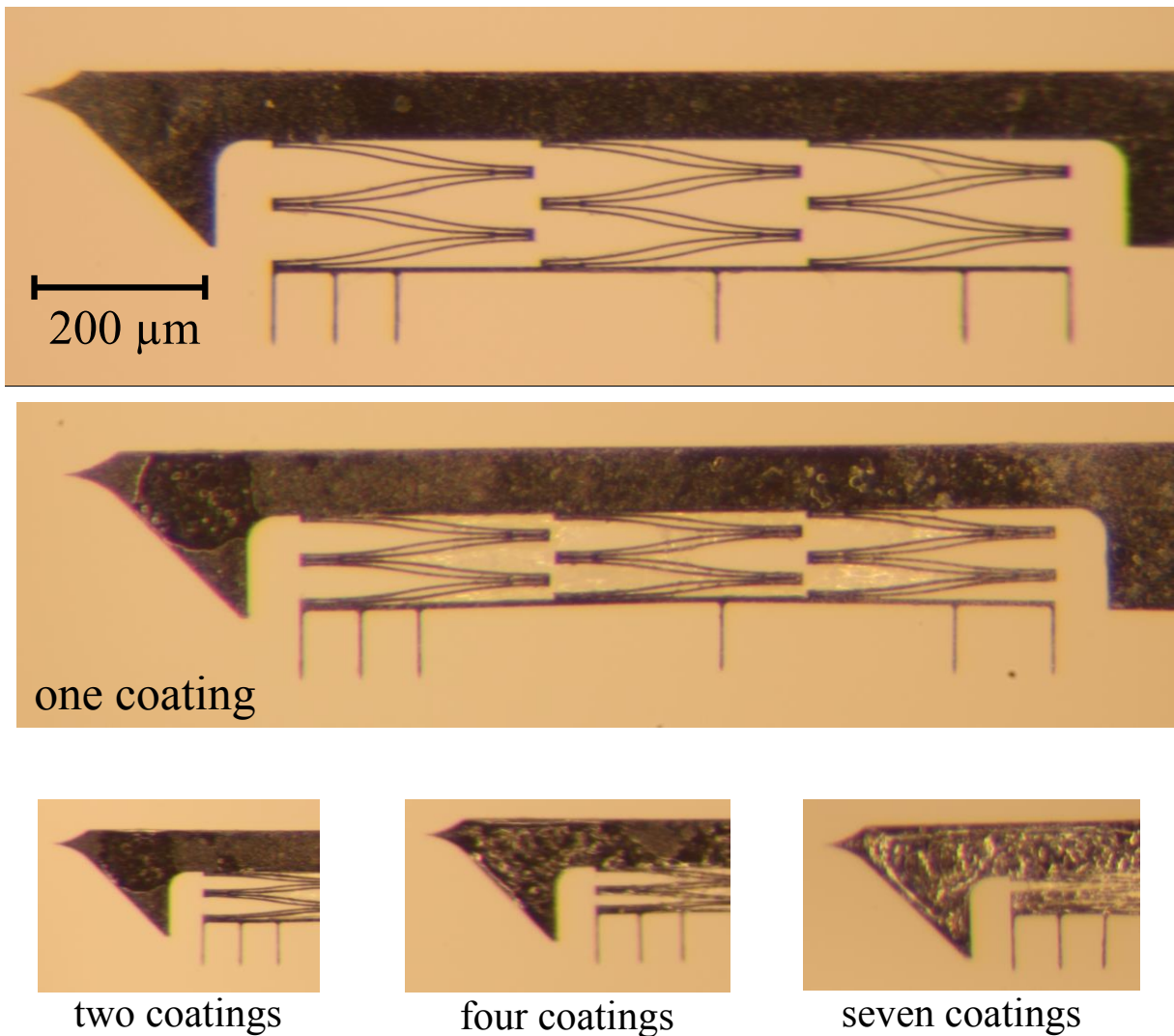
Figure 60: The springs retracted increasingly further with increasing the amount of starch gel coated on them. The images were taken after the starch dehydrated. The starch gel was applied in several separate coatings using a small syringe. Springs with 160 μm travel are shown.

Table 8: Springs with varying travel, before and after coating with starch.
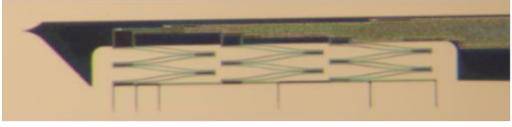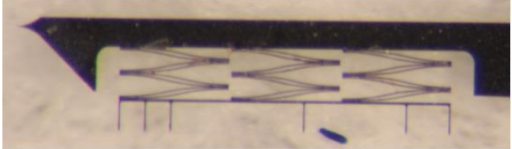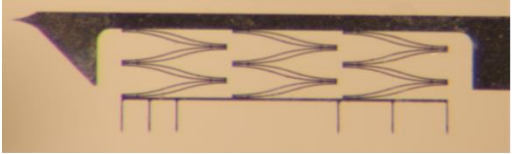
Before coating	After coating
Spring design: 120 µm travel	Springs retracted by 91 µm
Spring design: 160 µm travel	Springs retracted by 106 µm
Spring design: 200 µm travel	Springs retracted by 128 µm

Figure 61 shows how iodizing the starch gel lead to additional compression of the springs. This effect was more pronounced in large travel springs. In extreme cases, iodizing lead to the starch peeling off the silicon springs, or forming cracks.

a)   Dehydrated ≈ 128 µm retracted
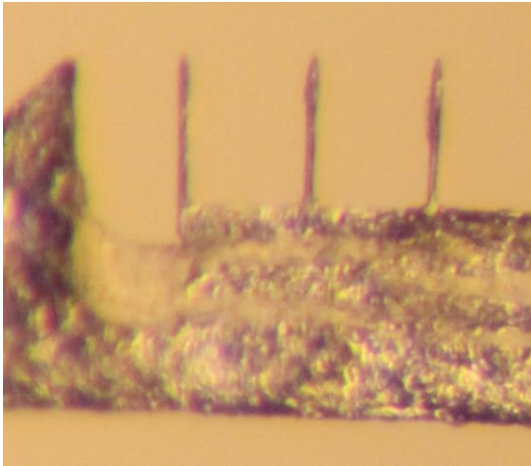
b)   Iodized ≈ 143 µm retracted
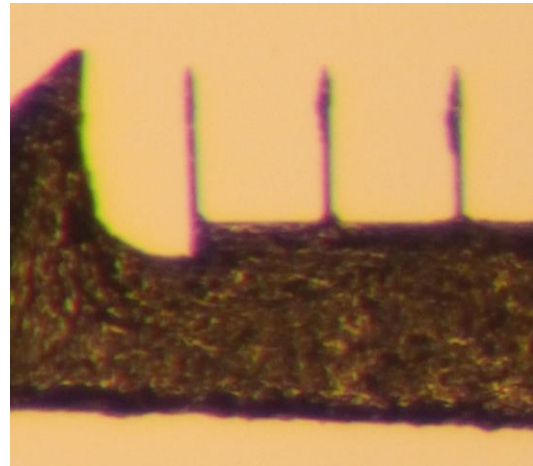
Figure 61: Starch-coated springs before and after iodizing (springs with 200 µm travel).

Figure 62 shows images of silicon neural probes coated with starch gel by dip-coating. The starch gel completely coated the springs and bridged larger gaps.

a)
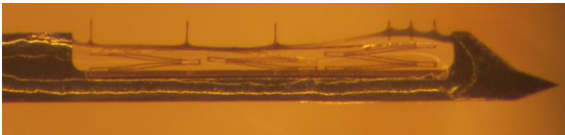
b)

Figure 62: Images of silicon springs after four repeated starch gel dip-coats a).right after coating, during dehydration b) after dehydration

In some cases, starch gel applied by dip-coating lead to undesired bending of the substrate (Figure 63a). Starch applied with a syringe in a controlled way, was used to fold the springs in a 90 ° angle (Figure 63b and Figure 63c).

a)
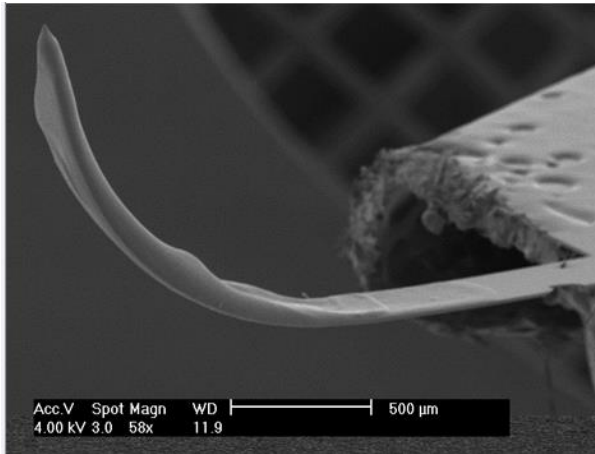
c)
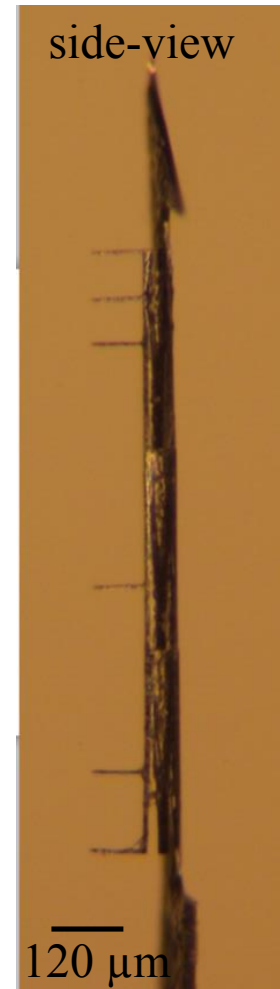
b)
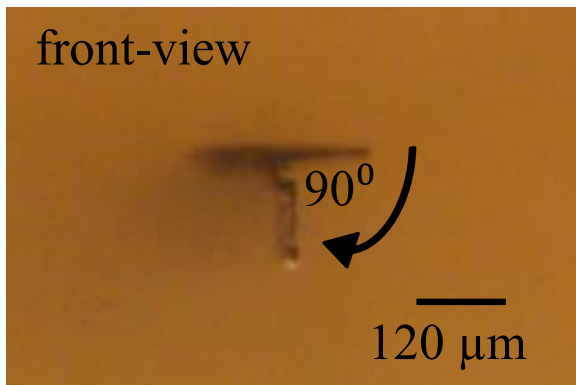
Figure 63: a) Starch gel applied by dip-coating lead to undesired bending of the substrate, b) and c) Starch applied with a syringe in a controlled way used to fold springs in a 90 ° angle.

Figure 64 shows edges of springs, in an early design, that were retracted by starch-hydrogel. The springs cracked in characteristic locations.

a)
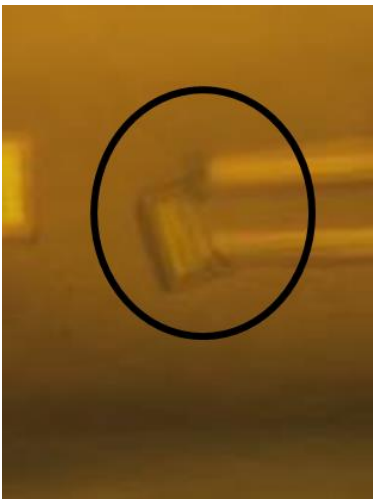
b)
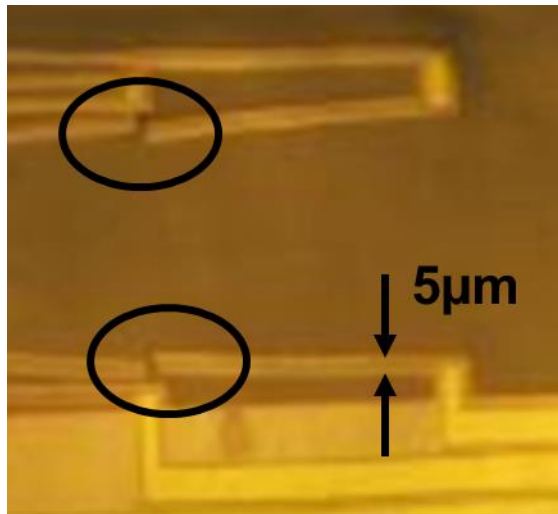
Figure 64: Images a) and b) show edges of springs that cracked during retraction by starch-hydrogel.

The average thickness of the starch spin-coated on glass slides was 1 μm (5 krpm), 0.8 μm (4 krpm), 0.7 μm (3 krpm), 0.6 μm (2 krpm) and 0.5 μm (1 krpm), measured after dehydration.

It was sometimes observed that the starch formed cracks when stored at room temperature for several days after dehydration. However, if the dried gel was stored at −7°C, that was prevented.

Discussion

Starch is easy, cheap and fast to acquire. Processing starch gel does not require unusual equipment or long preparation times.

Applying starch

Dip-coating starch allows surfaces with complex, hard accessible geometries to be coated. It is a fast process that can be applied to multiple devices in parallel. However, the distribution of starch gel was not very uniform in many cases, often the tips and one side of the springs were coated with a thicker layer that led to undesired bending. Also, it was hard to repeatedly achieve layers with exactly the same thickness.

Dispensing starch with syringes allows for precise control of the distribution of starch (on the order of 50 µm). The process is still relatively fast. This method is only applicable when all structures to be coated can be easily reached by a syringe. Therefore, they cannot be spaced too closely. The tips of the shanks and the needles did not retain much starch gel and remained sharp. This is likely caused by the surface tension of the drop of water that distributes the starch. The water drop distributes itself in a way that minimizes surface energy. If the surfaces were extremely hydrophilic, the starch would most likely distribute more evenly and also cover tips and needles.

The experiment involving spin-coating starch gel shows that it can be spun to micrometer thin layers. This might be of value for wafer-level processing, especially when only one side of the substrate needs to be covered. For example, this is the case when starch-gel is used to fold structures in a self-assembly fashion. Spin-coating might offer a more repeatable, parallel and fast way of coating substrates with starch-gel.

Compressing

Micrometer thin layers of starch gel seem well suited to quickly (within seconds) enact strong compressive stress (mN) over relatively large distances (160 µm) on coated structures during dehydration. When the coated structures deform, dehydrating starch gel is able to almost completely collapse them, leaving only micrometer sized gaps in between. The 5-µm-wide silicon

114

springs had to be reinforced in regions exposed to high leverage in order to prevent them from breaking during starch dehydration. One limitation became obvious: as structures with larger gaps were coated with starch, the dehydrating gel left larger gaps in between these structures. The experiments compare, for example, a spring design with 160 µm of travel to a spring design with 120 µm travel. The former, although having 40 µm more travel, only retracted 15 µm further. Another design with 200 µm of travel only provided 27 µm additional retracted distance. It appears that increasingly more starch gel remained trapped between the structures. This prevented them from collapsing further. In general, springs with narrow gaps compressed leaving smaller gaps than springs with wide gaps.

Compressing starch could serve applications reaching from compressing, folding, breaking or destroying structures.

3.5   Patterning

Methods

Various methods of removing starch gel after it has been coated were investigated. Once applied, starch gel was etched using various wet etchants. These include boiling water, diluted hydrochloric acid (20%) and an α-amylase solution at 37 °C. α-amylase is used by humans and some other mammals to break down starch into small, soluble polysaccharides [77]. The α-amylase solution was prepared as 0.1% v/v concentration with 0.9 % w/v NaCl and DI water (physiological saline). The starch coated springs were dipped into the respective etchants (several minutes for the boiling water and the hydrochloric acid solutions, and 10 hours for the α-amylase solution).

Starch was also dry-etched in oxygen plasma at room temperature. For that, starch gel was spin-coated to glass cover slips and dehydrated. The starch was then partially covered with polyimide

film. To etch it, it was exposed to reactive ion etching in oxygen plasma at 250 mT, 800 W, with an oxygen flow rate of 100 scc for 240s using a Glen 1000P Asher (Glen Technologies Inc.).

Another way of patterning starch was investigated. Instead of conformally applying starch and removing it from undesired locations, it was attempted to prevent starch from coating certain areas of the substrate in the first place. In order to prevent starch from coating parts of a substrate, a thin layer of extremely hydrophobic fluorpolymers, distributed under the name Cytop (Bellexinternational, Wilmington, DE, USA) was applied.

Results

Figure 66 shows probe shanks that were coated with starch and subsequently etched. Boiling water and hydrochloric acid (20%) were able to completely remove starch from the springs within a few minutes. The α-amylase solution removed most parts of the starch from springs within several hours, leaving back some residues. CYTOP prevented starch gel from wicking on pads adjacent to springs. Oxygen plasma cleanly etched exposed starch gel spin-coated on a glass slide (Figure 65). The portion of the gel that was covered by Kapton foil did not get etched.

a) etched in HCl
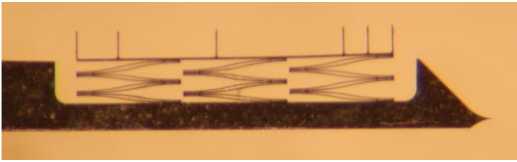
b) etched in amylase solution

c) applied on silicon
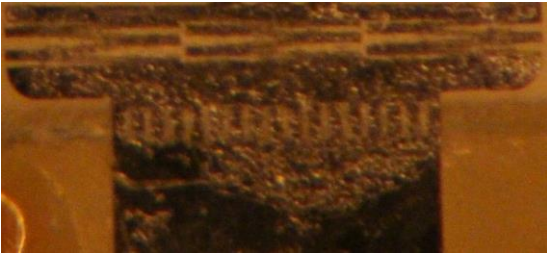
d) applied on CYTOP
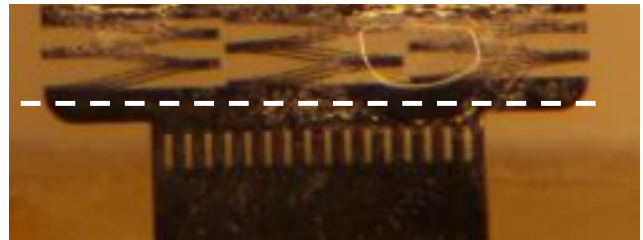
Figure 65: Micrographs of starch gel patterned by a) hydrochloric acid, b) amylase. c) Starch coated on silicon springs is also covering adjacent structures. d) Prior to starch-coating, adjacent structures covered with a hydrophobic polymer coating (CYTOP). In this case, starch does not spread past the springs.
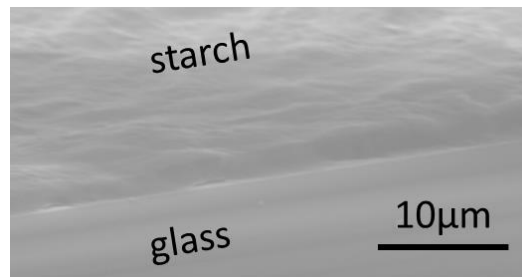
Figure 66: SEM picture of starch gel that was spin-coated on a glass slide, partly masked with Kapton tape and subsequently etched in oxygen plasma. The top part of the image shows starch gel that was covered by the Kapton tape.

Starch can be removed from substrates using many dry or wet etching methods. The choice of etch mask is likely the more tricky aspect. Photoresist, as common etch mask in microfabrication, requires a high temperature baking step and developing in water-containing solutions. The exposure to water likely makes the starch gel underneath the etch mask swell. This could distort patterns and cause delamination of the photoresist. Alternatively, patterned polyimide tape, similar to the Kapton tape used here, could be used as etch mask. Starch is fairly tolerant to exposure to typical conditions during processing. The experiments showed that starch gel did not dissolve in water at 21 °C, and dry starch gel could tolerate temperatures of 100 °C in air for several minutes without changing properties dramatically.

3.6   Deploying

The set of experiments shown in this section explores how fast and far starch coated springs deploy in water and some factors that influence the deployment.

Methods

The starch coated springs were deployed in a temperature controlled water bath. They were observed using a camera with zoom lens, connected to a computer with a USB video adapter for recording (Figure 67). The springs were observed through a custom-made container with a planar glass side facing the camera. Releasing the springs may be caused by softening, rupturing or swelling of the starch gel. The temperature of the water bath was regulated using a PID controller (HYDROFARM, USA), controlling the power to a hotplate. The water bath was kept at temperatures of 21 ⁰C, 37 ⁰C or 70 ⁰C.

It was also investigated how exposing dehydrated starch gel to hot air changed the deploying characteristics. Three sets of experiments were conducted. For that, the starch coated springs were first exposed to:

- 100 ^{o}C (10 min) and were iodized subsequently

- 160 ^{o}C (30 min) and were not iodized

- 200 ^{o}C (2 min) after iodizing
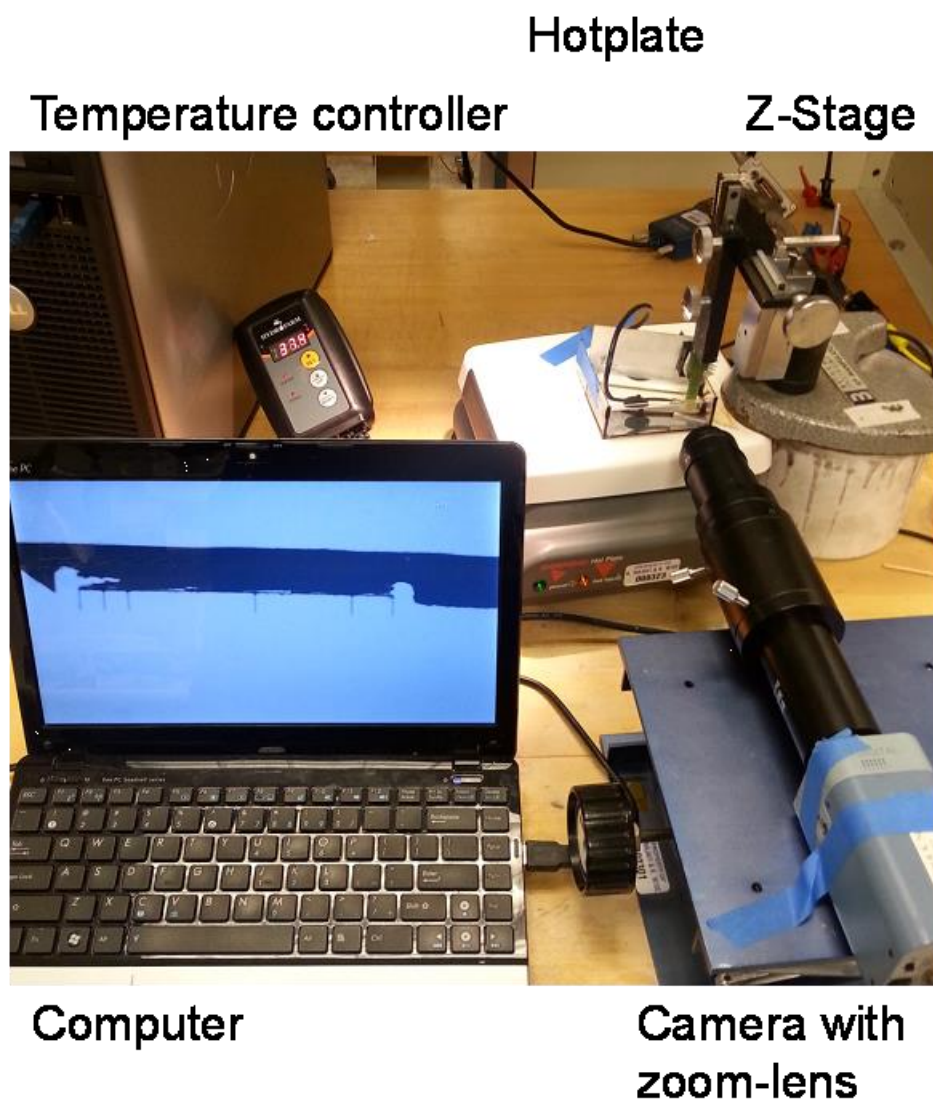
Figure 67: Setup to video-record starch-coated springs in a temperature controlled water bath.

In summary the following experiments concerning deploying starch were conducted in this section:

- Deploy springs coated with starch gel (not iodized) in water at 37 °C
- Deploy springs coated with iodized starch gel in water at 21 °C, 37 °C and 70 °C

- Deploy springs coated with iodized starch gel in water at 37 °C after being exposed to air temperatures of 100 °C for 10 min, to 160 °C for 30 min, and to 200 °C for 2 min

Results

When retracted springs, coated with starch gel, were immersed in water at 37 °C, they deployed almost fully within a few seconds (Figure 68). Dehydration and deploying of starch coated springs in water at 37 °C could be cycled without changing the apparent behavior much.
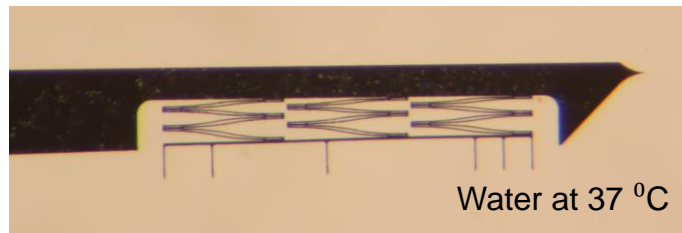
Figure 68: Springs coated with dehydrated starch gel, few seconds after immersion into water at 37 °C.

When the starch was iodized before immersion into water, the springs deployed considerably more slowly in water at 37 °C (Figure 69 and Figure 70). The graph in Figure 70 shows the distance the springs deployed, averaged over four trials. Each individual measurement is shown in Figure 98 in the appendix.
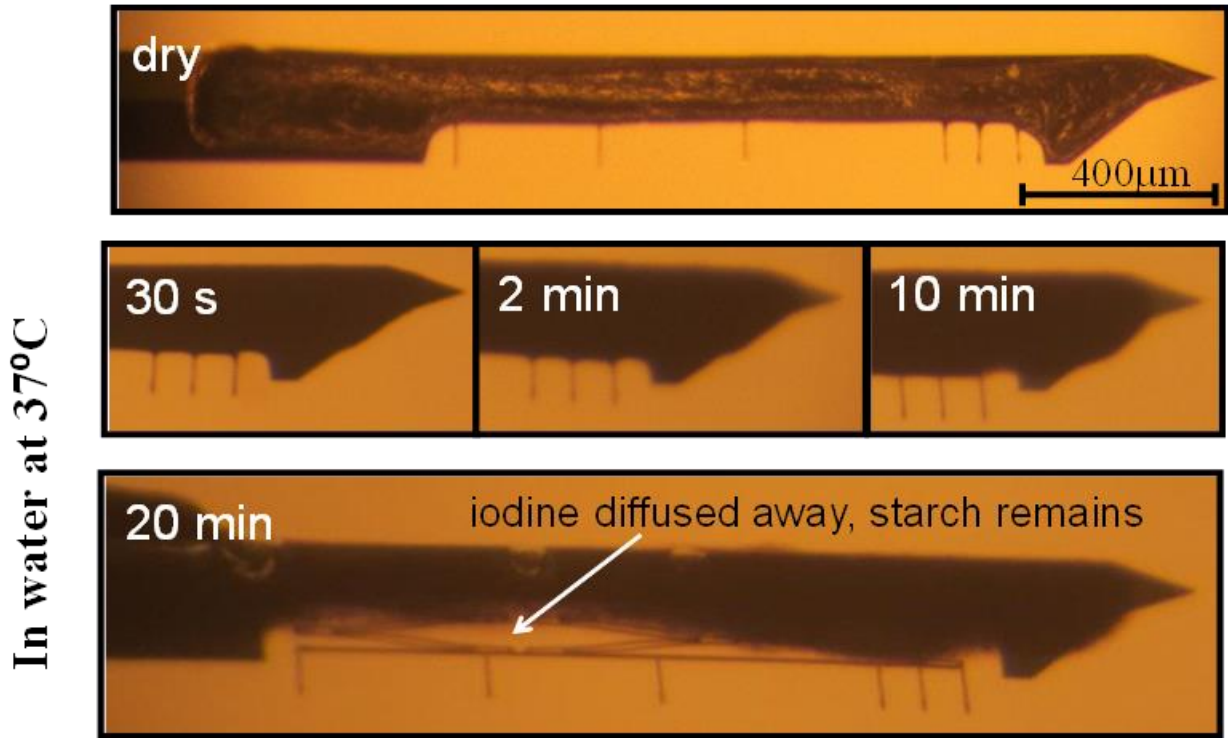
Figure 69: Deployment of iodized-starch coated springs in water at 37 °C. The first image shows retracted springs in air. After an initial jump, the springs deployed gradually and the starch became transparent. Springs with 120 μm travel were used for this experiment.
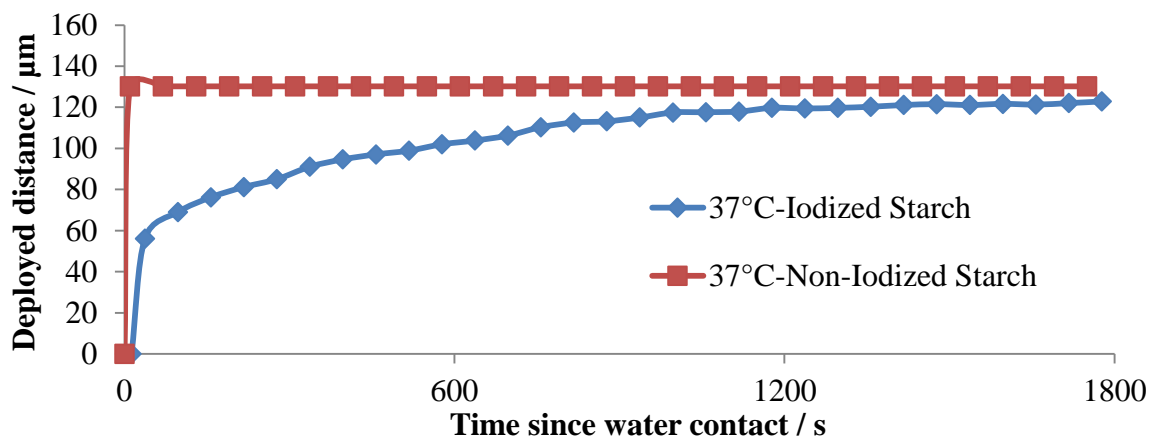
Figure 70: Graph showing the deployed distance of the springs versus time soaked. The measurements were averaged over four runs. Springs with 160 μm travel were used for this experiment.

An initial jump in deployment was evident: Within the first few seconds of contact with water, the springs (160 μm travel) deployed between 40 and 60 μm. Subsequently, the springs continued to deploy slowly and gradually to 110 -130 μm, within several tens of minutes. During this soaking time the starch became transparent. If the starch was iodized again after deploying and dehydration, the springs deployed similarly in an additional cycle. If the starch was not re-iodized, the springs deployed similarly to those that were not iodized in the first place.

The speed the springs, coated with iodized starch, deployed with, was strongly dependent on the temperature of the water. Around 21 °C the springs deployed to some extent. But after this initial quick deployment they stalled. At 70 ⁰C the springs were released almost instantaneously, similar to springs coated with starch gel that was not iodized (Figure 71) – these measurements were also averaged over four runs.
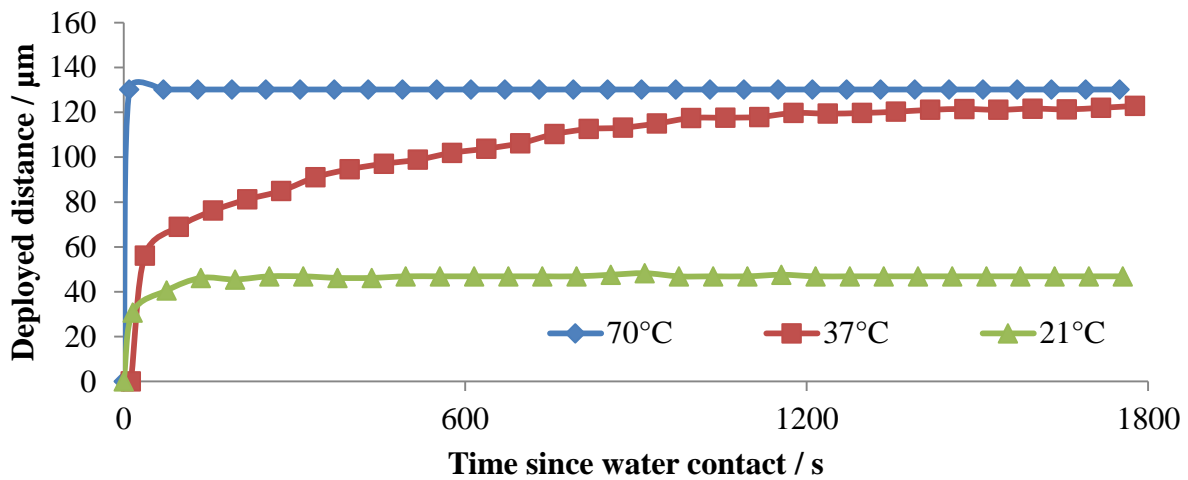
Figure 71: The deployment of springs, coated with iodized starch, was strongly dependent on the temperature of the water bath: they deployed only partially at 21 ^{0}C, slowly and almost fully at around 37 ^{0}C, and almost instantaneously and fully at 70 ^{0}C. The measurements were averaged over four runs.

Starch gel that was exposed to various air temperatures after dehydration and coating, deployed as follows: 100 °C for 10 min did not change the deployment characteristics fundamentally, 160 °C for 30 min lead to the springs deploying almost instantaneously and exposure to 200 °C for 2 min lead to the springs not deploying at all (Figure 72). The individual measurements of springs deploying after air exposure at 100 °C are shown in the appendix in Figure 97. Figure 73 shows springs coated with iodized starch gel that was exposed to 200 °C for 2 min.
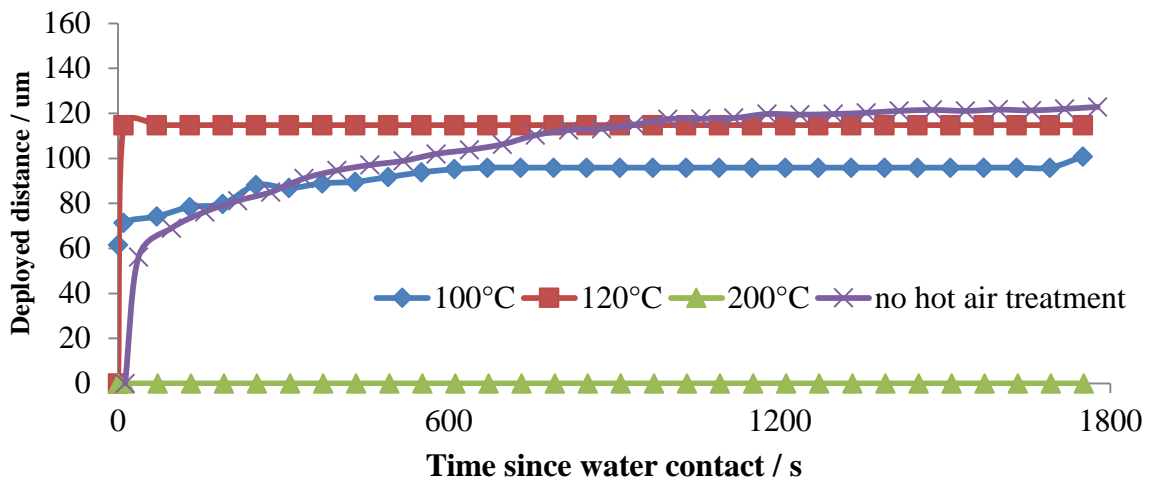
Figure 72: Starch gel, heated in air to 100 °C, 120 °C and 200 °C, deploying springs in water at 37 °C. For comparison, a curve showing deploying without hot air exposure is also plotted.
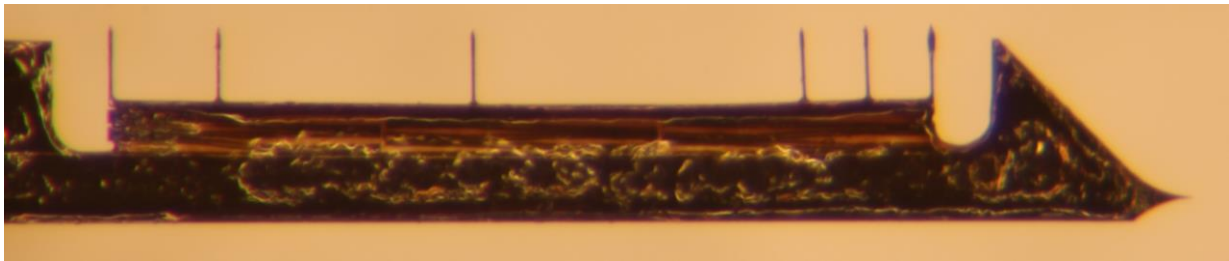
Figure 73: Starch coated springs after heating in air at 200 °C for 2min. The starch showed a caramel-transparent color.

The volume change of starch gel during swelling was occurring in all directions. The few-micrometer-thick dehydrated starch gel expanded to 40 μm thickness (Figure 74a and b).

b)
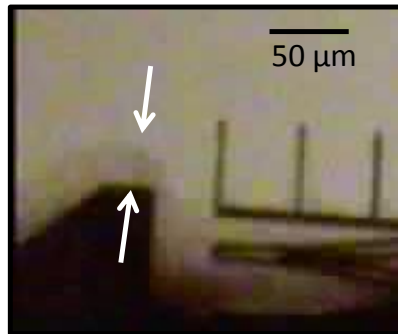
Figure 74: a)-side view and b) front view of starch coating swollen to several tens of microns in thickness.

<u>Discussion</u>

In the experiments, the position of the springs was used to conclude properties of the swelling starch gel. Releasing the springs may be caused by softening, rupturing or swelling of the starch gel.

Pure starch gel

Springs coated with micrometer-thin, pure starch gel released within a few seconds in water at 37 °C. The springs were almost fully, but not completely deployed. Since the starch gel did not dissolve, dehydration and deployment can be cycled. This can be desirable in applications where

a fast response time is needed, or a triggered release is needed. The swelling occurs isotropically; as the springs release, the starch gel also expands sideways, by several tens of micrometers. A possible advantage of that is that it forms a soft buffer layer. A disadvantage could be, that the volume of the device is increased. When implanted into tissue, surrounding tissue/material is pushed away.

Iodized starch gel

Previous work shows that hydrogels were modified to swell slowly in water by creating long diffusion paths, if enough volume is available, or by making the diffusion paths slow by adding hydrophobic groups [75, 87]. This might be troublesome to apply to micrometer thin gels with large surface to volume ratios, which are to respond within minutes rather than seconds. The experiments described here indicate that iodized starch gel slowly releases coated springs in water at 37 °C. It is known that the starch-iodine complex is stable up to temperatures of 40 °C [88]. With water temperature approaching this value, iodine appears to slowly diffuse outside the starch gel. During that process the springs deployed most. The cleavage of the starch-iodine complex and the diffusion of iodine might be occurring on a time-scale slow enough to sufficiently delay the swelling of starch. This might also help to explain why the springs did only deploy by a small fraction in water around room temperature. There the starch-iodine complex did not destabilize sufficiently. In water at 70 °C breaking and diffusion might have occurred quickly.

Air-heated starch gel

The experiments indicated that swelling of starch could be modified by heating dried starch gel after coating. Temperature exposure can be a side-effect of processing after application of starch gel or heat sterilization for implantation, or done on purpose as a means of achieving a desired

127

property. The changes in swelling behavior might be caused by changes to the structure of the starch gel. Three characteristic responses of starch gel to hot air exposure and their temperature range are listed in Table 9. The swelling behavior does not change much if the starch gel is heated to 100 °C, as long as the starch is iodized after this step. Exposure to this temperature might break or weaken some of the physical bonds formed during retrogradation of the gel. After the temperature exposure, swelling in water and dehydration might form new bonds, restoring the gel strength to a level similar is was at before.

Temperatures around 160°C might break a large portion of the physical bonds of the gel, and leave it less well connected. In these samples, there is no subsequent exposure to water before the actual swelling step that could allow new bonds to form. In that state, the gel releases the springs more quickly and also dissolves almost completely within a few minutes after immersion in water.

In contrast to that, exposure to air temperatures of around 200 °C, additional chemical bonds might form in the gel. These prevent the starch from swelling. In that form, starch can serve as stiff glue that permanently compresses or folds the substrate into a desired shape. Table 9 summarizes these explanations and mentions possible use of these characteristics.

Table 9: Three characteristic responses of starch gel to hot air exposure, and their temperature range.

Possible effect on gel bonds	*Minor damage (phys. bonds), mostly repaired during dehydration after iodizing*	*Major damage (phys. bonds), no repair, separated starch chains become soluble*	*New chemical bonds formed*
Air temperature	100 °C 160 °C 200 °C		
Spring deploying	*Slowly & gradually*	*Instantaneously, starch became soluble*	*No deploying observed*
Possible use	*Process compatibility, heat-sterilization*	*One-time quick release and disappear*	*Permanent folding*

3.7   Conclusions

Starch gel was investigated for properties useful for actuating micromechanical structures. As an exemplary structure neural probes with spring-deployed electrodes were used. Three spring designs were used. They had 120, 160 or 200 µm travel. All springs were 5 µm wide and 12 µm thick.

Starch gel coated to micrometer-thin layers was able to retract springs with 160 µm travel as it dehydrated by approximately 140 µm. At this deflection, the springs collectively reacted with 1.2 mN, according to an analytical model.

When immersed into water at 37 °C, the starch gel swelled but did not dissolve. The springs deployed within seconds. If the starch gel was iodized before immersion, the deployment became strongly dependent on the water temperature. The springs deployed slowly and gradually within several tens of minutes after an initial jump (40-60 µm). At 21 °C, the springs only deployed partially (40 µm) and then stalled. At 70 °C, the springs deployed instantaneously and almost completely. Since 37 °C is close to many mammalian body temperatures, this could be a useful characteristic.

In another set of investigations, the hydrogel was exposed to hot hair. The starch gel, after coating and dehydration, was exposed to 100 °C for 10 min without changing properties related to deploying springs much. Exposure to 160 °C rendered the starch gel such that it dissolves almost instantaneously in water. Exposure to 200 °C prevented the springs from deploying at all. This might be useful to permanently fold structures.

Furthermore, several methods of applying and patterning starch were investigated. Starch was applied by painting, dip-coating and spin-coating. Starch gel was etched in oxygen plasma. An etch mask was formed out of Kapton foil. Starch was stripped in boiling water, HCl (20%) and α-amylase (with residues). Hydrophobic coatings like Cytop were used to prevent starch from wicking into undesired areas. These results indicate that starch gel is compatible with methods typically used in micromachining.

In summary, the experiments indicate that starch gel has enabling properties for micro-mechanical applications. It can serve as non-electrically triggered one-time actuator providing large travel and force. Starch is easy to acquire and process, and it can be patterned with methods commonly used in microfabrication.

CHAPTER 4

PARYLENE NEURAL PROBES
WITH ENGINEERED STIFFNESS AND SHAPE
FOR IMPROVED INSERTION

This thesis chapter a fabrication technology developed to improve the insertion of Parylene neural probes into cortical tissue by implementing vertical stiffeners with a small footprint, and probe shanks with sharp tips. Taking advantage of the benefits of using a polymer as structural material for neural probes is often prevented by their troublesome insertion due to hyper-flexible shanks and dull tips. The fabrication process described here addresses both of these issues by integrating vertical stiffeners into the shank of Parylene neural probes, and by sharpening the probe tip by thinning its outer edge. Both modifications are achieved by minor adjustments to standard Parylene probe fabrication. According to an analytical model, these allow reducing insertion footprint for a given required stiffness, and are hypothesized to reduce the load on the shank and the dimpling of the brain surface during insertion. Several 30-µm-deep and 10-20-µm-narrow stiffeners are integrated into electrically-functional, 2-mm-long, 20-µm-thick, and 250-µm-wide Parylene neural probes. These were fabricated in a process requiring only three lithographic masks. The probes are strong enough for insertion into cadaver lamb brain through the pia mater. They are tested for electrical functionality by measuring the electrical impedance of the electrodes in saline

solution. Similar vertical stiffeners can be also used as hinges for folding structures, or wells for drug delivery.

4.1　　　Introduction

This paper reports a fabrication technology to improve the insertion of Parylene neural probes into cortical tissue by implementing vertical stiffeners and sharp shank tips (Figure 1). Neural probes are small, needle-like shanks that are implanted into the cortex in order to interface with neurons. They are used in zoological experiments in neuroscience [14] and for neuroprosthetics in clinical applications [89]. They can be fabricated using a variety of materials. Traditionally, hard and in some cases brittle materials have been used such as metal wires [90], silicon [1] or diamond [91]. More recently, flexible polymers like Parylene [92, 93], polyimide [94], SU-8 [95], liquid crystal polymer [96] or silicone [97] have been used. Polymeric materials are especially attractive for chronic implantation. They have advantages in material properties and fabrication: unlike their counterparts made of silicon, they are flexible and unlikely to break, they can be fabricated alongside and seamlessly integrated with cables, and they are pliable so they can be deformed during implantation to match biological topography.
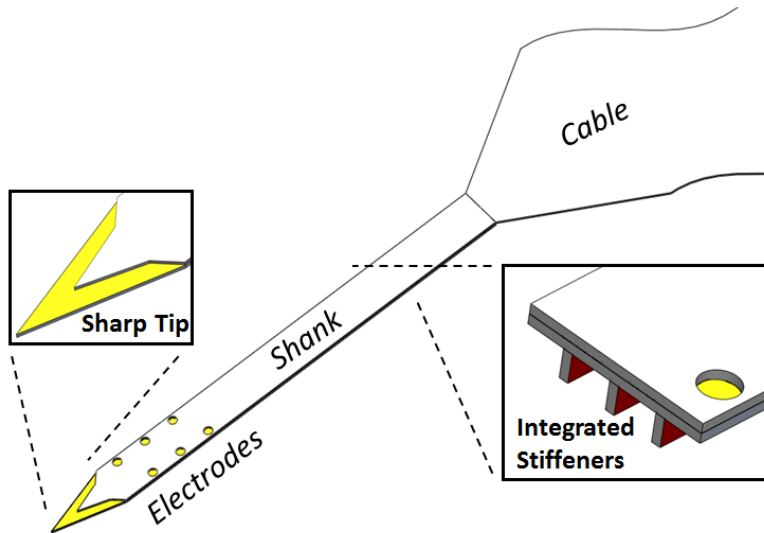
Figure 75: 3D drawing showing three different profiles of the Parylene neural probe: the sharp edge around the tip, the stiffeners underneath the shank and the flexible cable.

Flexible neural probes have been fabricated using various polymers. Often Parylene is the preferred material due to its unique properties: it can be deposited conformally, pure and void-free using vapor deposition on a substrate kept at room temperature [98], it is chemically and biologically inert and it has a long history of use as implant material [99]. Furthermore, Parylene layers can be bonded together to form fluid channels on neural probes [100]. A simple way to increase the buckling load of polymer probe shanks is to increase their thickness. However, unlike polymers that can be spin-coated to thicknesses in excess of 20 μm and photo-structured [94], the thickness of Parylene layers that can be practically achieved is limited to a few tens of micrometers. One of the main reason is that etch masks used to patterning Parylene quickly erode or form composite layers that do not etch. Hence there is need for more sophisticated ways of stiffening polymer probes, especially those made of Parylene.

Several ways to stiffen flexible polymer probes have been published. Some examples are depicted in Table 1. These can be grouped into three approaches. Approach 1 is to integrate a stiffer material, such as silicon or metal, into critical parts of the probe [101]. This allows reduction of the cross-section of the polymer shank without sacrificing stability. However, it also compromises some of the advantageous material properties of polymers. Approach 2 is to temporarily stiffen the probe shank for insertion. A stiff shank facilitates insertion into tissue; a more flexible shank likely mitigates stress induced into tissue by micromotion occurring inside the brain. This has been achieved in at least in two ways. For example, by coating bio-dissolvable materials onto a flexible polymer shank [102, 31, 73]. After insertion, they soften and dissolve, and the only flexible part of the shank remains. Although this is a very promising principle, there still are major hurdles to be overcome. Many bio-dissolvable materials are extremely soft before insertion and tend to soften further during insertion. Hence they were made large in order to increase the probe stiffness sufficiently. This can lead to dull tips, large probe dimensions, restrictions on insertion methods, and degraded electrode performance. Another way to temporarily stiffen the shank is to use a retractable insertion shuttle [97, 103]. In principle, the shuttle consists of a stiff carrier that is reversibly attached to a flexible shank. Both are inserted together. Shortly after insertion, the carrier is retracted, leaving the flexible shank behind. However, system assembly can be complex. The flexible shank needs to be well aligned to the carrier. This might be even harder when using combs or arrays of neural probe shanks. Also, it is not trivial to secure the probe to the carrier and to detach it after insertion. Approach 3 is to form a strategic shank design. For example, curving planar-fabricated polymer probes widthwise increases the moment of inertia without altering the footprint of the probe shank. A curved shank geometry is realized by thermal annealing in a custom-made mold after fabrication [104].

This thesis chapter reports a technology to stiffen Parylene neural probes by integration of narrow and deep vertical stiffeners. This does not add much process complexity and allows reducing the shank footprint. The stiffeners are made by trench refill. Trench refill has been developed to make high aspect-ratio polysilicon structures in silicon [105]: Deep and narrow trenches can be etched into silicon and refilled with silicon dioxide/polysilicon to form large conductive surfaces with narrow gaps for capacitive transducers. Similar trench refill has been used to form thin and high vertical beams of polysilicon for microprobes [106]. Parylene refill of silicon trenches (formed by deep reactive ion etching) has been used for high-aspect ratio structures for accelerometers [107]. Here, a new method to integrate vertical Parylene stiffeners into the shank of Parylene neural probes using refill of photoresist trenches is reported.

Table 10: Compared to other methods, integrating vertical stiffeners into shanks strongly increases the inertia without increasing the thickness of the shank or the process complexity much.

Ref.	Shank Footprint Geometry	Inertia per Footprint	Ease of Fabrication	Integration in Arrays
Reference				
[93]	Rectangular	-	Requires large thickness	Easy
Approach 1: Permanent integration of a stiffer material				
[101]	Integrate Hard Material	+ +	Reasonable	Easy
Approach 2: Temporary stiffening of the shank				
[102, 31, 73]	Coated Dissolvables	- -	Individual assembly	Hard
[97, 103]	Insertion Shuttle	+	Individual assembly	Hard
Approach 3: Strategic shank design for increased stiffness				
[104]	Curved Widthwise	+ +	Individual processing	Hard
This Work	Vertical Stiffeners	+	Easy	Easy

A new method to fabricate sharp tips of Parylene probes is also presented here. Sharp tips are shown to reduce the load on the shank during insertion. Sharp tips also induce less dimpling of the brain surface during insertion [108], what likely mitigates tissue damage. Typically, polymers cannot be machined as precisely as silicon. Shanks made of polymers need to be thicker, which leads to duller tips. To work around this constraint, others have patterned silk to a sharp tip inside a mold [73], or have integrated sharp silicon tips into an array of Parylene probes [109]. Both

require manual assembly and integration of hard materials into the polymeric probe. Here an integrated method to create a thinner and sharper tip in Parylene probes is introduced.

4.2 Materials and Methods

Design and Analysis

A neural probe needs to be designed large enough to provide sufficient stiffness for reliable insertion and electrical insulation. Minimizing shank dimensions decreases tissue damage and allows for a more narrow pitch between adjacently implanted shanks. The length, width and thickness of stiffeners and shank need to be chosen. The width of the probe is typically set to be as narrow as possible, meeting the required width for electrical interconnects. The thickness of Parylene cannot be increased arbitrarily; very thick layers (in excess of 20 μm) require long deposition times and are troublesome to etch. Too thin layers do not insulate well and are too flimsy for insertion and handling. Stiffeners add material in strategic positions away from the neutral plane of the shank. This considerably increases the bending moment of inertia. For a given minimum buckling load of the shank, stiffeners allow reducing its volume (compared to a shank with a rectangular cross section). The length of the probe is typically dictated by the physiological depth of the desired neurons. For example, electrodes placed 2 mm below the surface of the brain allow the detection of the highest number of discernable spikes in the macaque motor cortex. Probes that are only 1.5 mm long do not reach layer V neurons, which are preferable for extracellular recording [110].

The following analysis of buckling loads of neural probes with integrated stiffeners illustrates the feasibility of increasing the buckling load and provides a design guide. The model is based on concepts derived in [47]. The minimum axial load on a shank that causes buckling can be

approximated by Euler's formula for beam buckling:

$$F_E = c \cdot \frac{E \cdot I_{min}}{L^2}$$

(15)

F_E is the maximum longitudinal load on the shank that does not make it buckle, c is a factor taking mechanical boundary conditions into account, E is the Young's modulus of the shank material, L is the length of the shank and I_{min} is the bending moment of inertia across the axis of buckling. This analytical model is based on concepts derived in [47]. The bending moment of inertia of a section of the probe shank is calculated in two steps:

- The bending moment of inertia of rectangular segments of the shank (shank, stiffener, metal trace) around their own neutral axis is calculated.
- The bending moments of these segments are then combined using the Transfer Formula [47] to calculate the bending moment of the composite shank.

The bending moment of inertia of rectangular sections around their own neutral axis is:

$$I = \frac{width \cdot height^3}{12}$$

(16)

The Transfer Formula states that the inertia of the compound shape (I_C) calculates from that of the segments (I_i) as follows:

$$I_C = \sum_i I_i + \sum_i A_i \cdot d_i$$

(17)

with A_i the area of segment i and d_i the distance of the neutral axis of segment i to the neutral axis of the compound shape. The position of the neutral axis of the compound shape is its center of gravity and calculated with respect to a reference axis. This axis is chosen to be located at the

139

bottom of the stiffeners. The position of the neutral axis with respect to that reference is:

$$d_{reference} = \frac{\sum_i A_i \cdot r_i}{\sum_i A_i}$$

(18)

with r_i being the distance of the neutral axis of segment i to the bottom of the stiffeners.

To give a practical example, this analysis is performed for a shank with length of 2 mm and a width of 100 μm. The Young's modulus for Parylene was measured to be 4.75 GPa [111]. The variable 'c' is approximated to 20.2 for a fixed-hinged mechanical boundary condition of the probe shank [47]. Note that the lateral location and distribution of the stiffeners underneath the shank does not influence the bending moment of inertia in this simplified model. Their contribution can be determined according to their cumulative width.

Table 2 illustrates the effect of different numbers of 10 μm- wide stiffeners (the effect of metal interconnects is not included in this analysis). Typical maximum insertion forces of neural probes have been reported to be around 5 mN [112] (this value changes with a variety of factors such as insertion speed and tissue preparation).

Table 11: Adding stiffeners to shanks allows increasing their length or reducing their volume while maintaining their buckling load. This analysis does not take the effect of metal interconnects into account.

	Geometry: 20 µm shank thickness, 30 µm height of stiffener, 10 µm width of stiffener, 100 µm shank width, 2 mm shank length, 4.75 GPa Young's modulus [111].

Standard	**One stiffener (10µm width)**	**Four 10 µm-wide stiffeners (40µm cumulative width)**
Bending Moment of Inertia		
$6.7 \cdot 10^{-20}$ m^4	*$2.5 \cdot 10^{-19}$ m^4*	*$6.3 \cdot 10^{-19}$ m*
Euler buckling load for one end of the shank fixed and the other one pinned.		
1.6 mN	6 mN	15 mN
Approximate length of this shank compared to length of a shank with quadratic cross section and equal buckling load		
100%	200%	300%
Thickness of a shank with rectangular cross section and the same buckling load as this shank		
20 µm	32 µm	42 µm
Ratio of volume between shank with stiffener and shank with rectangular cross section and with increased thickness to match bending moment		
100%	72%	*76%*

Figure 76 shows a plot of the modeled buckling load as a function of width and thickness of

stiffeners. The graph shows that the buckling load of the shank can be increased from 1.6 mN to

12.5 mN by integrating one stiffener, with 30 µm width and 30 µm thickness.
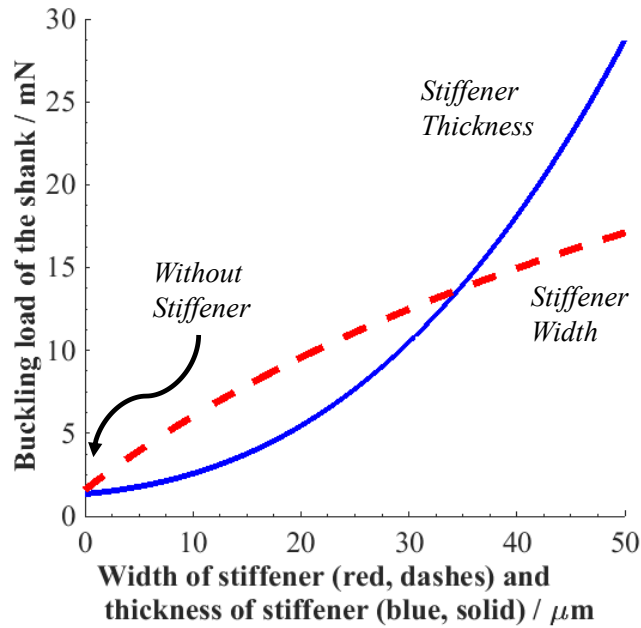
Figure 76: Adding stiffeners with 30 μm cumulative width and 30 μm height increases the buckling load of a shank from 1.6 mN to 12.5 mN, according to this analytical model. The dashed line shows how the buckling load of a 100 μm wide and 2 mm long shank changes with the width of a stiffener with 30 μm thickness. The solid line shows how it changes with the thickness of a stiffener with 30 μm width.

The metal layer used for electrical interconnects can also have an influence on the buckling load of the shank, especially when stiffeners are present. The reason for that is, once stiffeners are implemented, the location of the relatively stiff metal layers can be further away from the neutral plane of the shank. Following analysis describes how large that influence is, and how it depends on vertical position and thickness of the metal layer. The shank geometry and mechanical boundary conditions are set as before. A 50 μm wide metal trace is placed inside the upper part of the shank, accounting for the cumulative width of several traces. The Young's modulus of the metal forming interconnects was assumed to be 139.7 GPa, corresponding to thin film platinum [113]. As before,

142

the Young's modulus for Parylene was set to 4.75 GPa [111] Two scenarios are modeled. In one, the thickness of a metal trace placed in the neutral plane of the shank is swept from 0 to 5 μm. In the other, the vertical position of a 1 μm thick metal trace is swept from the lower end of the shank (30 μm height) to the upper end of the shank (50 μm height) of the shank, above a 30 μm high and 20 μm wide stiffener.

To calculate the effect of the metal trace on the buckling load, equation (1) is used. The probe shank consisting of different materials (Parylene, Platinum) is modeled by a shank consisting of one material only (Parylene). This is done by weighting the width of parts consisting of Platinum with the ratio of the Young's moduli of Platinum and Parylene. The ratio of the Young's moduli of Platinum and Parylene is 29.41. The width of the metal trace is 50 μm, the weighted width becomes 1471 μm.

The analysis shows that the buckling load does not change much when the metal trace is centered in the neutral plane of the shank, even if the thickness of the metal is increased considerably. However, the buckling load increases by more than 50 % if a 1 μm thin metal trace is placed close to the upper end of the shank (Figure 77).
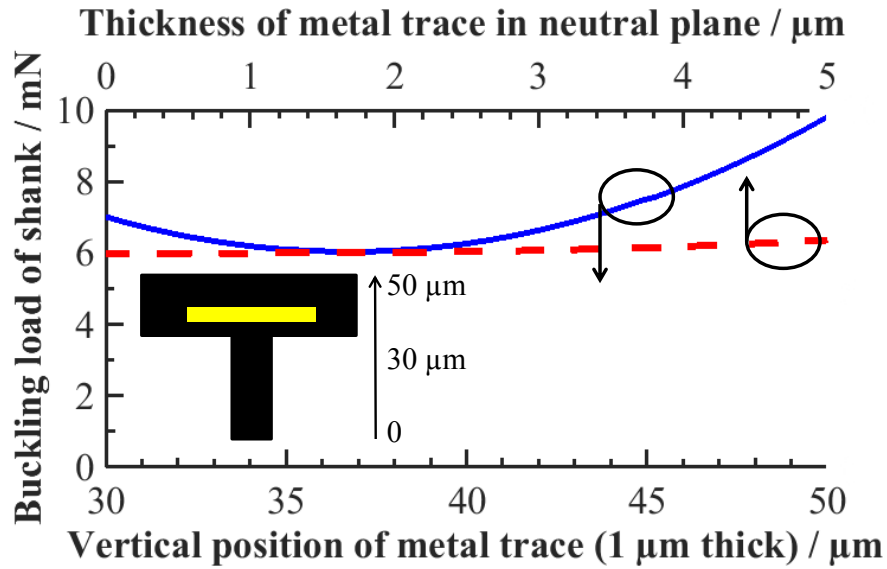
Figure 77: Analytically modeled buckling load of a shank as a function of the thickness of a metal trace in the neutral plane (dashed line, top x-axis) and as a function of vertical position of a 1 μm thick metal trace (solid line, lower x-axis).

This strong increase in buckling load is caused by the relatively stiff metal being further away from the neutral plane of the shank which amplifies the stress during buckling.

Another factor impacting the buckling load of the shank is the way the probe is anchored during insertion. The effect of mechanical clamping of the shank is represented by 'c' in equation (1). It can be approximated by 20.2 for one end of the shank fixed, and one end hinged. For both ends hinged, its value drops to 9.8 [47]. This example shows that a secure support for the backend of the probe (providing a fixed rather than a hinged boundary condition) could double the buckling load. One design consideration drawn from this observation is that the stiffeners should extend underneath the area where the probe is clamped during insertion.

144

Being very well established, this beam buckling analysis was not experimentally verified in this report.

Furthermore, a method to create sharp tips in Parylene probes is introduced. To pierce the surface of the brain, a certain pressure is required [114]. The pressure the probe exerts on the surface of the brain during implantation corresponds to the load on the shank distributed across the area of the tip in contact with the tissue. This area is proportional to the thickness of the probe tip. Here, the top Parylene layer around the tip is removed. This roughly doubles the pressure the probe exerts on the surface of the tissue. Besides lowering the load on the shank during insertion, sharper tips also lower the amount of dimpling of the surface of the brain [112].

<u>Fabrication</u>

Probes were fabricated in pairs of two or three identical shanks connected by one common backend for handling during transport and implantation, and one Parylene cable. Probe shanks were fabricated with three different widths and two different lengths. The widths were set to be 180 μm, 300 μm, or 380 μm, and the lengths were either 2 mm or 3 mm.

The main fabrication steps are depicted in Figure 78. The process requires three lithographic masks.

a) Pattern thick photoresist, deposit Parylene.

b) Evaporate Ti/Au/Ti.

c) Deposit Parylene.

d) Pattern Parylene.

e) Release in acetone.

Parylene	Silicon
Resist	Metal
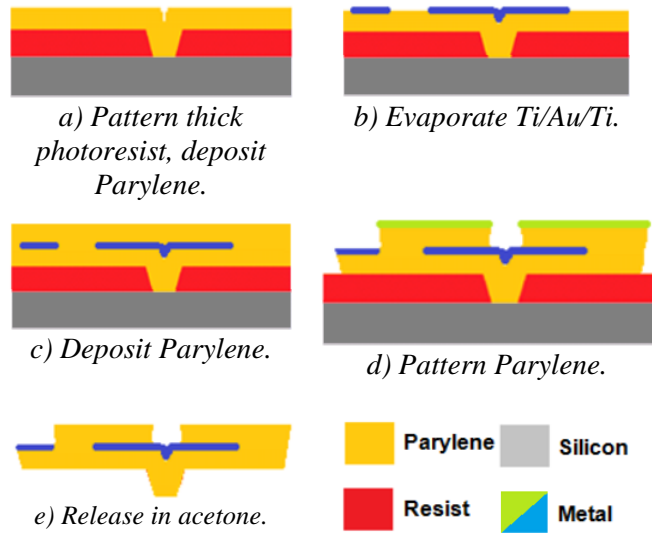
Figure 78 : Fabrication steps of Parylene probes with integrated stiffeners and sharp tip edges.

A silicon carrier wafer is used. After HMDS priming, two layers of photoresist AZ9260 are spun sequentially for 2 s at 300 rpm to produce a 25-30 µm-thick layer (depending on the distance to the center). The thickness of the stiffeners is defined by the thickness of this photoresist. Its thickness is controlled by the amount of resist dispensed on the wafer, and the duration and speed of spinning. The resist is exposed for 160 s on an MA/BA-6 Mask/Bond Aligner, (Süss Microtech, Garching, Germany) with 30 mW/cm^2, and developed in AZ400k/DI = 1:4 for 2 min. It is important to minimize outgassing from the thick resist during further process steps. For that, an intermediate and a final softbake step on a hotplate for 5 min at 90 ℃ are performed after spin coating. Then the wafer is flood-exposed and stored in vacuum for two hours. The trenches are refilled with a 12.5 µm-thick Parylene layer using a PDS2035 (Specialty Coating Systems, Indianapolis, USA) (Figure 78a). The photoresist is protected by Parylene during further fabrication. A metal layer to form interconnects, electrodes, pads and an etch-stop, consisting of Ti/Au/Ti or Ti/Pt/Ti 800/3000/800 Å, is evaporated. To pattern it, lift-off using 2-µm-thick SPR220 resist is used (Figure 78b). A second Parylene layer with 16 µm thickness is deposited.

Finally, the Parylene is etched in oxygen plasma. An etch mask consisting of Ti/Al 2000/3000 Å is evaporated and patterned via lift-off (Figure 78d). The tip is sharpened in this step, using a simple design change. The outline of the shank of the probe, and the inner portion of the tip are defined by etching Parylene through a metal etch mask. The metal layer sandwiched between the two Parylene layers, which forms interconnects and electrodes, is used as an etch stop around the outer potion of the tip. This allows creation of a recess, rendering the tip thin and sharp. The probes are released in acetone by dissolving the photoresist. A gentle method of releasing the probes off the carrier is advantageous, because, in order to achieve a high buckling load it is critical that the probes remain straight.

One fabrication challenge is that the deposition rate of Parylene is lower at the bottom of trenches. This can lead to the trenches sealing off at the top during Parylene deposition, before the trench is completely refilled. This would leave a permanent void in the center, what is detrimental to the mechanical stability and might cause biological complications after implantation. Also, as trenches refill, a notch forms in between them (Figure 78b). It is important that this notch does not hinder continuous metal deposition for interconnect formation. The authors of [107] addressed these problems by repeatedly etching and depositing Parylene. Here, trenches with a slight outward slope are created. This was done by calibrating exposure dose and developing time. The sloped sidewalls can be completely refilled with Parylene and form a less pronounced notch. The depth of the notch decreases as the Parylene layer thickness increases. As a rule of thumb, if the photoresist sidewall has a slight slope, the thickness of the Parylene layer should be 1.5 times the maximum width of the trench.

4.3   Results

Fabricated Probes

147

Released probes can be seen in Figure 79. The images show the top and bottom sides of the neural probes.
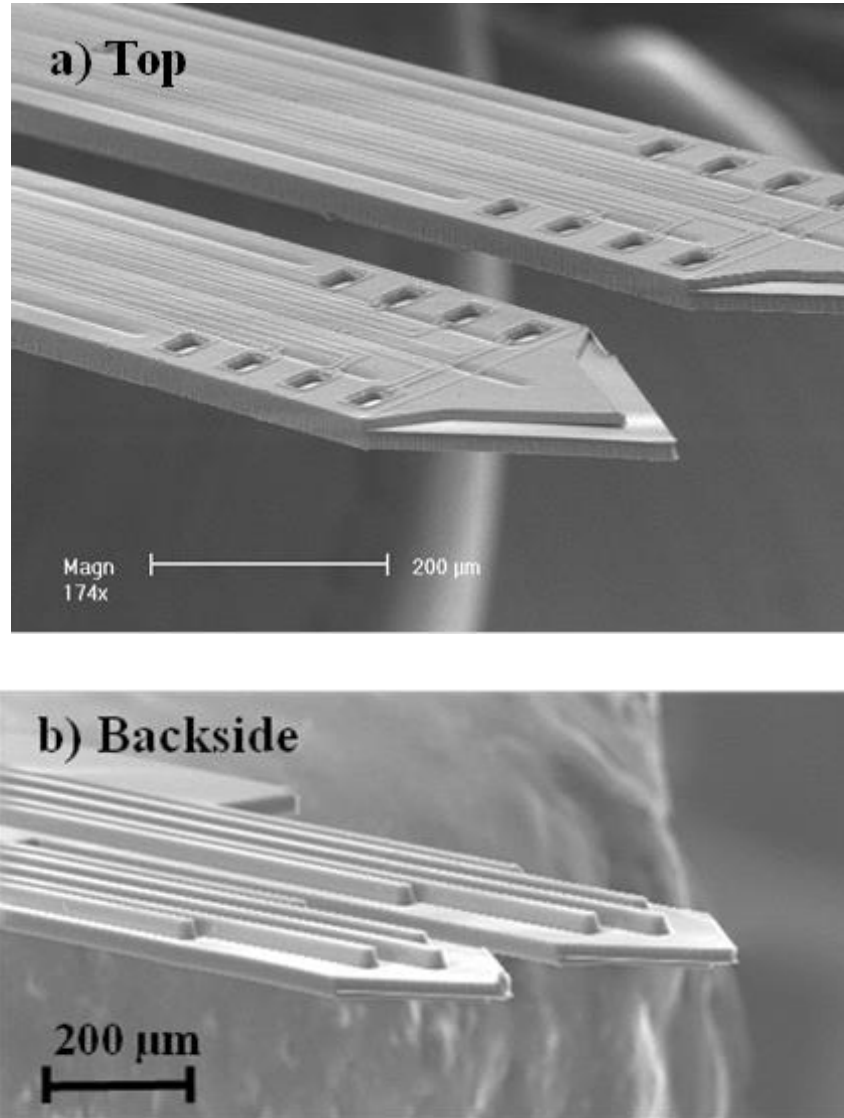
Figure 79: a) top of the probe showing electrodes and sharp tip edges, b) backside of a probe with 5 stiffeners.

An image of the cross-section of a refilled photoresist trench is shown in Figure 79. The slope of the sidewalls of the trenches was measured to be 78 deg. The photoresist trenches were completely

refilled and void-free. Figure 80 shows metal traces deposited across the notches above the stiffeners.
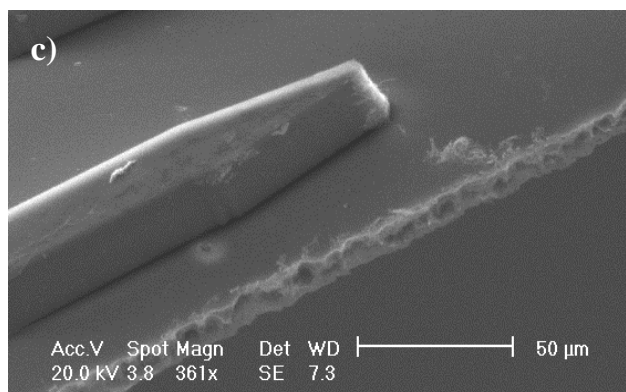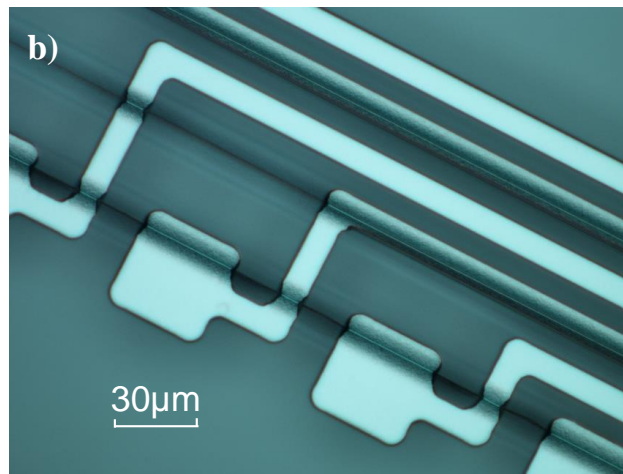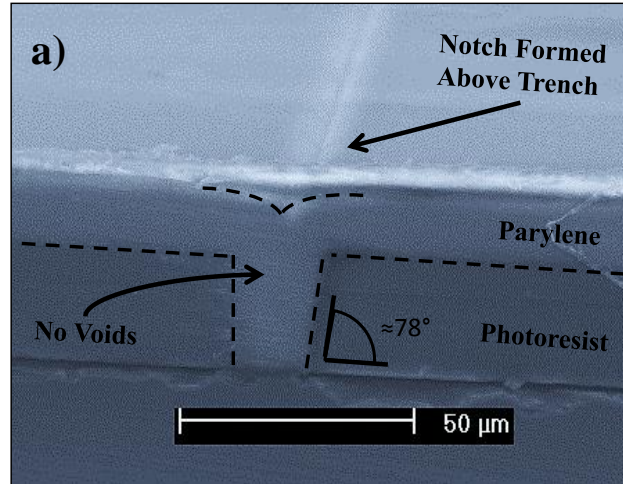
Figure 80: a) Photoresist trench refilled with Parylene; b) interconnects and electrodes deposited across the notch formed above trenches and c) chamfered tip of a stiffener.

The probe shanks were evaluated in insertion tests, and the impedance of their electrodes was measured in a saline solution. All probe designs could be inserted manually into 0.6% agar brain surrogate and into a cadaver lamb brain when the pia was nicked (the probes were inserted through an opening in the pia). Probes with 380 μm width, 2 mm length, and five integrated stiffeners could be inserted into a cadaver lamb brain through the pia (Figure 81).
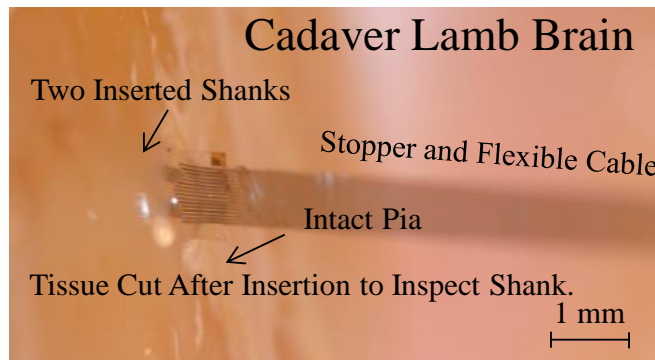
Figure 81: The probes with stiffeners inserted through the pia into a cadaver lamb brain.

To contact the electrodes, the probes were connected to OMNETIC connectors on PCBs using rivet bonding [115]. The electrode impedance was measured in 0.9% saline solution using a large platinum counter electrode. The solution and interconnects had relatively small resistance (less than 100 Ω), much less than the electrode impedance. Table 12 summarizes the results.

Table 12: Summary of mechanical, and electrical properties of fabricated probes.

Geometry		
Three designs: Shallow/Medium/Robust		
Shank Width	180/300/380 μm	
Shank Length	3/3/2 mm	
Total Thickness	55 μm including stiffeners 25 μm without stiffeners	
Width of Stiffeners	5–10 μm	
Number of Stiffeners	3/3/5	
Mechanical Properties		
Successful Insertion Experiments	all: agar gel brain model, cadaver lamb brain with pia nicked. "Wide" design: insertion w. pia intact.	
Electrical Properties		
(measured in 0.9% saline @ 1 kHz, site area: 900 μm^2)		
Gold electrodes: Zavg./Phase	1.5 MΩ/−75°	
Plat. electrodes: Zavg./Phase	350 kΩ/−65°	

4.4　　Discussion

The technology introduced here allows the creation of stiff, sharp and flexible regions that can be distributed along the probe shank, cable and connector. Since the tip, shank and cable have different requirements for cross section and stiffness, the use of stiffeners provides a very useful design "knob." The tip needs to be thin and shallow to easily pierce tissue, the shank needs to be stiff enough for insertion and have a small size, and the cable needs to be flexible (Figure 82).
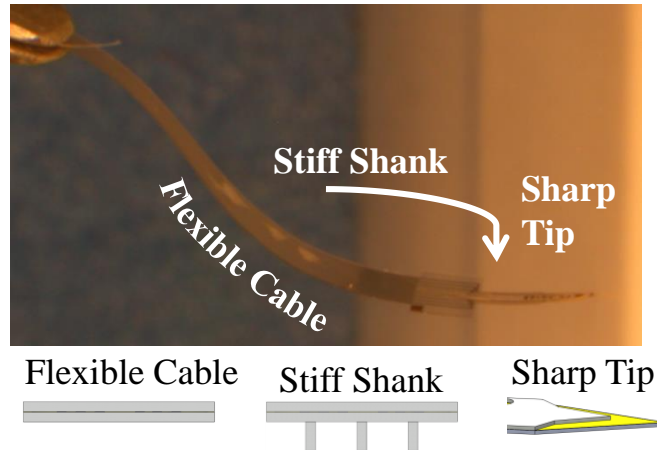
Figure 82: Micrograph of a Parylene probe pressed against a surface. The probe has three different cross sections along its length (illustrate above), allowing for sharp tips, stiff shanks and flexible cables.

The introduced modifications to conventional fabrication do not require manual assembly, non-standard materials and are scalable to arrays of probes.

The following paragraphs discuss some considerations of how the presence of stiffeners might affect the tissue reaction around chronically implanted neural probes, and their chronic stability.

Clinical applications of neural probes, related to prosthetics, require them to function over extended periods of time. However, the signal quality of chronically implanted neural probes is known to decrease over time [22, 10]. It was found that a chronic inflammation around the shanks of neural probes forms with increased density of immune cells and decreased density of neurons [115]. The further away a neuron is from an electrode, the lower the amplitude of the recorded signal [24]. Furthermore, some components of the immune reaction can contribute to an increased electrical impedance of the tissue surrounding neural probes. This also can decrease the amplitude of recorded signals and contribute noise [116].

153

The extent of the chronic tissue reaction around implanted neural probes has been shown to depend on the size of the implant [33]. Probe shanks with rectangular cross section and those with stiffeners and equivalent bending moment of inertia, will likely cause similar extend of scarring and tissue damage. Although the stiffeners allow reducing the cross-section, the right angles between stiffeners and shank are not likely to foster tissue survival or ingrowth in that area. The main advantage of integrating stiffeners lie in an easy method of rendering Parylene neural probes stiff enough for unaided insertion. Nontraditional shanks that employ means of reducing the size of the indwelling part of the shank (e.g. with biodissolvable materials [31, 73] or retractable insertion shuttles [97, 103]), allow for extremely small shank sizes. Some of the published examples show great promise but currently still face major practical limitations (extended tissue damage during insertion due to large insertion footprint and reduced sharpness of the tips, foreign body response to the biodissolvable materials, and dependence on an extremely fast insertion).

The flexibility of the anchor of implanted neural probes has also been shown to modulate the tissue response [33]. In case of neural probes are anchored to the skull, when the brain moves inside the skull, tethering stress is induced in the tissue. Flexible anchors are likely to decrease this stress. The stiffeners can be integrated selectively only under the shank and leave a very flexible cable connecting the back of the probe. Hence the stiffeners do not necessarily influence the stiffness of the anchoring.

Another component of micromotion originates from within the brain and is caused by pulse and respiration [117]. Similar to anchoring to the skull, this can also induce stress in the tissue. However, brain tissue is more than two orders of magnitude softer than Parylene [60]. This suggests that the increase in structural stiffness in one dimension due to the integration of stiffeners

might only cause a small increase in the induced stress in response to micro motion originating from within the brain.

The vertical stiffeners can also serve other purposes in neural probes. It may be desirable to transport drugs or cells into the brain [92]. Stiffeners can form a series of freely distributed wells or closed channels, allowing the secure transport of their content during implantation. Additionally, there have been some efforts to fold planar fabricated polymer probes into three dimensional probe arrays [92]. To achieve this, several connected shanks were fabricated in plane and then bent out of plane. Stiffeners like those described here can form hinges creating a preferred line for bending (Figure 83).
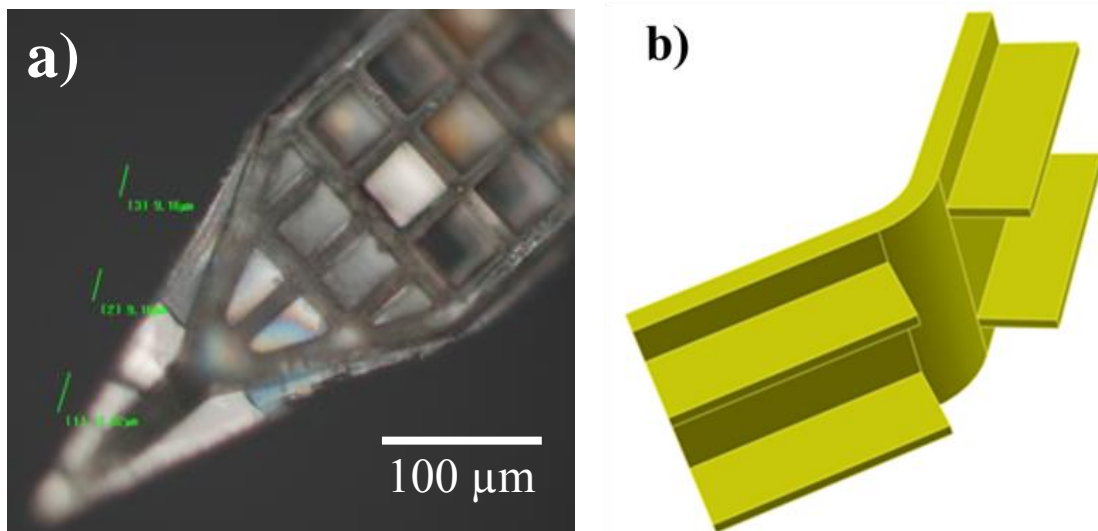
Figure 83: The developed process can also form (a, micrograph) shanks with wells e.g., for drug delivery or (b, 3-D drawing) hinges e.g., for bendable probe arrays.

4.5   Conclusions

This thesis chapter explains the design, analysis and fabrication of Parylene neural probes with integrated vertical stiffness and sharp tips. Both features are meant to improve the insertion of the

probe shanks into tissue. The mechanical and electrical practicality of the developed probes was experimentally verified.

A theoretical model revealed design choices that can have a large effect on the buckling load of the probe shank:

- The formation of a vertical stiffener underneath a Parylene shank can, employing typical dimensions, increase its buckling load from 1.6 mN to 6 mN.

- The buckling load can be further increased from 6 mN (Parylene shanks with metal interconnects and stiffeners) to more than 9 mN by depositing interconnect metal away from the mechanical neutral bending plane of the probe and close to the top.

- Anchoring the backend of the probe (providing a mechanically fixed rather than a hinged support) is doubling the buckling load.

Taken together, these modifications were shown to be sufficient to design electrically functional neural probes capable of insertion into cadaver brain.

The stiffener fabrication technique can also form open wells, channels or hinges integrated into the shank of neural probes. The wells or channels can be used for drug delivery, while hinges can establish a preferred bending axis for folding structures.

CHAPTER 5

GENERAL CONCLUSION AND SUGGESTED FUTURE WORK

This thesis presents a new class of intracortical neural probes with small electrodes that self-deploy from the large after insertion, which is hypothesized to prolong their chronic function. For that purpose, an actuation mechanism based on starch- hydrogel coated springs was developed. This concept may be used to form chronically stable brain-machine interfaces for clinical applications. Beyond that, properties of this starch-hydrogel actuation mechanism were explored for more general applications in MEMS. Furthermore, a Parylene neural probe design for improved insertion is elaborated. The thesis contributions can be concluded as follows:

- Neural probes with post-implant, self-deploying electrodes

An implantable, one-time compression and release actuation mechanism was developed and integrated in shanks of neural probes. The actuator consists of silicon microsprings that are retracted and released by a biodegradable, starch-based hydrogel coating. The deploying springs drive electrodes away from the shank after its insertion into tissue, triggered by contact of the dehydrated gel with biological fluids and body temperature.

Six electrodes on silicon neural probe shanks that were 3 mm long, 12 µm thin and 290 µm wide were shown to deploy by more than 120 µm through an agar brain model. This is, according to published studies, sufficient to reach beyond the dense scar tissue depleted of neurons, which is

accumulating around the shank over time and thus hypothesized to enhance the chronic operation. A specialized spring design was developed to have surfaces of spring arms coming into contact during deflection. This was implemented in order to facilitate coating and actuation by hydrogels. The springs were designed to have an extremely compact geometry when retracted, minimizing the increase in width of the neural probe shank. The springs were coated with iodized starch gel, which almost completely retracted them during dehydration. The springs slowly released (after an initial "jump") after insertion into an agar brain model. To delay the onset of the deployment until after the insertion of the neural probe shank, a second coating consisting of poly(lactic-*co*-glycolic-acid) was applied. With that, the onset of the deployment was delayed by 20 s. This delay is likely sufficient for insertion of a neural probes into cortical tissue under typical circumstances. The starch-coated springs then deployed within three minutes by 100 μm, and additional 20 μm over the next two hours. A set of experiments, including an acute *in-vivo* study, indicated that the fabricated devices are practical to use, and are able to record signals from neurons.

- Starch hydrogel for actuation of MEMS

Starch-based hydrogels were further investigated for actuation of structures on the micro-scale. Starch gels showed a diverse set of properties that could be harnessed for temperature-dependent self-actuation (triggered by the presence of water), such as retraction, compression, release, expansion or permanent folding.

Micrometer-thin layers of starch-hydrogel were shown to strongly compress silicon springs, used as exemplary devices. Coated springs with 12 μm thickness, 5 μm width and 160 μm travel were retracted by more than 140 μm during dehydration of the gel. At that deflection, they react with 1.2 mN, according to an analytical model.

Pure starch gel released the springs almost instantaneously after coming into contact with water. Iodized starch gel slowly (on the order of several tens of minutes) released the springs in water at 37 °C. The speed of deployment was strongly dependent on the temperature of the water. At room temperature, the springs only released partially but then stalled. Exposing starch gel to hot air (200 °C for 2 min) prevented coated springs from deploying in water. This property could be used to permanently fold structures. Starch hydrogels were found to be compatible with patterning and coating procedures commonly used in microfabrication.

- Parylene neural probes with integrated stiffeners and sharp tips

Two technologies to improve the insertion of hyper-flexible Parylene neural probes into neural tissue were introduced. A fabrication process was developed to form shallow and deep vertical stiffeners underneath planar Parylene shanks. According to an analytical mode, the stiffeners considerably increase the buckling load of the shanks. These stiffeners could also be used to form wells for drug or cell delivery, or hinges for folding around a preferred axis. Furthermore, a method was developed to create a thin and sharp tip on Parylene shanks. This is hypothesized to lower the amount of dimpling of the brain surface and the load on the shank during insertion. Fabricated 2 mm long and 180 µm wide Parylene probes with stiffeners and sharpened tips could be inserted into cadaver lamb brain.

5.1 Suggested Future Work

There are several stages for the research to continue in: Evaluation of efficiency and efficacy in chronic animal experiments of the developed prototypes of neural probes with deploying electrodes, optimization of the developed designs, and translation of the developed technologies into other applications.

The driving motivation for the research conducted in this thesis was to provide technologies to extend the lifetime of implanted neural probes. Chronic studies could help to evaluate the developed technologies in two ways. They could test the hypothesis that deploying electrodes away from the shank increases the chronic stability of neural probes. Also, they could allow investigating how the developed technologies allowing to deploy electrodes behave during chronic implantation. This includes investigating the fate of starch and PLGA in the central nervous system.

The first studies should investigate if the developed probes are operating chronically and if not, what their failure mechanisms are. Studies investigating the chronic performance of neural probes are complex and their outcome often depends on multiple factors. Some aspects to consider are:

- Animal model: The community that has been focusing on investigating the chronic stability of neural probes is using rat as animal models. Comparably few published research involves chronic recording from large animals such as monkeys. This might have ethical and financial reasons. Larger animal models might provide more insight valuable for clinically applications since behavior, immune reaction and physiology are a closer match to humans. To gain first insight into the chronic performance of the developed neural probes, and to eliminate as many failure mechanisms as possible, rat models might be a good choice. This will also allow to benchmark the results with published work from the community.

- Anchoring of the neural probe: The way the neural probe remains anchored after implantation can have a critical impact on its chronic performance. An easy way of anchoring neural probes, often used when employing a small animal model, is to secure the probes to a firm substrate that is cemented to the skull. However, this can aggravate tissue damage since the probe will displace along with the skull. An alternative is to leave

160

the probe floating with the brain, connected by a flexible cable or not at all. This requires a back end with a very low-profile (fitting between the brain and the skull/cap), and flexible or wireless connections between the probe and the head stage. For smaller animals like rats, this is very challenging. For the first study, tethered probes might be the better option. Since the deployed electrodes might be able to compensate for some motion between the brain and the skull, this might enhance their performance compared to controls without deployed electrodes.

- Controls: Scientific studies often gain meaning by adding an experiment in order to observe the outcome if the method under investigation is not used. The performance of neural probes with deploying electrodes will likely depend on many circumstances, some of which cannot be controlled: the surgery for implantation, the behavior of the animal in between and during measurements, the choice of size, distribution and impedance of electrodes, and the means and methods used to evaluate their recording performance. Some meaningful control experiments in a chronic study could be: evaluating the performance of non-deploying electrodes that are formed on a shank and at the end of needles without springs, formed on a shank also holding deploying electrodes. Furthermore, shanks with similar dimensions and electrode distributions that do not carry any deploying electrodes could be implanted contralateral. The shanks without deploying electrodes should be, in some cases, coated in starch and PLGA in order to isolate their impact on the performance.

- A common duration of chronic experiments investigating the tissue response around neural probes is 12 weeks. In rats, the tissue response was shown to stabilize after that time. However, experiments lasting longer than that showed a continuous decrease in signal quality. This suggests the existence of failure mechanisms other than the formation of a

161

chronic scar. Initial experiments should be done with a duration of 12 weeks to allow comparing to published work, but follow-up experiments should extend beyond that. Deployed electrodes might alleviate failure mechanisms other than the formation of scar tissue, such as damage induced by micromotion.

- Collected data: The impedance between electrodes should be measured regularly, as this gives insight into several failure mechanisms including biofouling (deposition of biological films with high impedance) or lead breaking. The amplitude and frequency of recorded action potentials is a good measure since this is often the intended use of neural probes in brain-machine interface applications. However, electrodes could be able to pick up action potentials while accidentally not being close enough to neurons to do so. A measure for the ability of an electrode to pick up action potentials is the power of the recorded noise in the frequency band of action potentials. This might be especially relevant to the present laminar neural probe design, where some electrodes are likely placed closer to layers of larger neurons. Histology of brain slices after termination of the experiment will also provide useful data. The extent of the tissue reaction, indicated by the density of immune cells, can be directly quantified. It should be investigated how the presence of starch and PLGA, and the geometry of the probe shank, needles and springs modulate the formation of the scar tissue.

The most useful design optimizations for the developed neural probes with deployable electrodes will likely be to reduce the shank width. The shank width composes of a minimum width required for mechanical stability, the cumulative width of retracted springs, and the length of the needles. Vertical stiffeners underneath the shank [57] can reduce the width of the shank required for mechanical stiffness to probably tens of micrometers. Rearranging or redesigning the springs, for

162

example such that the whole shank behaves like a spring, will reduce their contribution to its width. If the needles are oriented along the length of the shank during implantation, only their width and not their length will contribute to the width of the shank. Once the shank is fully inserted, they could fold out and align perpendicular to the shank. Alternatively, similar to [97], the shank could be reinforced by a recoverable inserter, leaving only deployed electrodes and flexible electrical traces behind. The distance electrodes deploy does increase the width of the shank in most designs and needs to be optimized.

Chronically implanted neural probes can suffer biological failure mechanisms, but also failure of the implanted materials. Parylene is inert, it does not dissolve inside the body and it is unlikely to break. Hence developing neural probes with deployable electrodes that consist of either a silicon core that is coated with Parylene, or solid Parylene, or having a detachable, indwelling Parylene component might reduce the frequency of material failures.

After optimization and evaluation, neural probes with deploying electrodes should be translated into clinical/scientific applications. This could include changing the type of interface from electrodes to optical waveguides or light emitting diodes, or integrating the spring actuation into a shank of a probe developed for deep brain stimulation. This might be especially beneficial, since their large footprint might evoke an even larger encapsulation preventing successful recording.

APPENDICES

A.1 Parylene cables

The electrical signals recorded from electrodes on neural probes can be routed to a connector through flexible cables made from polymers [118, 119]. One motivation to use flexible cables instead rigid anchoring is to allow to probe shank to move more freely with the brain tissue. This was shown to decrease the brain tissue response [120].

For this thesis the general compatibility of the fabricated neural probes with deployable electrodes with tethering cables was demonstrated. To increase the yield of the neural probe fabrication on silicon wafers, the relatively large Parylene cables were fabricated in a separate process and then individually assembled to probes.

Flexible polymer cables were fabricated by sandwiching metal interconnects between two Parylene layers. First, a 3 μm thick layer of Megaposit SPR-220 photoresist (MicroChem Corp., MA, USA) was spun on the wafer, serving as sacrificial release layer. The resist was flood-exposed and hard-baked to reduce outgassing. Then a 5 μm thick layer of Parylene is deposited using a PDS2035 (SCS, IN, USA) without adding any adhesion promoter. A layer of Cr/Au/Cr (300/3000/300 Å) was patterned using e-beam evaporation and lift-off. To facilitate the lift-off the photoresist was formed to have an undercut. This was done using a short TMAH dip after spin-coating to create an inhibition layer at the surface [121]. A second layer of Parylene is deposited

(5 μm). The stack is then etched in RIE with oxygen plasma using ti/al (750/2000 Å) and 10 μm thick photoresist (SPR220) as etch mask. This was followed by an annealing step: The wafer was covered with a several mm thick glass plate and heated on a hot-plate to 115 °C for 30 min. After cooling and stripping the etch mask the cables were gently released by dissolving the photoresist in acetone.

The cables were connected to the silicon probes using rivet bonding [115]. For the bonding process the probes (starch coating was done after this procedure) were temporarily glued to a silicon dice using photoresist. The cables then were manually aligned to bonding pads on the probes. It was of great help to apply a small drop of water between the cable and the dice. The mechanical and electrical connection was made by bonding gold bumps on bonding pads on the silicon probes through perforations in the Parylene cable. The pitch between adjacent bond pads was 150 μm, the area of the perforation in the Parylene cable was 40 μm². A ball bonder K&S4522 (Kulicke and Soffa, Singapore) was used. The cables were then connected in similar fashion to a printed circuit board (PCB). The connection between probe and cable was insulated with EPO_TEK 353ND epoxy glue (Epoxy Technology, MA, USA). The probes with cables were clamped on a bump consisting of clay. A small drop of epoxy glue was dispensed on the desired location and allowed to distribute. The glue wicked between cable and probe. Subsequently the assembly is cured on a hotplate.

The resistance of the metal lines on the cables was measured to be around 100 Ohms, the bonding was high yield. The epoxy was able to withstand short time soaking in salt water. No long time soak tests were performed.

a)

Photoresist

Silicon
shank
with
rivet
bonds

Parylene
cable

500 µm

b)

Cured epoxy glue
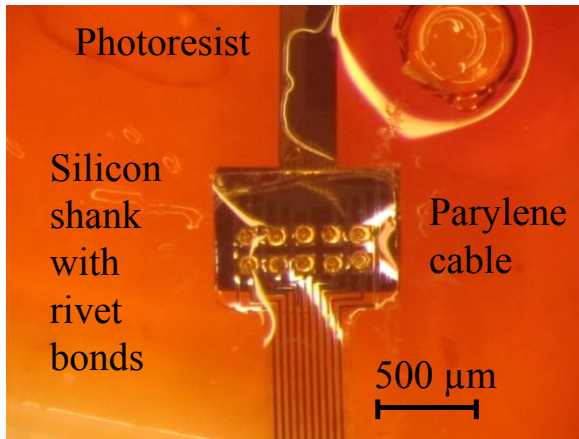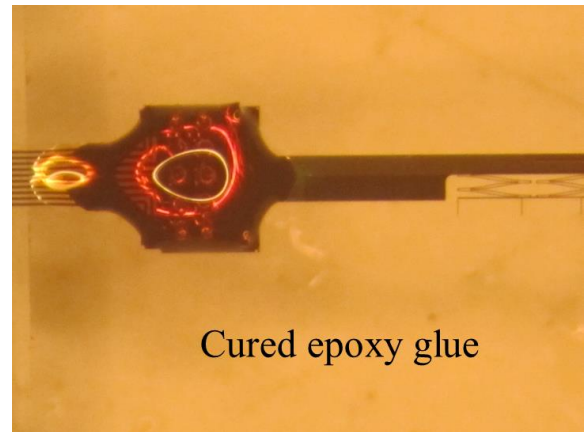
Figure 84: a) silicon probe after rivet-bonding to a Parylene cable. b) neural probe with springs bonded to a Parylene cable, connection insulated using epoxy glue.

A.2 Electrode impedance spectra

Figure 85 through Figure 92 show the averaged (4 electrodes) impedance magnitude/phase spectra of electrodes on the shank and on needles, with and without plated PEDOT:pTS. Figure 93 through Figure 96 show the non-averaged impedances at 1 kHz, of probes with and without plated PEDOT:pTS.
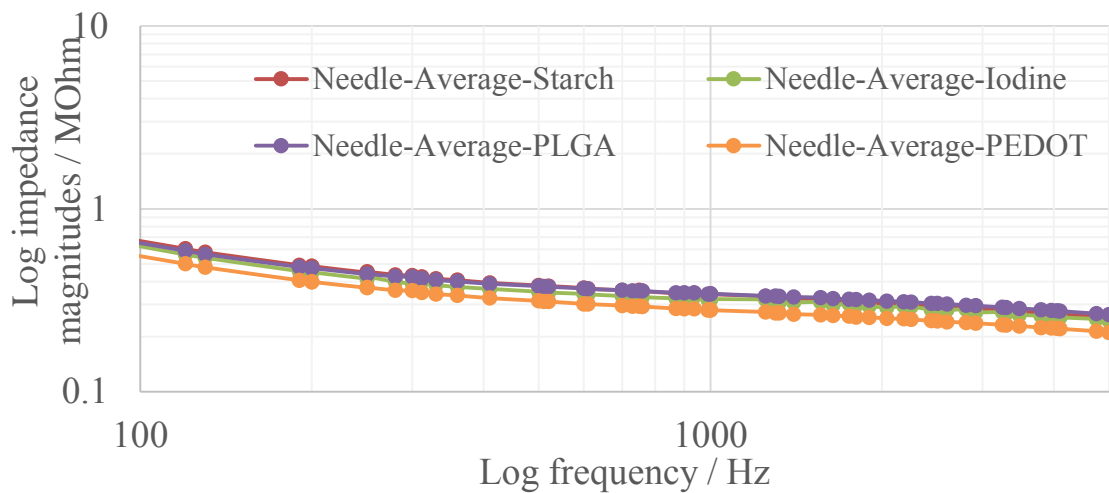
Figure 85: Impedance magnitude spectrum of needle electrodes with PEDOT:pTS
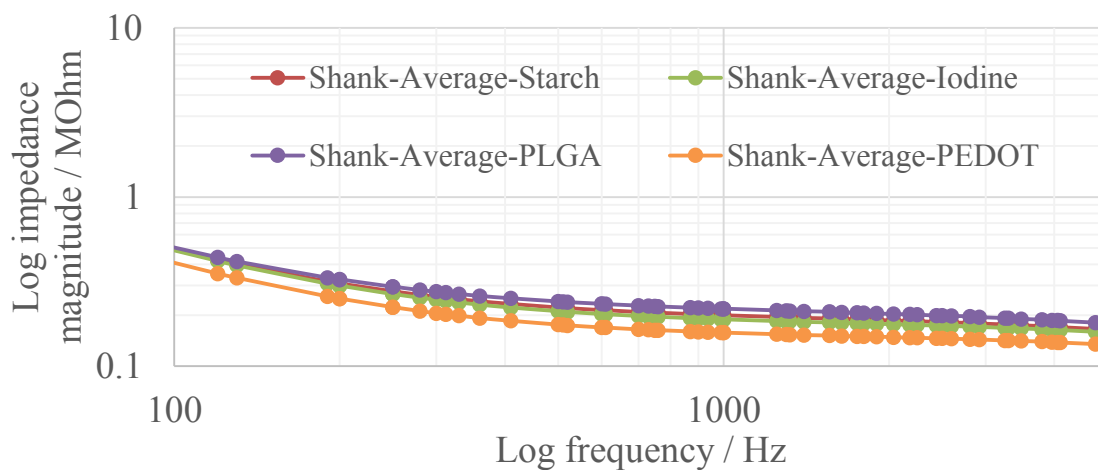
Figure 86: Impedance magnitude spectrum of shank electrodes with PEDOT:pTS
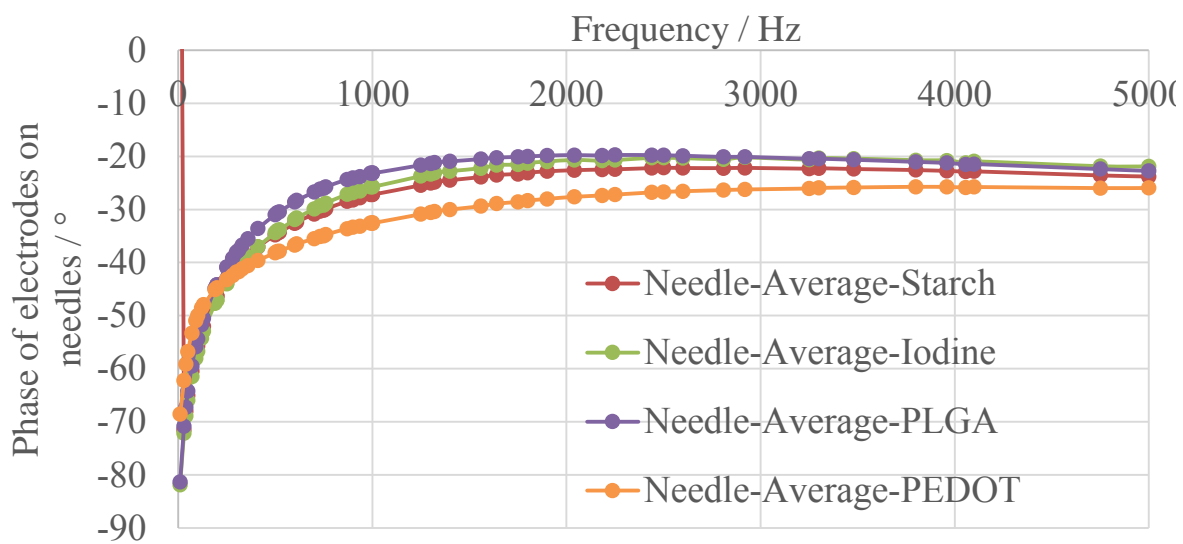
Figure 87: Impedance phase spectrum of needle electrodes with PEDOT:pTS
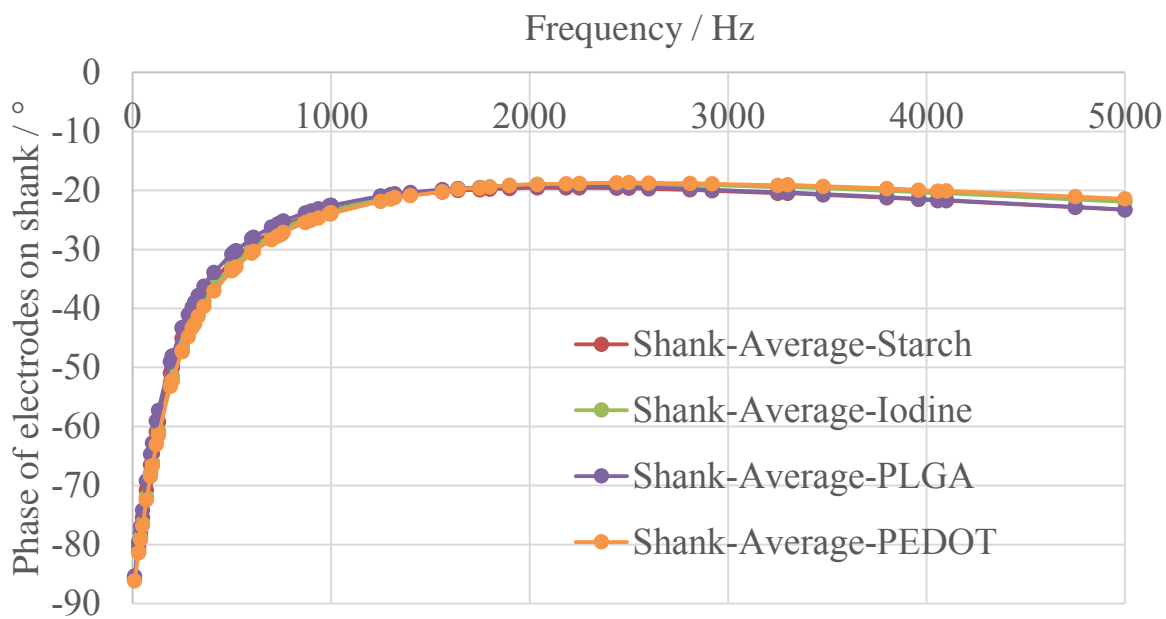
Figure 88: Impedance phase spectrum of shank electrodes with PEDOT:pTS
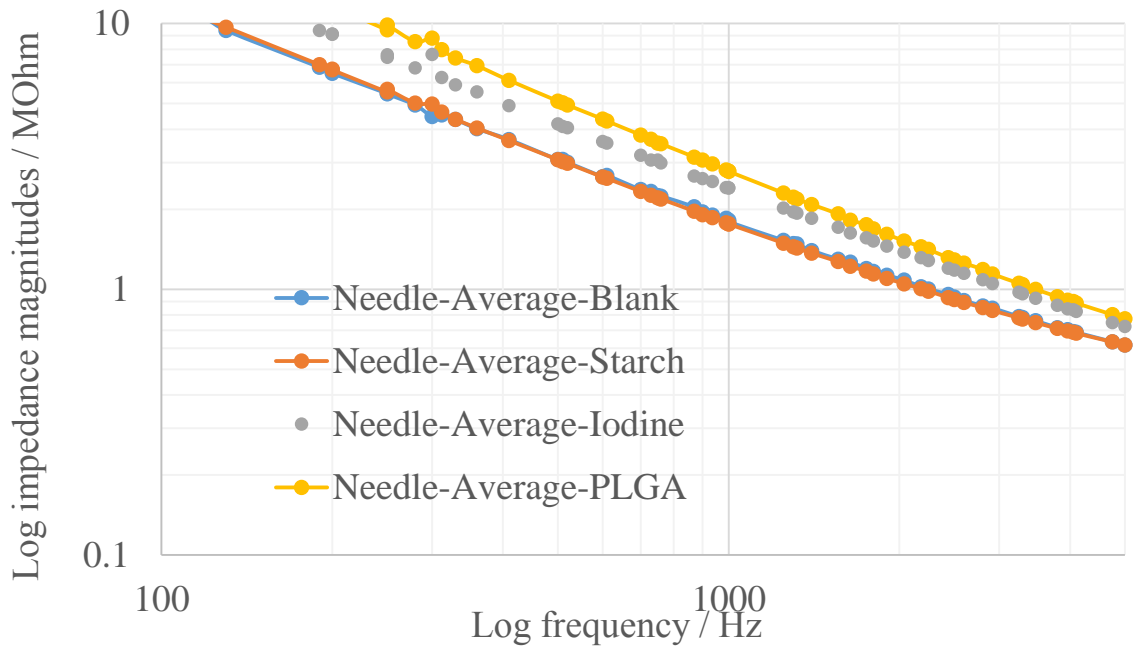
Figure 89: Impedance magnitude spectrum of shank electrodes without PEDOT:pTS
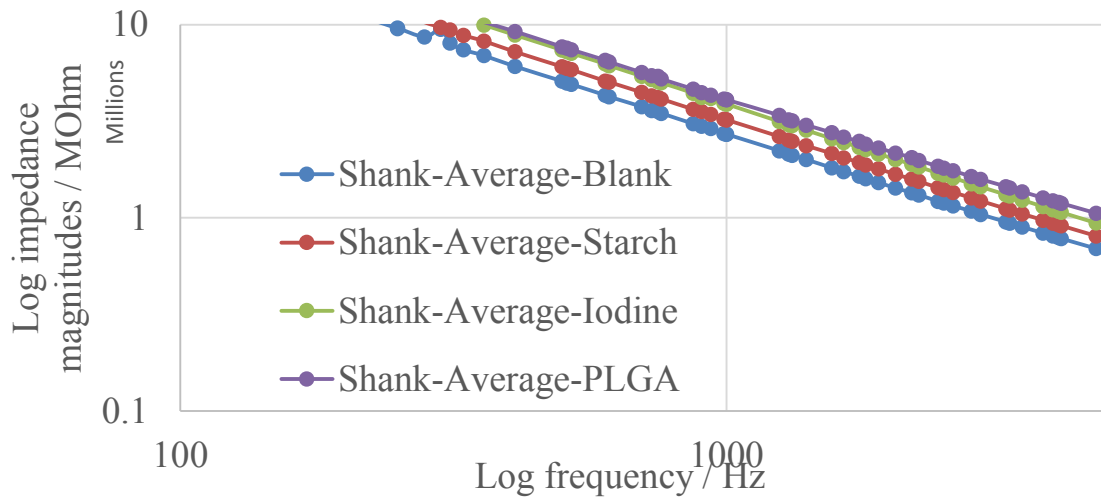
Figure 90: Impedance magnitude spectrum of shank electrodes without PEDOT:pTS
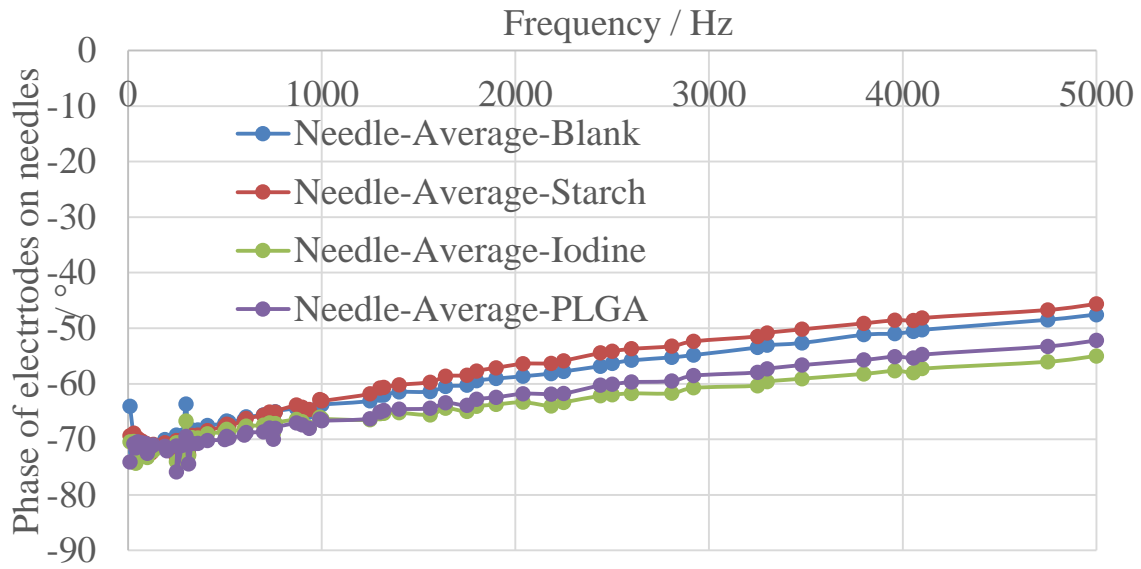
Figure 91: Impedance phase spectrum of needle electrodes without PEDOT:pTS
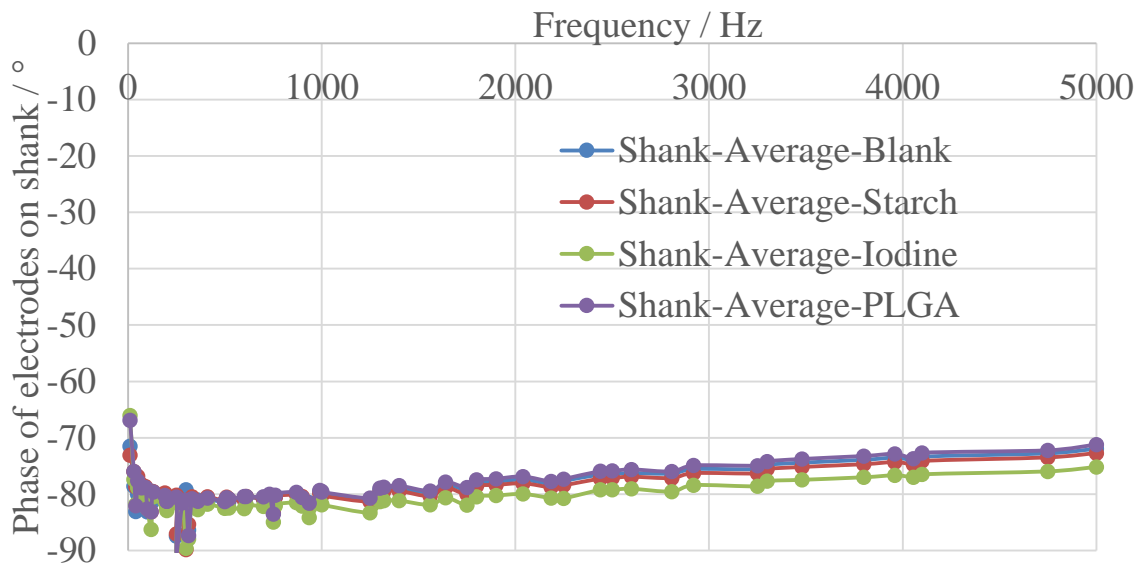
Figure 92: Impedance phase spectrum of shank electrodes without PEDOT:pTS
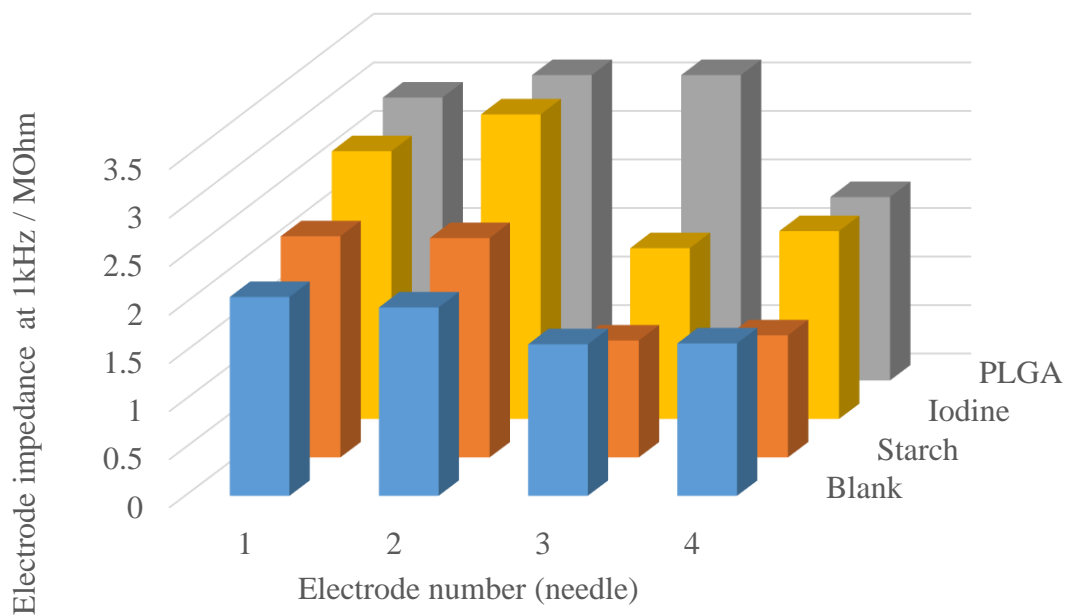
Figure 93: Individual values of needle electrode impedances measured at 1 kHz (without PEDOT:pTS).
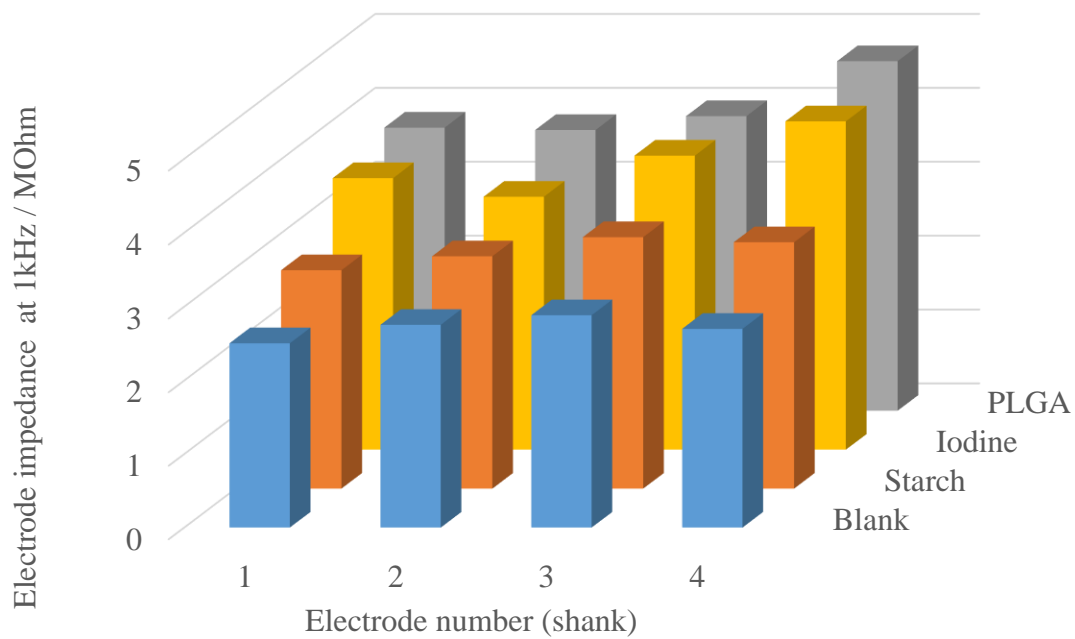
Figure 94: Individual values of shank electrode impedances measured at 1 kHz (without PEDOT:pTS)
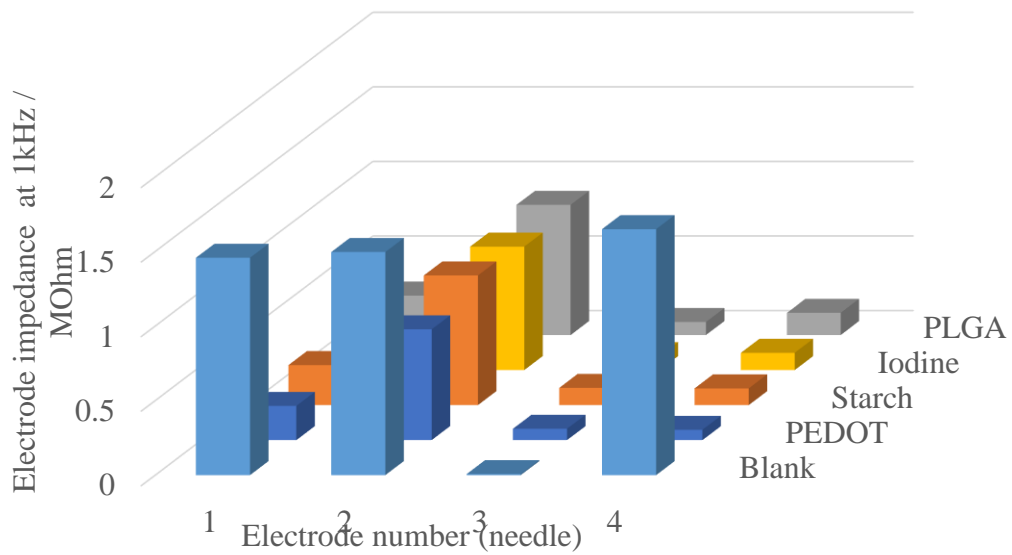
Figure 95: Individual values of needle electrode impedances measured at 1 kHz (with PEDOT:pTS).
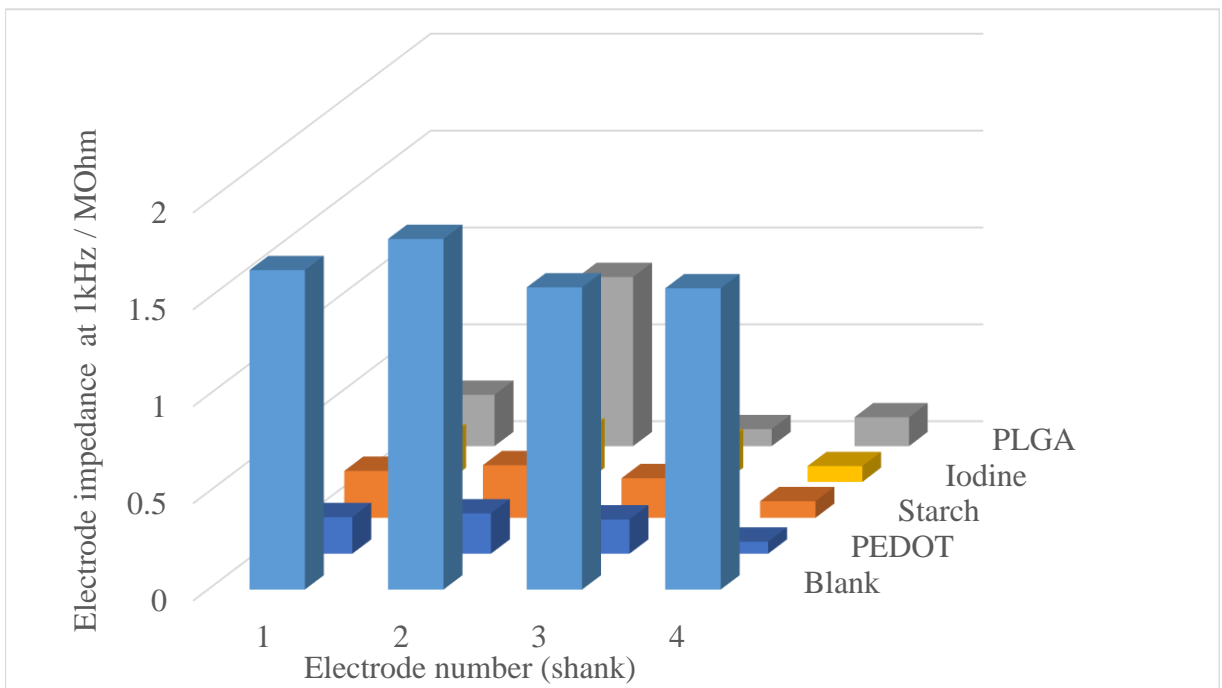
Figure 96: Individual values of shank electrode impedances measured at 1 kHz (with PEDOT:pTS).

173

A.3 Electrode deploying curves without averaging

Figure 97 and *Figure 98* show the measured deployed distances of starch coated springs in water heated to 37°C. These figures show the individual measurements for each trial, while the data shown in paragraph 3.6 shows their averaged value.
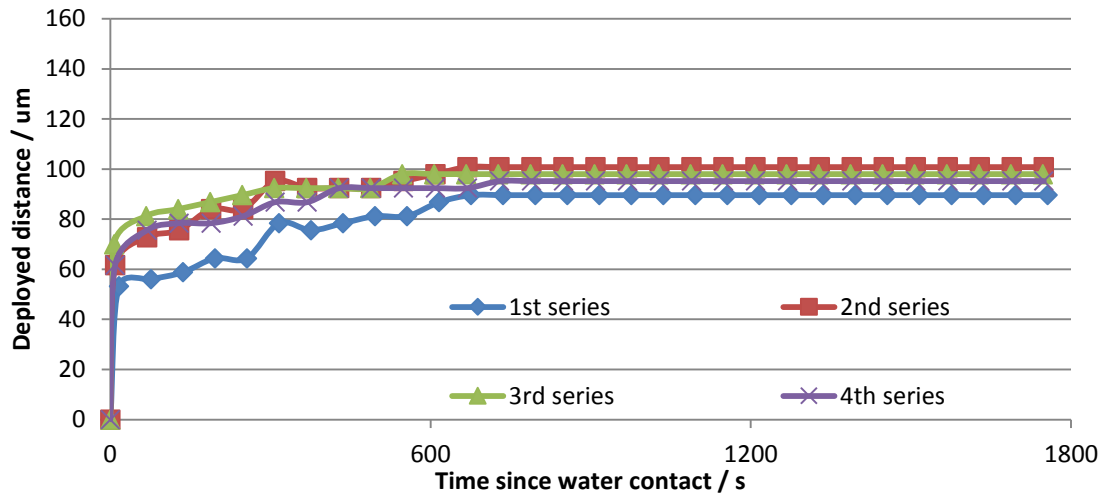
Figure 97: Starch-coated springs, iodized, deploying in water at 37 °C after air exposure at 100 °C for 10 min. Four separate series are shown.
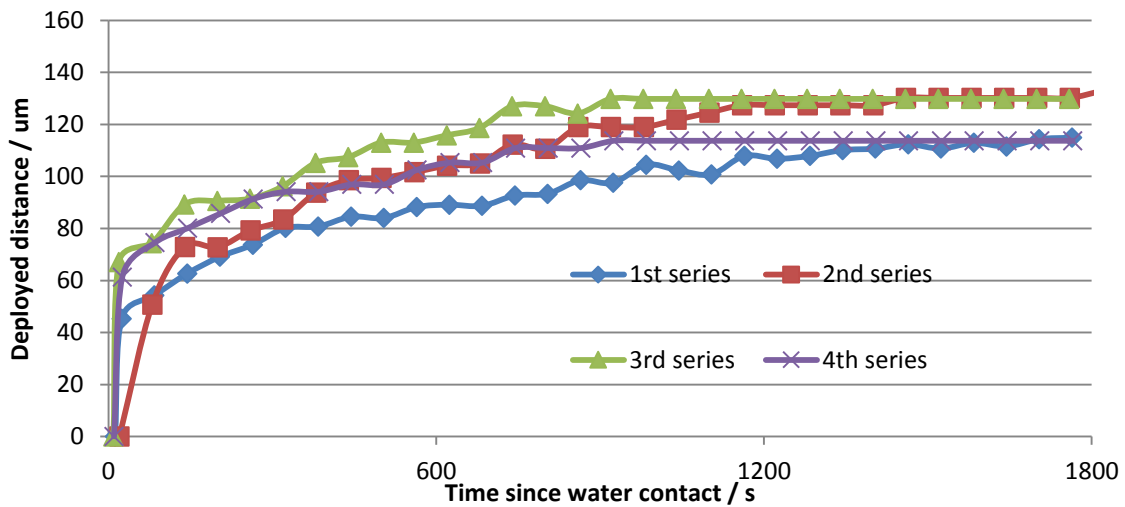
Figure 98: Starch-coated springs, iodized, deploying in water at 37°C. Four separate series are shown.

175

REFERENCES

[1]   K. Wise, A. Sodagar, Y. Yao, M. Gulari, G. Perlin and K. Najafi, "Microelectrodes, Microelectronics, and Implantable Neural Microsystems," *Proceedings of the IEEE,* vol. 96, no. 7, pp. 1184-1201, 2008.

[2]   G. Schalk, "Can Electrocorticography (ECoG) Support Robust and Powerful Brain–Computer Interfaces?," *Frontiers in Neuroengineering,* vol. 3, no. 9, 2010.

[3]   K. Deisseroth, "Optogenetics," *Nature Methods,* vol. 8, pp. 26-29, 2011.

[4]   F. Gilbert, A. Harris and R. Kapsa, "Controlling Brain Cells With Light: Ethical Considerations for Optogenetic Clinical Trials," *AJOB Neuroscience,* vol. 5, no. 3, pp. 3-11, 2014.

[5]   M. Haeusser, "Optogenetics: the age of light," *Nature Methods,* vol. 11, pp. 1012-1014, 2014.

[6]   J. Chen, K. Wise, J. Hetke and S. Bledsoe, "A Multichannel Neural Probe for Selective Chemical Delivery at the Cellular Level," *Transactions on Biomedical Engineering,* vol. 44, no. 8, pp. 760-769, 1997.

[7]   L. Nicolas-Alonso and J. Gomez-Gil, "Brain Computer interfaces, a Review," *Sensors,* vol. 12, no. 2, pp. 1211-1279, 2012.

[8]   J. Simeral, S. Kim, M. Black, J. Donoghue and K. Hochberg, "Neural control of cursor trajectory and click by a human with tetraplegia 1000 days after implant of an intracortical microelectrode array," *Journal of Neural Engineering,* vol. 8, no. 2, 2011.

[9]   L. R. Hochberg, D. Bacher, B. Jarosiewicz, N. Y. Masse, J. D. Simeral, J. Vogel, S. Haddadin, J. C. S. S. Liu, P. Smagy and J. P. Donoghue, "Reach and grasp by people with tetraplegia using a neurally controlled robotic arm," *Nature,* vol. 485, pp. 372-378, 2012.

[10]   C. Chestek, V. Gilja, P. Nuyujukian, J. Foster, J. Fan, M. Kaufman, M. Churchland, Z. Rivera-Alvidrez, J. Cunningham, S. Ryu and K. Shenoy, "Long-term stability of neural prosthetic control signals from silicon cortical arrays in rhesus macaque motor cortex," *Journal of Neural Engineering,* vol. 8, 2011.

[11]   S. Miocinovic, S. Somayajula, S. Chitnis and J. Vitek, "History, Applications, and Mechanisms of Deep Brain Stimulation," *JAMA Neurology,* vol. 70, no. 2, pp. 163-171, 2013.

[12] A. M. Sodagar, G. E. Perlin, Y. Yao, K. Najafi and K. D. Wise, "An implantable 64-channel wireless microsystem for single-unit neural recording," *IEEE Journal of Solid-State Circuits,* vol. 44, no. 9, pp. 2591-2604, 2009.

[13] D. Kipke, W. Shain, G. Buzsaki, E. Fetz, J. Henderson, J. Hetke and G. Schalk, "Advanced Neurotechnologies for Chronic Neural Interfaces: New Horizons and Clinical Opportunities," *Journal of Neuroscience,* vol. 28, no. 46, pp. 11830-11838, 2008.

[14] A. Berenyi, Z. Somogyvari, A. J. Nagy, L. Roux, J. D. Long, S. Fujisawa, E. Stark, A. Leonardo, T. D. Harris and G. Buzsaki, "Large-scale, high-density (up to 512 channels) recording of local circuits in behaving animals," *Journal of Neurophysiology,* vol. 111, pp. 1132-1149, 2013.

[15] D. Orenstein, "Brown University: News from Brown," Brown University, 16 May 2012. [Online]. Available: https://news.brown.edu/articles/2012/05/braingate2. [Accessed 14 November 2014].

[16] L. Karumbaiah, T. Saxena, D. Carlson, K. Patil, R. Patkar, E. A. Gaupp, M. Betancur, G. B. stanley, L. Carin and R. V. Bellamkonda, "Relationship Between Intracortical Electrode Design and Chronic Recording Function," *Biomaterials,* vol. 34, pp. 8061-8074, 2013.

[17] V. Gilja, C. Chestek, I. Diester, J. Henderson, K. Deisseroth and K. Shenoy, "Challenges and Opportunities for Next-Generation Intracortically Based Neural Prostheses," *Transactions on Biomedical Engineering,* vol. 58, no. 7, pp. 1891-1897, 2011.

[18] R. Biran, D. C. Martin and A. P. Tresco, "Neuronal cell loss accompanies the brain tissue response to chronically implanted silicon microelectrode arrays," *Experiment Neurology,* vol. 195, pp. 115-126, 2005.

[19] D. H. Szarowski, M. Andersen, S. Retterer, A. Spence, M. Isaacson, H. Craighead, J. Turner and W. Shain, "B rain responses to micro-machined silicon devices," *Brain Research ,* vol. 983, pp. 23-35, 2003.

[20] B. Winslow and P. Tresco, "Quantitative analysis of the tissue response t chronically implanted microwire electrodes in rat cortex," *Biomaterials,* vol. 31, pp. 1558-1567, 2010.

[21] A. Prasad, Q. Xue, V. Sankar, T. Nishida, G. Shaw, J. W. Streit and J. C. Sanchez, "Comprehensive Characterization and Failure Modes of Tungsten Microwire Arrays in Chronic Neural Implants," *Journal of Neural Engineering,* vol. 9, 2012.

[22] T. Kozai, Z. Du, Z. Gugel, M. Smith, S. Chase, L. Bodily, E. Caparosa, R. Friedlander and X. Cui, "Comprehensive chronic laminar single-unit, multi-unit, and local field potential recording performance with planar single shank electrode arrays," *Journal of Neuroscience Methods,* vol. 242, pp. 15-40, 2015.

[23] T. Saxena, L. Karumbaiah, E. A. Gaupp, R. Patkar, K. Paril, M. Betancur, G. B. Stanley and R. V. Bellamkonda, "The impact of chronic blood-brain barrier breach on intracortical electrode function," *Biomaterials,* vol. 34, pp. 4703-4713, 2013.

[24] G. Buzsáki, "Large-scale recording of neuronal ensembles," *Nature Neuroscience,* vol. 7, no. 5, pp. 446-451, 2004.

[25] J. P. Frampton, M. R. Hynd, M. L. Shuler and W. Shain, "Effects of Glial Cells on Electrode Impedance Recorded from Neural Prosthetic Devices in Vitro," *Annals of Biomedical Engineering,* vol. 38, no. 3, pp. 1031-1047, 2010.

[26] J. P. Frampton, M. R. Hynd, J. C. Williams, M. L. Shuler and W. Shain, "Three-dimensional hydrogel cultures for modeling changes in tissue impedance around microfabricated neural probes," *Journal of Neural Engineering,* vol. 4, 2007.

[27] J. L. Skousen, M. E. Merriam, O. Srivannavit, G. Perlin, K. D. Wise and P. Tresco, "Reducing surface area while maintaining implant penetrating profile lowers the brain foreign body response to chronically implanted planar silicon mircoelectrode arrays," *Progress in Brain Research,* vol. 194, 2011.

[28] J. P. Seymour and D. R. Kipke, "Neural probe design for reduced tissue encapsulation in CNS," *Biomaterials,* vol. 28, pp. 3594-3607, 2007.

[29] J. Witteveeen, D. Suyatin, L. Gaellentoft, J. Schouenborg, N. Danielsen and C. Prinz, "Gelatin/Glycerol coating to preserve mechanically compliant nanowire electrodes from damage during brain implantation," *Journal of Vacuum Science & Technology B,* vol. 28, no. 6, 2010.

[30] L. W. Tien, F. Wu, M. D. Tang-Schomer, E. Yoon, F. G. Omenetto and D. L. Kaplan, "Silk as a Multifunctional Biomaterial Substrate for Reduced Glial Scarring around Brain-Penetrating Electrodes," *Advanced Functional Materials,* vol. 23, 2013.

[31] T. Kozai, Z. Gugel, X. Li, P. Gilgunn, R. Khilwani, O. Ozdoganiar, G. Fedder, D. Weber and X. Cui, "Chronic tissue response to carboxymethyl cellulose based dissolvable insertion needle for ultra-small neural probes," *Biomaterials,* vol. 35, no. 34, pp. 9255-9268, 2014.

[32] H. Sohal, A. Jackson, R. Jackson, G. Clowry, K. Vassilevski, A. O'Neill and S. Baker, "The sinusoidal probe: a new approach to improve electrode longevity," *Frontiers in Neuroengineering,* vol. 7, 2014.

[33] J. Thelin, H. Jorntell, E. Psouni, M. Garwicz, J. Schouenborg, N. Danielsen and C. E. Linsmeier, "Implant Size and Fixation Mode Strongly Influence Tissue Reactions in the CNS," *PLoS ONE,* vol. 6, no. 1, 2011.

[34] A. Sharp, V. Panchawagh, A. Ortega, R. Artale, S. Richardson-Burns, D. Finch, K. Gall, L. Mahajan and R. D., "Toward a self-deploying shape memory polymer neuronal electrode," *Journal of Neural Engineering,* vol. 3, no. 4, 2006.

[35] M. Kang, S. Jung, H. Zhang, T. Kang, H. Kang, Y. Yoo, J. Hong, J. Ahn, J. Kwak, D. Jeon, N. A. Kotov and B. Kim, "Subcellular Neural Probes from Single-Crystal Gold Nanowires," *ACS Nano,* vol. 8, no. 8, pp. 8182-8189, 2014.

[36] D. Egert and K. Najafi, "New class of chronic recording multichannel neural probes with post-implant self-deployed satellite recording sites," in *Transducers '11*, Beijing, China, 2011.

[37] G. Lind, C. Linsmeier, J. Thelin and J. Schouenborg, "Gelatine-embedded electrodes—a novel biocompatible vehicle allowing implantation of highly flexible microelectrodes," *Journal of Neural Engineering,* no. 7, 2010.

[38] S. Martel and T. Fofonoff, "New Approaches for the Implementation of Minimally Invasive Microelectrode Arrays Designed for Brain-Machine Interfaces," in *EMBS*, Cancun, Mexico, 2003.

[39] A. Cutrone and S. Bossi, "Development of a Self-Opening Neural Interface," *Journal of Medical Devices,* vol. 7, 2013.

[40] S. Bossi, S. Kammer, T. Doerge, A. Menciassi, K. Hoffmann and S. Micera, "An Implantable Microactuated Intrafascicular Electrode for Pripheral Nerves," *Tansactions on Biomedical Engineering,* vol. 56, no. 11, pp. 2701-2706, 2009.

[41] E. Daneshvar and E. Smela, "Characterization of Conjugated Polymer Actuation under Cerebral Physiological Conditions," *Advanced Healthcare Materials,* 2014.

[42] L. Ionov, "Hydrogel-based actuators: possibilities and limitations," *Materials Today,* vol. 17, no. 10, pp. 494-503, 2014.

[43] D. Winslow, B. Christensen, W. Yang, F. Solzbacher and P. Tresco, "A comparison of the tissue response to chronically implanted Parylene-C-coated and uncoated planar silicon microelectrode arrays in rat cortex," *Biomaterials,* vol. 31, pp. 9163-9172, 2010.

[44] J. Subbaroyan, D. C. Martin and D. R. Kipke, "A finite-element model of the mechanical effects of implantable microelectrodes in the cerebral cortex," *Journal of Neural Engineering,* vol. 2, pp. 103-113, 2005.

[45] P. J. Rousche and R. A. Normann, "A Method for Pneumatically Inserting an Array of Penetrating Electrodes into Cortical Tissue," *Annals of Biomedical Engineering,* vol. 20, pp. 413-422, 1992.

[46] M. Welkenhuysen, L. Ameye, W. Eberle and B. Nuttin, "Effect of Insertion Speed on Tissue Response and Insertion Mechanics of Chronically Implanted Silicon-Based Neural Probe," *Transactions on Biomedical Engineering,* vol. 58, no. 11, 2011.

[47] J. Gere and S. Timoshenko, Mechanics of Materials, Boston, MA: PWS Publishing Company, 1997.

[48] M. Hopcroft, W. Nix and T. Kenny, "What is the Young's Modulus of Silicon?," *Journal of Microelectromechanical Systems,* vol. 19, no. 2, pp. 229-238, 2010.

[49] S. Hu, "Critical stress in silicon brittle fracture, and effect of ion implantation and other surface treatments," *Journal of Applied Physics,* vol. 53, no. 5, pp. 3576-3580, 1982.

[50] D. K. S. Manjeet and J. Heikenfeld, "Reliable and low-voltage electrowetting on thin parylene films," *Thin Solid Films,* vol. 519, no. 10, p. 3346–3351, 2011.

[51] R. A. Cooper, "Iodine Revisited," *International Wound Journal,* vol. 4, no. 2, pp. 124-137, 2007.

[52] P. Foley, N. Nishimura, B. Neeves, B. Schaffer and L. Olbricht, "Flexible microfluidic devices supported by biodegradable insertion scaffolds for convection-enhanced neural drug delivery," *Biomedical Microdevices,* pp. 915-924, 2009.

[53] P. Durani and D. Leaper, "Povidone–iodine: use in hand disinfection, skin preparation and antiseptic irrigation," *International Wound Journal,* vol. 5, no. 3, pp. 376-387, 2008.

[54] P. Stice, A. Gilletti, A. Panitch and J. Muthuswamy, "Thin microelectrodes reduce GFAP expression in the implant site in rodent somatosenory cortex," *Journal of Neural Engineering,* vol. 4, pp. 42-53, 2007.

[55] J. E. Sanders, C. E. Stiles and C. L. Hayes, "Tissue response to single-polymer fibers of varying diameters: Evaluation of fibrous encapsulation and macrophage density," *Journal of Biomedical Material Research,* vol. 52, no. 1, pp. 231-237, 2000.

[56] J. Du, T. Blanche, R. R. Harrison, H. A. Lster and S. C. Masmanidis, "Multiplexed, High Density Electrophysiology with Nanofabricated Neural Probes," *PLOS One,* vol. 6, no. 10, 2011.

[57] D. Egert, R. L. Peterson and K. Najafi, "Parylene microprobes with engineered stiffness and shape for improved insertion," in *Transducers '11*, Beijing, 2011.

[58] H. Lee, R. Bellamkonda, W. Sun and M. Levenston, "Biomechanical analysis of silicon microelectrode-induced strain in the brain," *Journal of Neural Engineering,* vol. 2, pp. 81-90, 2005.

[59] A. Olamat, N. Nkemasong, B. Pohl and U. Hofmann, "Physical and FEM Simulation of Microprobe Insertion into Rat Brain," in *COMSOL Conference*, Paris, 2010.

[60] K. Mendis, R. Stalnaker and S. Advani, "A Constitutive Relationship for Large Deformation Finite Element Modeling of Brain Tissue," *Journal of Biomedical Engineering,* vol. 117, pp. 279-285, 1995.

[61] K. Wise, D. Anderson, J. Hetke, D. Kipke and K. Najafi, "Wireless implantable microsystems: high-density electronic interfaces to the nervous system," *Proceedings of the IEEE,* vol. 92, no. 1, pp. 76-97, 2004.

[62] Z. Chen, G. T. Gillies, W. C. Broaddus, S. S. Prabhu, H. Fillmore, R. M. Mitchell, F. D. Corwin and P. Fatouros, "A realistic brain tissue phantom for intraparenchymal infusion studies," *Journal of Neurosurgery,* vol. 101, pp. 314-322, 2004.

[63] S. F. Lempka, M. D. Johnson, M. A. Moffitt, K. J. Otto, D. R. Kipke and C. C. McIntyre, "Theoretical analysis of intracortical microelectrode recordings," *Journal of Neural Engineering,* vol. 8, no. 4, 2011.

[64] S. F. Cogan, "Neural Stimulation and Recording Electrodes," *Biomedical Engineering,* vol. 10, pp. 275-309, 2008.

[65] R. A. Green, R. T. Hassarati, L. Bouchinet, C. S. Lee, L. G. M. Cheong, J. F. Yu, C. W. Dodds, G. J. Suaning, L. A. Poole-Warren and N. H. Lovell, "Substrate dependent stability of conducting polymer coatings on medical electrodes," *Biomaterials,* vol. 33, no. 25, pp. 5875-5886, 2012.

[66] D. A. Henze, Z. Borhegyi, J. M. A. Csicsvari, K. D. Harris and G. Buzsaki, "Intracellular Features Predicted by Extracellular Recordings in the Hippocampus In Vivo," *Journal of Neuronal Physiology,* vol. 84, pp. 390-400, 2000.

[67] J. Csicsvari, D. A. Henze, B. Jamieson, K. D. Harris, A. Sirota, P. Barth, K. D. Wise and G. Buzsaki, "Massively Parallel Recording of Unit and Local Field Potentials With Silicon-Based Electrodes," *Journal of Neurophysiology,* vol. 90, pp. 1314-1323, 2003.

[68] S. Paik, Y. Park and D. Cho, "Roughened polysilicon for low impedance microelectrodes in neural probes," *Journal of Micromechanics and Microengineering,* vol. 13, pp. 373-379, 2003.

[69] Y. Xiao, X. Cui and D. Martin, "Electrochemical polymerization and properties of PEDOT/S-EDOT on neural microelectrode arrays," *Journal of Electroanalytical Chemistry,* vol. 573, pp. 43-48, 2004.

[70] H. Muro, T. Mitamura and S. Kiyota, "Determination of Electrical Properties of n-Type and p-Type Polycrystalline Silicon Thin Films as Sensor Materials," *Sensors and Materials,* vol. 18, no. 8, pp. 433-444, 2006.

[71] L. Ionov, "Biomimetic Hydrogel-Based Actuating Systems," *Advanced Materials,* vol. 23, pp. 4555-4570, 2013.

[72] T. Leong, C. Randall, B. Benson, N. Bassik, G. Stern and D. Gracias, "Tetherless thermobiochemically actuated microgrippers," *PNAS,* vol. 106, no. 3, pp. 703-708, 2012.

[73] T. W. Lee, F. Wu, M. D. Tang-Schomer, E. Yoon, F. G. Omenetto and D. L. Kaplan, "Silk as a Multifunctional Biomaterial Substrate for Reduced Glial Scarring around Brain-Penetrating Electrodes," *Advanced Functional Materials,* vol. 23, no. 25, pp. 3185-3193, 2013.

[74] A. Aghel and J. E. Armstrong, "Recent advances in self-expanding stents for use in the superficial femoral and popliteal arteries," *Expert Reviews in Cardiovascular Therapy,* vol. 12, no. 7, pp. 833-842, 2014.

[75] X. Wang, S.-G. Choi and L. W. Kerr, "Water dynamics in white bread and starch gels as affected by water and gluten content," *Food Science and Technology,* vol. 37, pp. 377-384, 2004.

[76] J. J. Gibson, "The hierarchiacal structure and mechanics of plant materials," *Journal of the Royal Interface Society,* 2012.

[77] R. Tester, X. Qi and J. Karkalas, "Hydrolysis of native starches with amylases," *Animal Feed Science and Technology,* vol. 130, no. 1-2, pp. 39-54, 2006.

[78] H. Fredriksson, J. Silveriob, R. Anderssona, A.-C. Eliassonb and Å. P., "The influence of amylose and amylopectin characteristics on gelatinization and retrogradation properties of different starches," *Carbohydrate Polymers,* vol. 35, no. 3-4, pp. 119-134, 1998.

[79] D. S. J. Wajira S. Ratnayake, "Gelatinization and Solubility of Corn Starch during Heating in Excess Water: New Insights," *Journal of Agricultural and Food Chemistry,* vol. 54, no. 10, 2006.

[80] S. C. L. Wang, "Molecular disassembly of starch granules during gelatinization and its effect on starch digestibility: a review," *Food and Function,* vol. 4, pp. 1564-1580, 2013.

[81] R. R. Rundle and B. R. R., "The Configuration of starch and the Starch-Iodine Complex. I. The Dichroism of Flow of Starch-Iodine Solutions," *Journal of the American Chemical Society,* vol. 65, no. 4, pp. 554-558, 1943.

[82] D. Simarata, E.-S. M. Abdel-Aal and S. Koushik, "Effect of iodine on polymer leaching and granule swelling of starches from different botanical sources," *Journal of Cereal Science,* vol. 54, pp. 76-82, 2011.

[83] A. J. Salgado, O. P. Coutinho, R. R. L. and D. J. E., "In vivo response to starch-based scaffolds designed for bone tissue engineering applications," *Journal of Biomedical Materials Research Part A,* vol. 80, no. 4, 2007.

[84] C. Elvira, J. F. Mano, J. San Román and R. R. L., "Starch-based biodegradable hydrogels with potential biomedical applications as drug delivery systems," *Biomaterials,* vol. 23, no. 9, pp. 1955-1966, 2002.

[85] L. H. Zhou, W. K. Nahm, E. Badiavas and T. F. V. Yufit, "Slow release iodine preparation and wound healing: in vitro effects consistent with lack of in vivo toxicity in human chronic wounds," *British Journal of Dermatology,* vol. 146, no. 3, pp. 365-374, 2002.

[86] A. Beilvert, F. Chaubet, L. Chaunier, S. Guilois, G. Pavon-Djavid and D. Letourneur, "Shape-memory starch for resorbable biomedical devices," *Carbohydrate Polymers,* vol. 99, pp. 242-248, 2014.

[87] D. J. Beebe, J. S. Moore, J. M. Bauer, Q. Yu, R. H. Liu, C. Devadoss and B.-H. Jo, "Functional hydrogel structures for autonomous flow control inside microfluidic channels," *Nature,* vol. 404, pp. 588-591, 2000.

[88] G. A. Gilbert and J. V. R. Marriott, "Starch-iodine complexes. Part I," *Transactions of the Faraday Society,* pp. 84-93, 1948.

[89] E. Fernández, B. Greger, P. A. House, I. Aranda and C. Botella, "Acute human brain responses to intracortical microelectrode arrays: challenges and future prospects," *Frontiers in Neuroengineering,* vol. 7, June 2014.

[90] G. E. Loeb, R. A. Peck and J. Martyniuk, "Toward the ultimate metal microelectrode," *Journal of Neuroscience Methods,* vol. 63, pp. 175-183, 1995.

[91] M. Varney, D. Aslam, A. Janoudi and H. W. D. Chan, "Polycrystalline-Diamond MEMS Biosensors Including Neural Microelectrode-Arrays," *Electronics, Communications and Photonics Conference (SIECPC),* vol. 1, pp. 118-133, 2011.

[92] S. Takeuchi, D. Ziegler, Y. Yoshida, K. Mabuchi and T. Suzuki, "Parylene flexible neural probes integrated with microfluidic channels," *Lab on a Chip,* vol. 5, no. 5, pp. 519-523, 2005.

[93] P. Rousche, D. Pellinen, D. Pivin, J. Williams, R. Vetter and D. Kipke, "Flexible polyimide-based intracortical electrode arrays with bioactive capability," *IEEE Transactions on Biomedical Engineering,* vol. 48, no. 3, pp. 361-371, 2001.

[94] S. Metza, A. Bertsch, D. Bertrand and P. Renaud, "Flexible polyimide probes with microelectrodes and embedded microfluidic channels for simultaneous drug delivery and

multi-channel monitoring of bioelectric activity," *Biosensors and Bioelectronics,* vol. 19, no. 10, pp. 1309-1318, May 2004.

[95] A. Altuna, L. Menendez de la Prida, E. Bellistri, G. Gabriel, A. Guimerá, J. Berganzo, R. Villa and L. J. Fernández, "SU-8 based microprobes with integrated planar electrodes for enhanced neural depth recording," *Biosensors and Bioelectronics,* vol. 37, no. 1, pp. 1-5, 2012.

[96] J. Lee, S. Oh, K. Song and J. Kim, "Neural signal recording using microelectrode arrays fabricated on liquid crystal polymer material," *Materials Science and Engineering,* vol. 24, pp. 265-268, 2004.

[97] T. Kozai and D. R. Kipke, "Insertion shuttle with carboxyl terminated self-assembled monolayer coatings for implanting flexible polymer neural probes in the brain," *Journal of Neuroscience Methods,* vol. 184, pp. 199-205, 2009.

[98] J. B. Fortin and T. M. Lu, "A Model for the Chemical Vapor Deposition of Poly(para-xylylene) (Parylene) Thin Films," *Chemical Materials,* vol. 14, pp. 1945-1949, 2002.

[99] G. Loeb, M. Bak, M. Salcman and E. Schmidt, "Parylene as a Chronically Stable, Reproducible Microelectrode Insulator," *IEEE Transactions on Biomedical Engineering,* vol. 24, no. 2, pp. 121-129, 1977.

[100] D. Ziegler, T. Suzuki and S. Takeuchi, "Fabrication of Flexible Neural Probes with Built-In Microfluidic Channels by Thermal Bonding of Parylene," *Journal of Microelectromechanical Systems,* vol. 15, no. 6, pp. 1477-1482, December 2006.

[101] K. Lee, A. Singh, J. He, S. Massia, B. Kim and G. Raupp, "Polyimide-based Intracortical Neural Implant with Improved Structural Stiffness," *Journal of Micromechanics and Microengineering,* vol. 14, no. 1, pp. 32-37, 2004.

[102] A. Hess, J. Capadona, K. Shanmuganathan, L. Hsu, S. Rowan, C. Weder, D. Tyler and C. Zorman, "Development of a Stimuli-responsive Polymer Nanocomposite Toward Biologically Optimized, MEMS-based Neural Probes," *Journal of Micromechanical Microengineering,* vol. 21, no. 5, May 2011.

[103] B. J. Kim, S. A. Hara, C. D. Lee, L. Yu, C. A. Cutierrez, T. Q. Hoang, V. Pikov and E. Meng, "3D Parylene Sheath Neural Prob for Chronic Recording," *Journal of Neural Engineering,* vol. 10, no. 4, May 2013.

[104] R. Hoffmann, "Verfahren zur Kortex-Insertion von Polyimid-Mikroelektroden," Freiburg, Germany, 2008.

[105] F. Ayazi and K. Najafi, "High Aspect-ratio Combined Poly and Single-Crystal (HARPSS) MEMS Technology," *Journal of Microelectromechanical Systems,* vol. 9, no. 3, pp. 288-294, 2000.

[106] A. Selvakumar, "A Multifunctional Silicon Micromachining Technology for High Performance Microsensors and Microactuators," Ann Arbor, MI, USA, 1997.

[107] Y. Suzuki and Y. Tai, "Micromachined High-Aspect-Ratio Parylene Spring and Its Application to Low-Frequency Accelerometers," *Journal of Microelectromechanical Systems,* vol. 15, no. 5, pp. 1364-1370, October 2006.

[108] C. S. Bjornsson, S. J. Oh, Y. A. Al-Kofahi, Y. J. Lim, K. L. Smith, J. N. Turner, S. De, B. Roysam, W. Shain and S. J. K. Kim, "Effects of insertion conditions on tissue strain and vascular damage during neuroprosthetic device insertion," *Journal of Neural Engineering,* vol. 3, no. 3, pp. 196-207, 2006.

[109] R. Wang, W. Zhao, W. Wang and L. Zhihong, "A Flexible Microneedle Electrode Array With Solid Silicon Needles," *Journal of Microelectromechanical Systems,* vol. 21, no. 5, pp. 1084-1089, 2012.

[110] A. B. Schwartz, X. T. Cui, D. J. Weber and D. W. Moran, "Brain-Controlled Interfaces: Movement Restoration with Neural Prosthetics," *Neuron,* vol. 52, no. 1, pp. 205-220, 2006.

[111] C. Shih, T. Harder and Y. Tai, "Yield strength of thin-film parylene-C," *Microsystem Technologies,* vol. 10, pp. 407-411, 2004.

[112] A. Andrei, M. Welkenhuysen, B. Nuttin and W. Eberle, "A response surface model predicting the in vivo insertion behavior of micromachined neural implants," *Journal of Neural Engineering,* vol. 11, no. 1, 2011.

[113] M. Salvadori, I. Brown, A. Vaz, L. Melo and M. Cattani, "Measurement of the elastic modulus of nanostructured gold and platinum thin films," *Physical Review B,* vol. 67, no. 15, 2003.

[114] A. Sharp, A. Ortega, D. Restrepo, D. Curran-Everett and K. Gall, "In-Vivo Penetration Mechanics and Mechanical Properties of Mouse Brain Tissue at Micrometer Scales," *IEEE Transactions on Biomedical Engineering,* vol. 56, no. 1, pp. 45-53, 2009.

[115] J. Hetke, J. Williams, D. Pellinen, R. Vetter and D. Kipke, "3-D Silicon Probe Array with Hybrid Polymer Interconnect for Chronic Cortical Recording," in *EMBS*, Capri Islan, Italy, 2003.

[116] J. Williams, J. Hippensteel, J. Dilgen, W. Shain and D. Kipke, "Complex impedance spectroscopy for monitoring tissue responses to inserted neural implants," *Journal of Neural Engineering,* vol. 4, pp. 410-423, 2007.

[117] A. Gilletti and J. Muthuswamy, "Brain micromotion around implants in the rodent somatosensory cortex," *Journal of Neural Engineering,* vol. 3, pp. 189-195, 2006.

[118] T. Sun, W. Park, M. Cheng, J. An, R. Xue, K. Tan and M. Je, "A flexible polyimide cable for implantable neural probe arrays," *Microsystems Technology,* vol. 19, pp. 1111-1118, 2013.

[119] H. Yu, N. Zheng, W. Wang, S. Wang, X. Zheng and Z. Li, "Electroplated Nickel Multielectrode Microprobes with Flexible Parylene Cable for Neural Recording and Stimulation," *Journal of Microelectromechanical Systems,* vol. 22, no. 5, pp. 1199-1205, 2013.

[120] R. Biran, D. Martin and P. Tresco, "The brain tissue response to implanted siliconmicroelectrode arrays is increased when the device is tethered to the skull," *Journal of Biomedical Materials Research,* pp. 169-178, 2007.

[121] R. Redd, D. Maurer and S. Klingbeil, "Revitalization of Single Layer Lift-off for Finer Resolution and Challenging Topography," GaAs MANTECH, Inc., 2001.

[122] V. Polikov, P. Tresco and W. Reichert, "Response of brain tissue to chronically implanted neural electrodes," *Journal of Neuroscience Methods,* vol. 148, pp. 1-18, 2005.